EXPLORATION OF THE SHELL EFFECT ON THE LEVEL DENSITY PARAMETER NEAR DOUBLY CLOSED SHELL NUCLEUS A$\sim$208

By

Prakash Chandra Rout

PHYS01200704009

Bhabha Atomic Research Centre, Mumbai

A thesis submitted to the
Board of Studies in Physical Sciences

In partial fulfillment of the requirements

For the Degree of

DOCTOR OF PHILOSOPHY

of

HOMI BHABHA NATIONAL INSTITUTE

September 2014

Homi Bhabha National Institute

Recommendations of the Viva Voce Committee

As members of the Viva Voce Committee, we certify that we have read the dissertation prepared by **Prakash Chandra Rout** entitled **"Exploration of the Shell Effect on the Level Density Parameter near Doubly Closed Shell Nucleus A∼208"** and recommend that it may be accepted as fulfilling the thesis requirement for the award of Degree of Doctor of Philosophy.

______________________ **Date:** 29/9/2014

Chairman : Prof. A. K. Mohanty

______________________ **Date:** 29/9/2014

Convener : Prof. V. M. Datar

______________________ **Date:** 29-09-2014

Member : Prof. B. N. Jagatap

______________________ **Date:** 29/9/14

Member : Prof. V. Nanal

______________________ **Date:** 29.09.2014

External Examiner : Prof. J. N. De

Final approval and acceptance of this thesis is contingent upon the candidate's submission of the final copies of the thesis to HBNI.

I hereby certify that I have read this thesis prepared under my direction and recommend that it may be accepted as fulfilling the thesis requirement.

______________________ **Date:** 29th Sept, 2014

Guide : Prof. V. M. Datar

STATEMENT BY AUTHOR

This dissertation has been submitted in partial fulfillment of requirements for anadvanced degree at Homi Bhabha National Institute (HBNI) and is deposited in the library to be made available to borrowers under rules of the HBNI.

Brief quotations from this dissertation are allowable without special permission, provided that accurate acknowledgement of source is made. Requests for permission for extended quotation from or reproduction of this manuscript in whole or in part may be granted by the Competent Authority of HBNI when in his or her judgment the proposed use of the material is in the interests of scholarship. In all other instances, however, permission must be obtained from the author.

Prakash Chandra Rout

DECLARATION

I, hereby declare that the investigation presented in the thesis has been carried out by me. The work is original and the work has not been submitted earlier as a whole or in part for a degree/diploma at this or any other Institution or University.

Prakash Chandra Rout

LIST OF PUBLICATIONS:

In refereed journals:

1. * Measurement of the Damping of the Nuclear Shell Effect in the Doubly Magic ^{208}Pb Region

   P. C. Rout, D. R. Chakrabarty, V. M. Datar, Suresh Kumar, E. T. Mirgule, A. Mitra, V. Nanal, S. P. Behera, V. Singh

   Phys. Rev. Lett. **110**, 062501 (2013).

2. * A large area plastic scintillator detector array for fast neutron measurements

   P. C. Rout, D. R. Chakrabarty, V. M. Datar, Suresh Kumar, E. T. Mirgule, A. Mitra, V. Nanal, R. Kujur

   Nucl. Instrum. Methods Phys. Res., Sect.**A 598**, 526 (2009).

3. Electromagnetic transition from the 4^+ to 2^+ resonance in ^{8}Be measured via the radiative capture in ^{4}He+^{4}He

   V. M. Datar, D. R. Chakrabarty, Suresh Kumar, V. Nanal, S. Pastore, R. B. Wiringa, S. P. Behera, A. Chatterjee, D. Jenkins, C. J. Lister, E. T. Mirgule, A. Mitra, R. G. Pillay, K. Ramachandran, O. J. Roberts, **P. C. Rout**, A. Shrivastava, and P. Sugathan

   Phys. Rev. Lett. **111**, 062502 (2013).

4. Role of the cluster structure of ^{7}Li in the dynamics of fragment capture

   A. Shrivastava, A. Navin, A. Diaz-Torres, V. Nanal, K. Ramachandran, M. Rejmund, S. Bhattacharyya, A. Chatterjee, S. Kailas, A. Lemasson, R. Palit, V.V. Parkar, R.G. Pillay, **P. C. Rout**, Y. Sawant

   Phys. Lett. **B 718**, 931 (2013).

5. Exclusive giant dipole resonance measurement on the Jacobi transition in the ^{19}F+^{27}Al system

   D. R. Chakrabarty, V. M. Datar, Suresh Kumar, G. Mishra, E. T. Mirgule, A. Mitra, **P. C. Rout**, V. Nanal, Deepak Pandit, S. Mukhopadhyay, and Srijit Bhattacharya

   Phys. Rev. **C 85**, 044619 (2012).

*This thesis work is based on these papers

6. Study of fusion in ^{6,7}Li+^{197}Au at near barrier energies

   Shital Thakur, Vivek Singh, C. S. Palshetkar, Vandana Nanal, V. V. Parkar, R. G. Pillay, A. Shrivastava, **P. C. Rout**, K. Ramachandran and A. Chatterjee

   EPJ Web of Conferences **17**, 16017 (2011).

7. Unusual feature of alpha spectra in the ^{12}C+^{93}Nb reaction near Coulomb barrier energies

   E. T. Mirgule, D. R. Chakrabarty, V. M. Datar, Suresh Kumar, A. Mitra, V. Nanal, **P. C. Rout**

   Phys. Rev. C **82**, 064608 (2010).

8. Inhomogeneous and intrinsic damping of giant dipole resonance in hot rotating nuclei with A $\sim$ 150

   D. R. Chakrabarty, V. M. Datar, Suresh Kumar, E. T. Mirgule, A. Mitra, V. Nanal, R. G. Pillay and **P. C. Rout**

   J. Phys. G: Nucl. Part. Phys. **37** 055105 (2010).

9. Broad structures in γ-ray multiplicity gated p and α spectra in low energy ^{12}C+^{93}Nb and ^{16}O+^{89} Y reactions

   A. Mitra, D. R. Chakrabarty, V. M. Datar, Suresh Kumar, E. T. Mirgule, **P. C. Rout**, V. Nanal

   EPJ Web of Conferences **2**, 04004 (2010).

10. Structures in angular momentum gated proton and alpha particle spectra in low-energy ^{12}C and ^{12}O induced reactions

    A. Mitra, D. R. Chakrabarty, V. M. Datar, Suresh Kumar, E. T. Mirgule, V. Nanal, **P. C. Rout**

    J. Phys. G: Nucl. Part. Phys. **36** 095103(2009).

11. Exploring Fusion at Extreme Sub-Barrier Energies with Weakly Bound Nuclei

    A. Shrivastava, A. Navin, A. Lemasson, K. Ramachandran, V. Nanal, M. Rejmund, K. Hagino, T. Ichikawa, S. Bhattacharyya, A. Chatterjee, S. Kailas, K. Mahata, V. V. Parkar, R. G. Pillay, **P. C. Rout**

    Phys. Rev. Lett. **103**, 232702 (2009).

12. Absolute cross-sections from X - γ coincidence measurements

    A. Lemasson, A. Shrivastava, A. Navin, M. Rejmund, V. Nanal, S. Bhattacharyya, A. Chatterjee, S. Kailas, K. Mahata, V. V. Parkar, R. G. Pillay, K. Ramachandran, **P. C. Rout**

    Nucl. Instrum. Methods Phys. Res., Sect.**A 598**,445 (2009).

13. Structure in E1 strength distribution built on 15.1 MeV T=1 state in ^{12}C

    D. R. Chakrabarty, V. M. Datar, Suresh Kumar, E. T. Mirgule, A. Mitra, V. Nanal, **P. C. Rout**

    Physical Review C **77**, 051302(R) (2008).

In national and international Conferences:

1. On the damping of shell effect in ^{208}Pb region using neutron time of flight measurements

   P. C. Rout, D. R. Chakrabarty, V. M. Datar, Suresh Kumar, E. T. Mirgule, A. Mitra , V. Nanal, S. P. Behera , V. Singh

   International Nuclear Physics Conference INPC2013, NR165 (2013).

2. Preliminary results of a more accurate measurement of the radiative 4^+ to 2^+ transition in ^{8}Be

   V.M.Datar, D.R. Chakrabarty, Suresh Kumar, V. Nanal, S.P. Behera , E.T. Mirgule, A. Mitra, K. Ramachandran, **P. C. Rout**, A. Shrivastava, R.G. Pillay, P. Sugathan, C.J. Lister, D. Jenkins, O. Roberts

   International Nuclear Physics Conference INPC2013, NS45 (2013).

3. Inclusive alpha angular distribution in ^{7}Li induced reactions on heavy targets

   P. C. Rout, D. R. Chakrabarty, V. M. Datar, Suresh Kumar, E. T. Mirgule, A. Mitra, A. Shrivastava, V. Nanal, S. P. Behera, G. Mishra, R. Kujur

   Symp. on Nucl. Phys. Vol. **57**,512 (2012).

4. Giant Dipole Resonance width evolution in A 128 mass region

   G. Mishra, D. R. Chakrabarty, V. M. Datar, Suresh Kumar, E. T. Mirgule, A. Mitra, **P. C. Rout**, S. P. Behera, V. Nanal

   Symp. on Nucl. Phys. Vol. **57**,190 (2012).

5. Measurement of direct breakup and transfer-breakup for ^{7}Li+^{93}Nb, ^{89}Y systems around the Coulomb barrier

   S. K. Pandit, A. Shrivastava, K. Mahata, V. V. Parkar, **P. C. Rout**, C. S. Palshetkar, I Martel, Abhinav Kumar, A. Chatterjee, S. Kailas

   Symp. on Nucl. Phys. Vol. **57**, 396 (2012).

6. Dynamics of fragment capture in ^{7}Li + ^{198}Pt

   A. Shrivastava, A. Navin, A. Diaz-Torres, V. Nanal, K. Ramachandran, M. Rejmund, S. Bhattacharyya, A. Chatterjee, S. Kailas, R. Palit, V. V. Parkar, R. G. Pillay, **P. C. Rout**, Y. Sawant

   Symp. on Nucl. Phys. Vol. **57**, 404 (2012).

7. Study of fusion barrier distribution from quasielastic scattering for ^{6,7}Li + ^{197}Au systems

   Shital Thakur, Neha Dokania, V. V. Parkar, V. Nanal, A. Shrivastava, S. Santra, C. Palshetkar, N. L. Singh, **P. C. Rout**, R. G. Pillay

   Symp. on Nucl. Phys. Vol. **57**, 406 (2012).

8. Effect of doubly closed shells on nuclear level density through neutron TOF measurements in the ^{208}Pb region

   P. C. Rout, D. R. Chakrabarty, V. M. Datar, Suresh Kumar, E. T. Mirgule, A. Mitra, V. Nanal, S. P. Behera, V. Singh, R. Kujur

   Symp. on Nucl. Phys. Vol. **56**, 482 (2011).

9. Characterization of a liquid scintillator detector using mono-energetic neutrons.

   P. C. Rout, T Basak, D R Chakrabarty, V M Datar, Suresh Kumar, E T Mirgule, A Mitra, S P Behera, G Mishra, R Kujur

   Symp. on Nucl. Phys. Vol. **56**, 1108 (2011).

10. Alpha particle spectra in ^{12,13}C-induced reactions - dominantly non-statistical at near-barrier energies?

    G Mishra, D R Chakrabarty, V M Datar, Suresh Kumar, E T Mirgule, A Mitra, **P. C. Rout**, R Kujur

    Symp. on Nucl. Phys. Vol. **56**, 454 (2011).

11. Jacobi shape transition from GDR measurements in 19F+ 27Al reaction

    G Mishra, D R Chakrabarty, V M Datar, Suresh Kumar, E T Mirgule, A Mitra, **P. C. Rout**, S P Behera, R Kujur, V Nanal

Symp. on Nucl. Phys. Vol. **56**, 518 (2011).

12. Search for fusion hindrance at deep-sub barrier energies in ^{7}Li + ^{198}Pt

    A Shrivastava, K Mahata, K Ramachandran, S Thakur, S K Pandit, V Nanal, **P. C. Rout**, A Navin, S Bhattacharyya, M Rejmund, C Palshetkar, A Chatterjee, P Patale, S Kailas

    Symp. on Nucl. Phys. Vol. **56**, 542 (2011).

13. Preliminary results from new measurement of the 4^{+} to 2^{+} gamma decay in ^{8}Be

    V. M. Datar, S. P. Behera, D. R. Chakrabarty, A. Chatterjee, D. Jenkins, Suresh Kumar, C. J. Lister, A. Mitra, E. T. Mirgule, V. Nanal, Oliver Roberts, R. G. Pillay, K. Ramachandran, **P. C. Rout**, A. Shrivastava, P. Sugathan

    Proc. of the Symp. on Nucl. Phys. Vol. **55**,2 (2010).

14. Response of long liquid scintillator detector to mono-energetic neutrons

    T. Basak, S. P. Behera, **P. C. Rout**, D. R. Chakrabarty, V. M. Datar, Suresh Kumar, A. Mitra, R. Kujur

    Proc. of the Symp. on Nucl. Phys. Vol. **55**, 714 (2010).

15. Evaporation residue gated GDR studies in ^{19}F +^{27}Al reaction at E(^{19}F)=125 MeV

    D. R. Chakrabarty, V. M. Datar, Suresh Kumar, E. T. Mirgule, A. Mitra, **P. C. Rout**, V. Nanal, Deepak Pandit, S. Mukhopadhyay, Srijit Bhattacharya

    Proc. of the Symp. on Nucl. Phys. Vol. **55**,236 (2010).

16. Transfer reaction studies in ^{7}Li+^{197}Au

    Shital Thakur, Vivek Singh, C. S. Palshetkar, V. Nanal, R. G. Pillay, V. V. Parkar, A. Shrivastava, **P. C. Rout**, K. Ramachandran, A. Chatterjee

    Proc. of the Symp. on Nucl. Phys. Vol. **55**,228 (2010).

17. Three alpha decays of Hoyle state of ^{12}C in ^{12}C + ^{12}C reaction

    T. K. Rana, C. Bhattacharya, S. Kundu, K. Banerjee, S. Bhattacharya, G. Mukherjee, T. K. Ghosh, J. K. Meena, P. Dhara, M. Biswas, H. Pai, K. Mahata, Suresh Kumar, K. Ramachandran, **P. C. Rout**, S. K. Pandit, V. Nanal, R. G. Pillay

    Proc. of the Symp. on Nucl. Phys. Vol. **55**, 230 (2010).

18. Fusion in ^{6}Li+^{197}Au at near barrier energies

    Shital Thakur, Vivek Singh, C. S. Palshetkar, V. Nanal, R. G. Pillay, A. Shrivastava, **P. C. Rout**, K. Ramachandran, A. Chatterjee

    Proc. of the Symp. on Nucl. Phys. Vol. **55**, 294 (2010).

19. On the excitation energy dependence of nuclear level density and damping of shell effect in ^{208}Pb region

    P. C. Rout, D. R. Chakrabarty, V. M. Datar, Suresh Kumar, E. T. Mirgule, A. Mitra, V. Nanal, S. P. Behera, V. Singh, R. Kujur

    Proc. of the Int. Symp. on Nucl. Phys. Vol. **54**, 392 (2009).

20. Compound nuclear origin of broad structures in proton spectra from low energy ^{12}C and ^{16}O induced reactions

    A. Mitra, D. R. Chakrabarty, V. M. Datar, Suresh Kumar, E. T. Mirgule, V. Nanal, **P. C. Rout**, R. Kujur

    Proc. of the Int. Symp. on Nucl. Phys. Vol. **54**, 390 (2009).

21. Isoscaling in ^{13}C + ^{12}C and ^{12}C + ^{12}Creactions at 6MeV/u

    T.K.Rana, C. Bhattacharya, S. Kundu, K. Banerjee, S. Bhattacharya, G. Mukherjee, T.K. Ghosh, J. K.Meena, P. Dhara, M. Biswas, H. Pai, K. Mahata, Suresh Kumar, K. Ramachandran, **P. C. Rout**, S. K. Pandit, V. Nanal, R. G. Pillay

    Proc. of the Int. Symp. on Nucl. Phys. Vol.**54**, 388 (2009).

22. Fusion in ^{7}Li+^{197}Au at sub-barrier energies

    Shital Thakur, Vivek Singh, C. S. Palshetakar, V. Nanal, V.V. Parkar, R.G. Pillay, A. Shrivastava, **P. C. Rout**, K. Ramchandran, A. Chatterjee

    Proc. of the Int. Symp. on Nucl. Phys. Vol. **54**, 316 (2009).

23. A thin wall high vacuum compact chamber for nuclear reaction studies

    Suresh Kumar, V.M. Datar, D.R. Chakrabarty, **P. C. Rout**, R. Kujur

    Proc. of the Int. Symp. on Nucl. Phys. Vol. **54**, 702 (2009).

24. Energy response of plastic scintillator detector to monoenergetic electrons and neutrons

    P. C. Rout, D. R. Chakrabarty, V. M. Datar, Suresh Kumar, E. T. Mirgule, A. Mitra, V. Nanal, and R. Kujur

    Proc. DAE-BRNS Symp. on Nucl. Phys. Vol. **53**, 735 (2008).

25. A segmented annular PPAC to tag fusion residues by time of flight

    Suresh Kumar, **P. C. Rout**, V. M. Datar, R. Kujur, V. Nanal, A. Mitra, E. T. Mirgule, and D. R. Chakrabarty

    Proc. DAE-BRNS Symp. on Nucl. Phys. Vol. **53**, 691 (2008).

26. Characterization of a long, pulse shape discriminating liquid scintillator detector

    David Dennetiere, V. Nanal, **P. C. Rout**, D. R. Chakrabarty, V. M. Datar

    Proc. DAE-BRNS Symp. on Nucl. Phys. Vol. **53**, 707 (2008).

27. Giant dipole resonance studies in ^{28}Si + ^{124}Sn reaction at E(^{124}Sn)=188 MeV

    D. R. Chakrabarty, V. M. Datar, Suresh Kumar, E. T. Mirgule, A. Mitra, V. Nanal, R.G. Pillay, **P. C. Rout**, R. Kujur, M. S. Pose

    Proc. DAE-BRNS Symp. on Nucl. Phys. Vol. **53**, 219 (2008).

Prakash Chandra Rout

To

my teachers,

my maternal grand-parents

and

my family

ACKNOWLEDGEMENTS

I take this opportunity to thank all who have contributed in some way or other in shaping my life and those who inspired and peered during my thesis work.

First and foremost, I would like to express my deep and sincere gratitude to my thesis supervisor, Dr. V.M. Datar, for his guidance and constant encouragement during this journey. My special thanks to Dr. D.R. Chakrabarty who taught me valuable knowledge that an experimentalist should have. I am very fortunate to get both of them as my mentors since the beginning of research work. I would like to express my gratitude and thanks to Dr. Suresh Kumar for his encouragement and constant support for completion of this work. I appreciate them for valuable physics discussions and critical proof reading of the thesis. I would like to thank Dr. E.T. Mirgule, Dr. A. Mitra for their encouragement, moral support and valuable discussion throughout this work.

My special thanks to my doctoral committee members: Dr. A. K. Mohanty, Dr. V. Nanal, Dr. B. N. Jagtap for their valuable comments and critical evaluation for completion of the thesis work. I thank Dr. S. S. Kapoor and Dr. R. K. Choudhury for their valuable suggestions. I would like to thank Dr. A. Chatterjee, Dr. A. Navin, Dr. B.K. Nayak, Dr. S. R. Jain, Dr. R.G. Pillai and Palit-bhai for valuable physics discussions and encouragement.

I would like to thank my friends at Van de Graaff, Aradhana, Kripa-da, Santra-da, Jha-bhai, Ramachandran, Bidyut-da, Vivek, Sanat, Shiba, Gaurava, Yogesh and Renju for their affection, immense support and encouragement. The help of Rajendra, Parui-da, H. H. Oza, Mahesh, Prasant and Nitali during the experiment are gratefully acknowledged. I would also like to thank the NPD office staff and each and every member of NPD for their help during this period. I wish to thank the Pelletron Linac staff for smooth operation of the machine and target laboratory staff for helping in target preparation during all the experiments.

I would like to take this opportunity to thank all my teachers from school to university who imparted value education and moral courage. I am also very fortunate to have loving and friendly teachers during my graduate and postgraduate courses. My special thanks to Mr. Praffulla Sahoo (Gopabandhu Science college), Prof. Swadhin Pattanayak (Institute of Mathematics) and Prof. Niranjan Barik (Utkal University) for motivating me towards Physics.

To all my friends who make my life a wonderful experience, thank you for your understanding and encouragement throughout. I cannot list all the names here, but you are always on my mind.

My deepest gratitude to my parents for their love and support throughout my life. Thank you Maa for giving me strength to reach for the stars and chase my dreams. Damayanti-didi, Bikash, Kedar, Kiran deserve my wholehearted thanks as well. I also thank all my relatives especially Mama (Krushna-mamu), main (aunt) and Kalia-mamu for their support and being there by my side throughout. I would like to express my gratitude to my father and mother-in-law for their help during the PhD work. Last, but not the least, I thank my loving and supportive wife, Puja and my love for my daughter, Guddu (Pratyusha) who missed me at home while I was busy in the thesis work.

Thank you, Lord Jagannath, for always being there for me.

Contents

List of Figures

List of Tables

SYNOPSIS

Shell effect is the manifestation of the finite fermionic systems such as atoms and nuclei. This plays an important role in describing the structure and the properties of the matter. The electronic shell structure in atoms decides the chemical properties of the corresponding elements and defines the architecture of the modern periodic table. In analogy to the atomic shell structure, the nuclei with closed nucleon shell have a significantly greater stability with respect to the neighbouring nuclei. These nuclei are more stable than that predicted by the liquid drop model (LDM). The heaviest stable doubly magic nucleus is ^{208}Pb with Z=82 and N=126 (Z, N are proton number and neutron number respectively). There are many important nuclear phenomena such as the occurrence of super heavy elements fission isomers, super-deformed nuclei and new magic numbers in exotic nuclei which are the consequences of the shell effect.The shell effect also affects the nuclear level density (NLD). The NLD is a fundamental property of the nucleus and a crucial input to the statistical calculation of compound nuclear decay. This is thus an important physical quantity for many practical applications, such as the calculations of reaction rates relevant to nuclear astrophysics, nuclear reactors and spallation neutron sources. The NLD is defined as the number of energy levels per MeV at excitation energy (E_X). The dependence of the NLD on the excitation energy and angular momentum (J) was first derived by Bethe using Fermi gas model [1, 2]. The generic behaviour with respect to E_X is described by $e^{2\sqrt{aE_X}}$. Here *'a'* is the NLD parameter which is related to the single particle density at the Fermi energy. The experimental evidences of the nuclear level density are obtained from (a) counting the discrete levels and resonances populated by neutron and charged particle reactions, (b) the inelastic scattering of neutron, proton, alpha and transfer reaction populating the low excitation energy, (c) the Ericson fluctuation analysis in the compound nuclear reaction which is restricted to light mass nuclei (A$\leq$60) and (d) the analysis of evaporation spectra [3]. In the first two methods the NLD is obtained by direct counting of the nuclear levels with necessary correction for unresolved and unobserved levels and therefore provide an absolute measure of the nuclear level density. The information of the NLD is limited to near stable nuclei and very low excitation energy (up to binding energy of the nucleon) and angular momentum of few $\hbar$ (mainly s and p wave). The extrapolated to higher J values is made to estimate the angular momentum summed or total NLD. The last method does not provide the absolute value of the NLD, but has been used to study its variation over wide range of the excitation energy and the angular momentum. The total NLD inferred from various measurements show that on an average the level density parameter a increases linearly with the mass number of the nucleus as $a \approx$A/8 MeV^{-1}. This smooth behaviour with respect to mass is due to the liquid drop like properties of the nucleus. However, there is a significant departure from this liquid drop value at shell closures. This departure is the largest for the doubly magic nucleus ^{208}Pb, where the effective a is as low as A/26 MeV^{-1} at $E_X \sim B_n$ (neutron binding energy). This shell effect on the NLD parameter is expected to wash out with excitation energy so that a approaches its liquid drop value at $E_X \geq 40$ MeV [4]. There is no measurement in this important topic to address the washing out of the shell effect over a wide E_X range. The main obstacle is population of the doubly closed shell nucleus ^{208}Pb at low excitation energy, using a suitable projectile and target combination, where the shell effect is important. This is because of the large Coulomb barrier in the entrance channel that is relevant for a heavy ion fusion reaction. For instance, The extracted NLD in ^{208}Pb from the measurement of the proton evaporation spectra in ^{10,11}B+^{198}Pt reactions showed liquid drop behaviour at an excitation energy $\sim$ 50 MeV [5]. The level densities of $^{205˘208}$Pb at low excitation energy (up to 6 MeV) were obtained using the Oslo method, which involves the measurement of the continuum γ-ray spectra following the ^{3}He induced inelastic scattering and single nucleon transfer reactions [6, 7]. However, the damping of the shell effect over wide range of excitation energy has not yet been addressed.

One possible method to populate ^{208}Pb at low excitation energy is the triton transfer/breakup-fusion in the ^{7}Li induced reaction on ^{205}Tl target. In this method, the populated intermediate nucleus is assumed to be in thermal equilibrium and emits particles such as p, n, α and gamma rays as per the statistical model of compound nuclear decay. We can then measure the neutron spectra from the excited ^{208}Pb nucleus in coincidence with the out-going alpha particles. The energy of the alpha particle has a correspondence with the excitation energy in the ^{208}Pb. This exclusive measurement of neutrons is meaningful as the α-yield is not small. A feasibility experiment was carried out to ascertain the alpha production cross section in such reactions. The time resolution of the pulsed ^{7}Li beam from the Pelletron was also measured as it was important for the neutron time of flight (TOF) measurement. The angular distributions of alpha production in the ^{7}Li induced reaction on heavy targets were measured and the measured total cross sections show a universal behaviour near the barrier energies. The total α cross section in ^{7}Li + ^{205}Tl at 30 MeV is found to be $\sim$40 mb. The time resolution of the pulsed ^{7}Li beam was measured with respect to γ-rays detected in a BaF_2 detector and found to be better than 1.5 ns. Since the intrinsic efficiency of the neutron detector is very small, we require a large angular coverage for the neutron detectors and also need an efficient charged particle detector system for measurement of alpha particles. We have setup a large area plastic scintillator array for fast neutron measurement and also an array of CsI(Tl) detectors for the detection of alpha particles. These detector systems are briefly described in the following paragraphs.

Large area neutron detector array:

Plastic scintillators have been widely used for neutron measurements by the TOF technique because of their fast response. A long scintillator detector (6×6 cm^2 cross section) with photomultiplier tube (PMT) at either ends is used to get position information from the timing signal from both the PMTs [8]. We have set up a neutron detector array ($\sim 1\times1$m^2) at the Mumbai Pelletron Linac Facility (PLF), which consists of 16 plastic scintillator bars of square cross section [9]. Each bar has a dimension 6 cm$\times$6 cm$\times$100 cm and is coupled to two 5 cm diameter XP2020 PMTs, one each at either end. The array will be used for fast neutron spectroscopy and also for any measurement in coincidence with neutrons. The characterization of the plastic detector was done using radioactive sources and also for mono-energetic and continuum neutrons using beams from the PLF. The energy, time and position response has been measured for quasi-mono-energetic electrons using Compton tagging of scattered γ-rays and for mono-energetic neutrons using the ^{7}Li(p,n$_1$)^{7}Be*(0.429 MeV) reaction at proton energies between 6.3 and 19 MeV. The array has been used to measure the evaporation neutron spectrum from 4 to 12 MeV in the reaction ^{12}C+ ^{93}Nb at E(^{12}C)= 40 MeV and the measured neutron spectrum compares well with the statistical model calculation. A Monte Carlo simulation algorithm has been developed in-house to simulate the neutron energy dependent efficiency of the array. The Monte Carlo simulated efficiency of the plastic scintillators for the neutron detection agrees with that obtained from the ^{7}Li(p,n$_1$) measurements. Add-ons for the neutron detector array are : (a) Lead (Pb) sheets of total thickness 25 mm placed in front of the array to reduce the low energy γ-ray background while not significantly attenuating the neutrons from the target and (b) a 30 cm thick shadow pyramid consisting of several plates of mild steel (MS) shield used to estimate the contribution due to the scattered neutrons.

CsI(Tl) detector array for efficient α measurement:

An array of 8 CsI(Tl) detectors with active area of 2.5 cm $\times$ 2.5 cm and thickness of 1 cm has been assembled to detect the light charged particles with a reasonably large efficiency. The scintillation light is collected by a silicon PIN photodiode (PD) and pre-ampllifier coupled to the CsI(Tl) detectors. The PD is more efficient than a photo multiplier tube (PMT), requires less voltage to operate and is very compact. The detectors are covered with an aluminised mylar foil of thickness $\sim$1 μm. The standard pulse shape discrimination method is used for the particle identification by measuring the zero cross over timing (ZCT) of the amplified bipolar pulse . These detectors have nonlinear energy response for various particles. The energy response of the CsI(Tl) detectors to α-particles has been measured from 8.5-25 MeV using a ^{229}Th source and the ^{12}C(^{12}C, α)^{20}Ne reaction at E(^{12}C) = 24 MeV populating discrete states in ^{20}Ne. The energy non-linearity and the count rate effect on the PSD property has also been measured and it was found that the PSD deteriorates for count rate $\geq$3 kHz.

We would now address the question pertaining the shell effect and its damping with excitation energy in the double closed shell nucleus ^{208}Pb. The exclusive neutron spectra from ^{208}Pb have been measured in coincidence with ejectile alpha particles. The nucleus ^{208}Pb, formed in the excitation energy range 19 - 23 MeV, decays predominately by the neutron emission populating the residual nucleus in the $E_X \sim 3$ - 14 MeV. Over this E_X range, the NLD parameter is expected to show a significant change due to the damping of the shell effect. We have also made a controll measurement with a ^{181}Ta target populating nuclei in the ^{184}W region where the shell effect is expected to be small. The statistical model(SM) analysis of the measured neutron spectra demonstrate the expected large shell correction energy for the nuclei in the vicinity of doubly magic ^{208}Pb and a small value around ^{184}W. Furthermore, the detailed analysis of the neutron spectra from ^{208}Pb in various excitation energies within the frame work of statistical model of compound nuclear decay using the phenomenological NLD prescription [10], the damping parameter (γ) and asymptotic level density parameter($\tilde{a}$) were constrained for a fixed shell correction energy. The shell correction energy was taken as 13.1 and 11.7 MeV for ^{207}Pb and ^{206}Pb, respectively. An exclusion plot between the damping parameter and the inverse level density parameter δa (= $A/\tilde{a}$) has been made for the first time. It is observed that the acceptable range of δa lies between 8.0 and 9.5 MeV. The parameter γ controlling the damping of the shell effect can be constrained to $(0.060^{+.010}_{-.020})$ MeV^{-1} [11]. This is different from the value extracted from the neutron resonance data within errorbars *viz*. (0.079 ± 0.007) MeV^{-1} [12].

The thesis is organized into five chapters. Chapter 1 describes the historical perspectives of the magic nuclei and shell effect and experimental evidences of the shell effect. This chapter also introduces the nuclear level density and the important physical parameter characterizing the NLD. The motivation and structure of the thesis work is described.

Chapter 2 describes the detector arrays developed for the measurement of the fast neutrons and alpha particles. The details of the neutron detector array and the characterization with radio active sources and beams are described. A brief description of the Monte Carlo simulation for the energy dependent efficiency is also presented. The second part of this chapter describes the charged particle array developed for the measurement of light charge particles using the PSD technique. The detailed characterization of the CsI(Tl) detectors such as energy non-linearity, PSD and count rate effects will be described.

The third chapter includes a brief description of the PLF. The other part of this chapter will be devoted to the measurement of nuclear level density and the study of nuclear shell effect and its damping with the excitation energy.

The statistical model of compound nuclear reaction is briefly discussed in the fourth chapter. The results are discussed within the frame work of the statistical model.

Chapter 5 contains the summary and conclusions. The future outlook including possible improvements pertaining to the study of the nuclear shell effect in NLD will be described.

Bibliography

[1] H. A. Bethe, Phys. Rev. **50**, 332 (1936).

[2] A. Bohr, B. R. Mottelson, Nuclear Structure (Benjamin, New York,1969), Vol.**1**.

[3] D. Chakrabarty, V. Datar, S. Kumar, E. Mirgule, H. Oza, and U. Pal, Phys. Rev. C **51**, 2942 (1995) and its references.

[4] V. S. Ramamurthy, S. K. Kataria, S. S. Kapoor, Phys. Rev. Lett. **25**, 386 (1970).

[5] G. Viesti et al., Pramana- J. of Phys. Vol. **53** 395(1999).

[6] E. Melby, et al., Phys. Rev. Lett. **83**, 3150 (1999).

[7] N. U. H. Syed et al., Phys. Rev. C **79**, 024316 (2009).

[8] G. Charpak, L. Dick, L. Feuvrais, Nucl. Instr. and Meth. 15 (1962) 323.

[9] P. C. Rout, D. R. Chakrabarty, V. M. Datar, Suresh Kumar, E. T. Mirgule, A. Mitra, V. Nanal, R. Kujur, Nucl. Instrum. Methods Phys. Res., Sect.**A** **598**, 526 (2009).

[10] A. V. Ignatyuk, G.N. Smirenkin, A.S. Tishin, Sov. J. Phys. **21**, 255 (1975).

[11] P. C. Rout, D. R. Chakrabarty, V. M. Datar, Suresh Kumar, E. T. Mirgule, A. Mitra, V. Nanal, S. P. Behera, V. Singh, Phys. Rev. Lett. **110**, 062501 (2013).

[12] S. F. Mughabghab, C. Dunford, Phys. Rev. Lett. **81**, 4083 (1998).

1

Introduction

1.1 Historical perspective

The nucleus is a many body quantum system composed of nucleons, namely neutrons and protons. These nucleons are bound by an attractive, short range nuclear force. The stability of the nucleus is determined by the competition between attractive nuclear force and the repulsive Coulomb force due to the charged protons while at the same time respecting the Pauli principle. The saturation property of the nuclear force and the low compressibility of the nucleus suggest an analogy with a charged liquid drop. The liquid drop model (LDM) of the nucleus describes the average properties of the nucleus, i.e. the nuclear binding energies and is also useful in explaining the phenomenon of nuclear fission. The systematics of the binding energy of nuclei show an evidence of the presence of shell structure of the nuclei like the electronic shell structure of atoms. Nuclei with the closed shell configuration (proton number Z and/or neutron number N equal to the magic numbers 2, 8, 20, 50, 82 and 126) have an extra stability with respect to that expected from the LDM. The successful explanation of these nuclear magic numbers via a large spin-orbit splitting led to the Nobel prize in Physics for Goeppert-Mayer and Jensen. ^{208}Pb with 82 protons and 126 neutrons is the heaviest known doubly closed shell stable nucleus. The shell correction energy, which is a measure of shell effect, is defined as the difference between the experimental mass and the liquid drop mass (the LDM without shell correction). The shell effect influences many physical phenomena such as formation of super heavy nuclei, fission isomer, super-deformed nuclei etc. There is also a strong correlation between the shell effect and the nuclear level density (NLD), a fundamental property of the nucleus.

The following sections of this chapter briefly describe the shell effect and how to estimate the shell correction energy. This is followed by the discussion on the NLD and the phenomenological description of the shell corrected nuclear level density. The motivation and structure of the thesis are also presented.

1.2 Nuclear Shell effect

Nuclear shells correspond to an inhomogeneous distribution of nucleons in phase space. The non-uniformities in the single particle spectrum associated with the shell structure imply that the nuclear energy does not vary smoothly with particle number, as in the LDM, but exhibits specific variations depending on the degree of filling of the shells. The crucial issue is to separate between the smooth behavior associated with the bulk property and the more specific effects due to the nuclear shell structure, which is contained in the sum of the single-particle energies. The method of estimating the shell correction energy was given by Strutinsky [1] and a similar concept was developed independently by Myers and Swiatecki for spherical nuclei [2]. The basic idea of the Strutinsky method is the concept of separating the

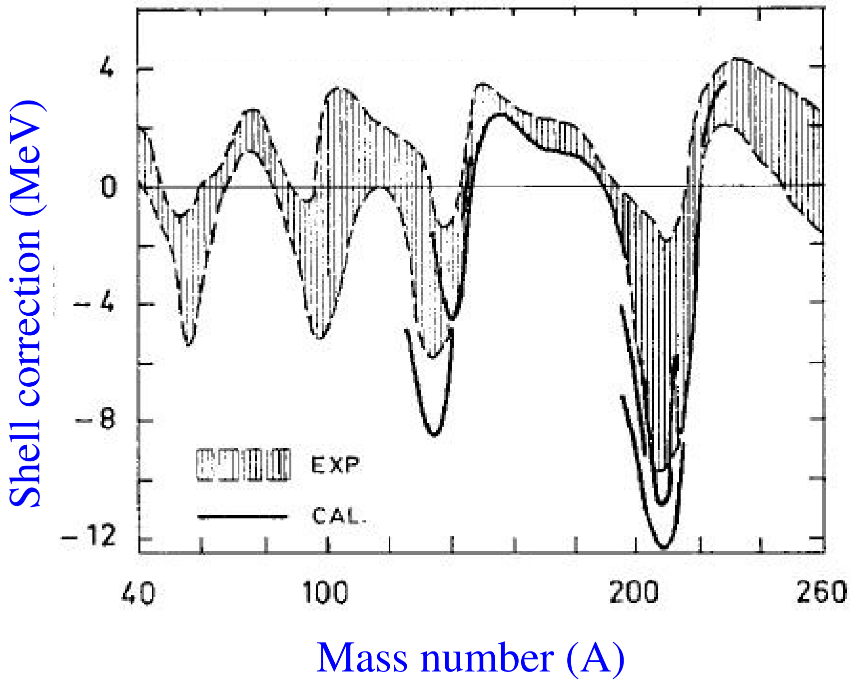

Figure 1.1: The total shell correction energies to the nuclear ground-state masses, as calculated by Strutinsky, are compared to the deviations of experimental masses from an LDM mass referring to spherical nuclei [6].

smooth components from fluctuating ones due to the nuclear shell structure. The total nuclear energy may be written as E = $\tilde{E}+\ \Delta_S$, $\tilde{E}$ representing the smooth part and Δ_S is the fluctuating part attributed to the shell effect. The $\tilde{E}$ can be calculated using the 'macroscopic' LDM and Δ_S which is also called 'the shell correction energy' can be determined from the single particle energies. Strutinsky defined a smoothed single particle level density $\tilde{g}$(e) by smearing the calculated single-particle levels e_ν over an energy range of the order of the shell spacing ($\sim$41$A^{-\frac{1}{3}}$ MeV). The single particle level density of actual discrete level structure $g(e)$ can be estimated as $g(e) = \sum \delta(e - e_\nu)$ and the smoothed level density $\tilde{g}$(e) can be obtained by smearing the discrete levels with a Gaussian smearing

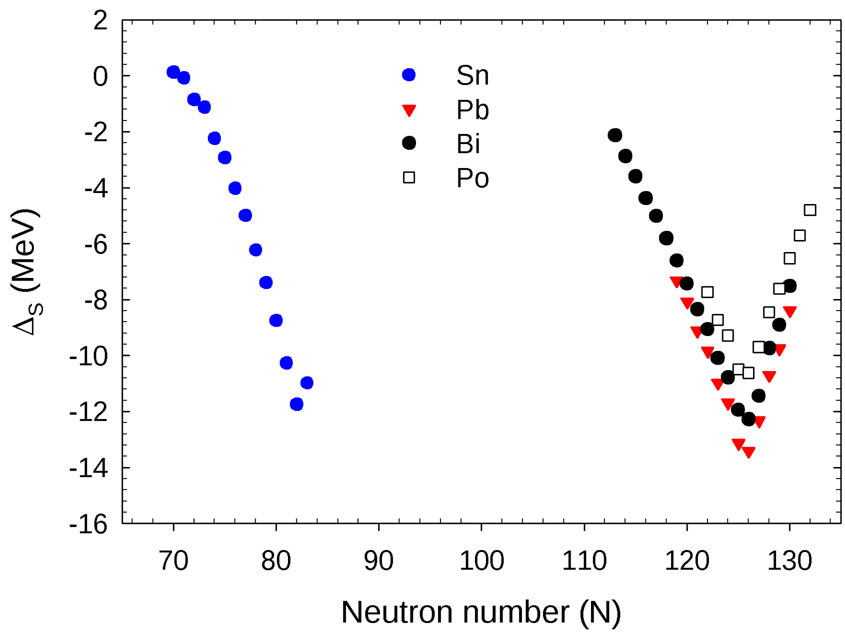

Figure 1.2: Shell correction energy calculated from the M_{exp} and M_{LDM} for Sn, Pb, Bi and Po isotopes.

function [1, 3]. The shell correction energy [4, 5] can be calculated as

$$\Delta_S = 2\sum e_\nu - 2\int e\tilde{g}(e)de$$

where $\tilde{g}$(e) is assumed to be Gaussian function. The Strutinsky's method of calculating the shell correction energy works well in practice and has been used successfully to describe quantitatively the ground state energies and the associated equilibrium deformations. The figure 1.1 shows calculated shell correction energies compared with the observed difference between the LDM masses and the empirical masses. Many prescriptions for calculating the shell correction energy are available in the literature.

The interpretation of the shell-structure terms in the nuclear masses was given by Myers and Swiatecki [2]. The observed masses show deviations from the LDM masses that are correlated with the nuclear shell structure. The semi-empirical mass equation of a nucleus with Z protons and N neutrons is $M_{obs} = M_{LDM} + M_{shell}$. For a spherical nucleus M_{shell} is same as shell correction energy (Δ_S) and for the deformed nucleus Δ_S is multiplied by an attenuation factor $e^{-(distortion)^2/c^2}$, where c is a parameter related to the range of the nuclear interaction. The attenuating factor makes the shell correction disappear with increasing distortion of the nucleus. The shell correction generally changes from negative values in the vicinity of magic numbers to positive values in between.

The shell correction energy was derived by considering the fact that the observed magic configuration is the result of the bunching of the single-particle levels into groups separated by gaps. The shell correction energy defined as the difference between the sum over single-particle contributions in the bunched and unbunched cases:

$$\Delta_S = \sum \epsilon_i(\text{bunched}) - \sum \epsilon_i(\text{unbunched}),$$

where ϵ_i is the single-particle energy calculated using suitable nuclear potential as in case of nuclear shell model. However, in practice the shell correction energy is calculated from the measured and the LDM nuclear masses. The shell correction is usually defined as $\Delta_S = M_{exp} - M_{LDM}$, where M_{exp} is the experimental mass and M_{LDM} is the nuclear mass calculated using the LDM [7]. The variation of shell correction energy with neutron number for Sn, Pb, Bi, and Po isotopes as calculated by Myers and Swiatecki is shown in Fig. 1.2. The shell correction energy is large near the Pb region and is maximum, -13.4 MeV, for the doubly magic ^{208}Pb. It may be noted that the shell correction energy is also sizable near the doubly magic ^{132}Sn region.

1.3 Experimental evidences of the shell effect

The regularities and correlations in the compiled data from various experimental results provides the information about the shell structure of the nucleus. Some experimental evidences of the existence of shell structure in nuclei are: (a) The abundance plot by Goldschmidt in the region of heavy elements shows peaks at nuclei: Zr (N=50), Sn (Z=50), Ba (N=82) and Pb (Z=82 or N=126) [8], (b) The compilation of mass defects of the nuclei and binding energy per nucleon plot against the mass number shows a number of significant local variations near the magic numbers, (c) The experimental neutron capture cross sections exhibit fluctuations from isotope to isotope. The nuclei having 50, 82 and 126 neutrons have lower cross section by a factor of fifty than neighboring nuclei, (d) The sharp discontinuity in the neutron and proton separation energies reveal the nuclear shell structure just as observed in the ionization potentials of atom, (e) The systematic of the first excited 2^+ state in even-even nuclei show the maxima at the shell closings [9].

1.4 Nuclear level density

The nuclear level density (NLD) is a fundamental property of the many body quantum system. The level density is an indispensable input to the statistical model of compound nuclear (CN) decay and thus an important physical quantity for many practical applications. Its wide spread applications include the study of fission hindrance in heavy nuclei, the giant dipole resonance built on excited states, the yields of evaporation residues to populate certain exotic nuclei, production of heavy elements in stellar processes etc. Apart from the practical needs, the study of the NLD provides a fundamental insight into the microscopic feature of an excited nucleus. The NLD is also an important quantity for the determination of thermodynamical properties of nuclei, such as entropy, temperature and heat capacity.

The (NLD) is defined as the number of energy levels per unit energy at an excitation energy E_X. It increases rapidly with excitation energy. The NLD has a smooth behaviour with respect to mass (A) due to the liquid drop like properties of the nucleus. It also has a quantum mechanical dependence which exhibits an oscillatory behaviour with respect to A due to shell effects. In general, the level density depends on various physical quantities, e.g. excitation energy, number of particles, angular momentum, parity, isospin, shell effect, pairing etc. The extensive work on both the theoretical and experimental investigations of nuclear level densities addressing various microscopic aspects of nucleonic motion is summarised in Refs. [10, 11].

The number of energy levels in a nucleus between an excitation energy E_X and $E_X+\mathrm{d}E$ and at an angular momentum J is $\rho(E_X, J)\mathrm{d}E$ where $\rho(E_X, J)$ is the level density. Each level of total angular momentum J has $2J+1$ degenerate states. Thus, the state density $\omega(E_X, J)$, which counts all $2J+1$ states, can be represented as $\omega(E_X, J) = (2J+1)\rho(E_X, J)$. There are three main theoretical methods used to understand the nuclear level density from the single particle levels: (a) thermodynamic approach [12, 13], based on the grand partition function which contains all the statistical information of the nucleus, (b) combinatorial method [14], which is basically an enumerative method requiring large scale computation to estimate the number of ways the nucleons can be distributed among the available single particle levels and sorting them according to a given excitation energy and angular momentum, and (c) spectral distribution method [15, 16], which uses the fact that the shell model state densities have nearly Gaussian distribution, the energy and angular momentum dependent level density being evaluated from the first few moments (centroid, width, skewness etc.) of the nuclear Hamiltonian. Recently developed a powerful shell model Monte Carlo (SMMC) method [17, 18], which has been used to calculate the nuclear level density in the presence of correlations. The SMMC method enables calculations in model spaces that are many orders of magnitude larger than those that can be treated by conventional methods. This method was employed to calculate the level densities of $^{59-64}$Ni (including the odd-mass isotopes) and deformed nucleus ^{162}Dy [19, 20]. These results found to be in good agreement with the level density extracted from various experiments.

The NLD was first calculated by Bethe using a non-interacting Fermi gas model. The simplest picture is the equidistant model where the single particle levels are equi-spaced and non-degenerate. The density of states for a system composed of two kinds of particles (neutron and proton) is given in analytical form by [13]:

$$\omega(E_X) = \frac{\pi}{12}\frac{\exp(2\sqrt{aE_X})}{E_X^{5/4}a^{1/4}} \tag{1.1}$$

where, a is known as the level density parameter and is given by $a = \pi^2 g/6$ and g is the sum of the neutron and proton single particle level density at the Fermi surface. This result is only the zeroth order approximation to the level density of a Fermi gas. In a Fermi gas, the single particle level density increases approximately as the square root of the particle kinetic energy, while in this model it is a constant. The thermodynamical quantities, entropy and temperature, can be obtained from the above expression. The entropy and the nuclear temperature are given by

$$S = \ln\omega \tag{1.2}$$

$$\frac{1}{T} = \frac{d\ln\omega}{dE_X} \tag{1.3}$$

Therefore, the nuclear temperature is given by

$$\frac{1}{T} = (\frac{a}{E_X})^{1/2} - \frac{5}{4E_X} \tag{1.4}$$

At high E_X limit, the nuclear temperature is $(E_X/a)^{\frac{1}{2}}$. Since $a = (E_X/T^2)$, the argument of the exponential in ω is proportional to E_X/T. It turns out that the experimental level density at low energy is described well by the expression

$$\rho(E_X) \propto \exp(E_X/T) \tag{1.5}$$

where T is constant. This formula is usually referred as constant temperature formula.

In general, the E_x and J dependent nuclear level density is used in most of the statistical model analysis of the experimental data involving heavy ion reaction. The level density for a given angular momentum and both parity states is:

$$\rho(E_X, J) = \frac{2J+1}{12}\sqrt{a}\left(\frac{\hbar^2}{2\Im}\right)^{\frac{3}{2}} \frac{1}{(E_X - E_{rot})^2}\exp[2\sqrt{a(E_X - E_{rot})}\ ] \tag{1.6}$$

where $E_{rot} = (\hbar^2/\Im)J(J+1)$ and $\Im$ is the rigid body moment of inertia. $\Im$ is related to the average square of single particle angular momentum projection ($< m^2 >$) by $\Im = \hbar^2 g < m^2 >$. The rotation energy(E_{rot}) is not available for intrinsic excitation. It is therefore excluded while calculating the NLD.

The nuclear level density so far discussed is based on the equidistant model of the single particle level in a Fermi gas system. However, the shell model single particle levels has a complex variation in its level spacings. The non-uniformity in the single particle level spacing leads to correction in the nuclear level density due to the shell structure. The shell effects tend to disappear with increasing E_X. The shell effect on the NLD of nuclei with a sizable shell correction can be addressed experimentally. In addition, the residual interactions such as pairing and the collective modes of excitation such as rotation and vibration can also alter the energy dependence of the nuclear level density.

The information on the nuclear level densities are usually obtained from: (a) the neutron and charged particle resonances, (b) the inelastic scattering and the transfer reactions populating the low E_X states, (c) the Ericson fluctuation analysis in the compound nuclear reactions and (d) the particle evaporation from the compound nuclear reactions.

Neutron and charged particle resonances

Neutron resonance data [22, 23] provides the crucial information on level densities in the vicinity of the neutron binding energy. The NLD is obtained from the observed nuclear energy levels by counting the resonances in a particular neutron energy interval. An important requirement for such experiments is that the width Γ of each level should be less than the level spacing D and the detector resolution should be good enough to resolve individual levels. The level density ρ is proportional to D^{-1}. The counting of resonances must be corrected for levels missing because of counting statistics and resolution effect. Recently, CERN has devel-

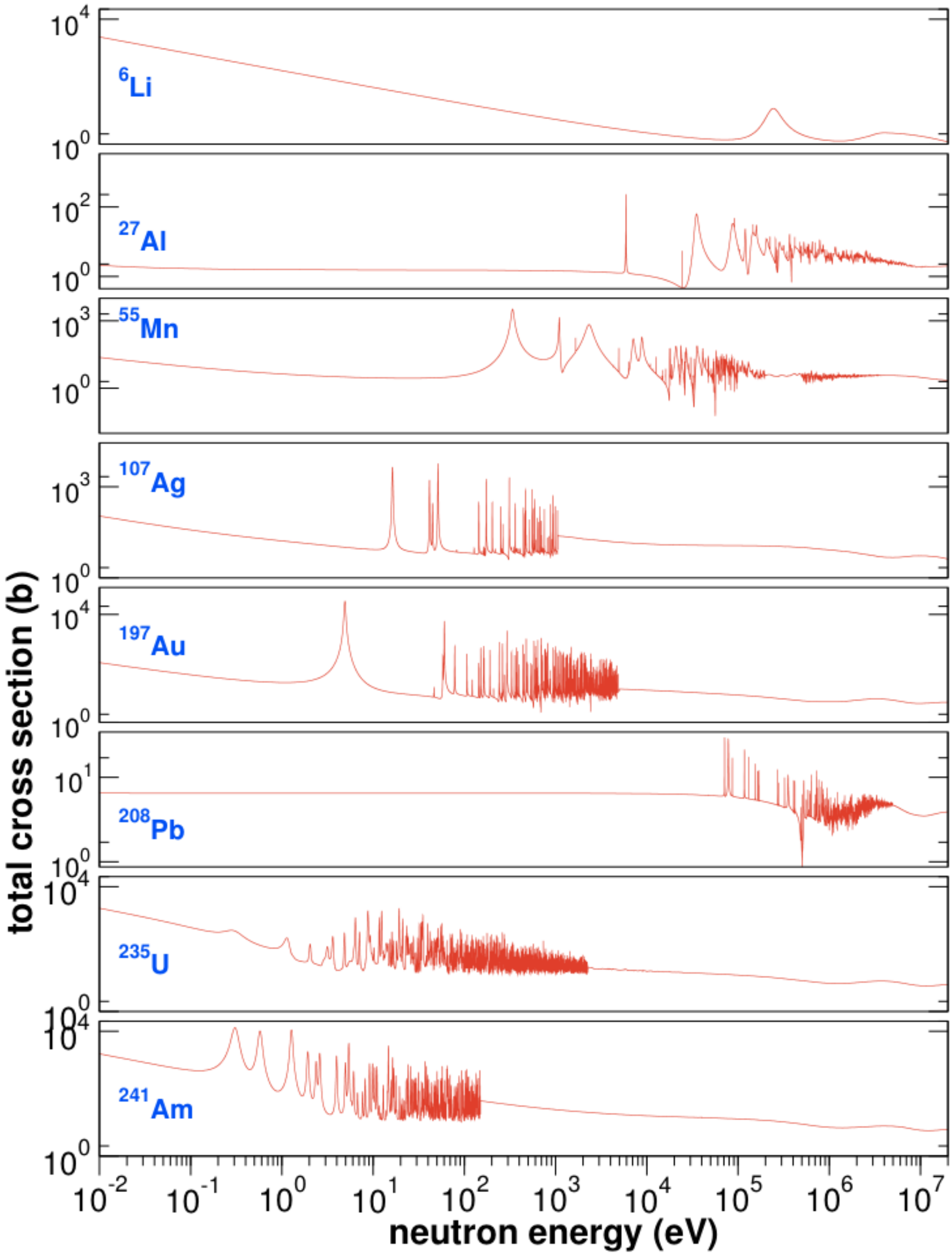

Figure 1.3: Total cross section measured by neutron capture resonance spectroscopy from ^{6}Li to ^{241}Am using the CERN n-TOF experiment [24].

oped a neutron time of flight (n-TOF) facility for low energy nuclear physics to investigate nuclear structure at high excitation energies from neutron resonance spectroscopy. The total cross-section measured in CERN n-TOF experiment as a function of neutron energy for several nuclei with increasing mass ranging from ^{6}Li to ^{241}Am is shown in Fig 1.3 [24]. The observed spacing between two levels decreases which implies that the level density increases as mass of the nucleus increases. A significant shell effect is observed for the doubly closed shell ^{208}Pb nucleus.

The level density measured from neutron resonances is limited to a single energy region just above the neutron binding energy and for one or two values of angular momentum. Information on the level density from charged-particle capture resonances are obtained in a similar way. The charged particle resonance data are restricted to light and medium nuclei due to the Coulomb barrier and the NLD information is limited to nuclei around A$\sim$60.

Inelastic scattering and transfer reactions:

The neutron and charged-particle resonance spectroscopy used to obtain the NLD in the compound nucleus, requires high resolution experimental techniques. The NLD has been studied also in residual nuclei at lower energies by excitation through inelastic scattering and a variety of other nuclear reactions. Typical nuclear reactions employed for the study of the level density are (p, p$'$), (n, n$'$), (α, α') and (p, α) reactions. It is possible to obtain nuclear level density for the nucleus with A$\sim$60 at an E_X $\sim$5-6 MeV [25, 26].

Recently, a method of extracting level density and γ-ray strength function has been developed by the Oslo cyclotron group [27]. This method employs to measure the continuum γ-ray spectra following inelastic scattering and transfer reactions, namely (^{3}He, ^{3}He$'\gamma$) and (^{3}He, ^{4}Heγ). The primary γ-ray spectra at an E_X is obtained from the decay probability $P(E_X, E_\gamma)$ which depends on the the level density $\rho(E_X - E_\gamma)$ and the γ-ray strength function. The analysis of the energy distribution of the primary γ-rays emitted from a nucleus at a given E_X thus reveals information on both the level density at the E_X and the γ-ray strength function. This method employs to investigate the nuclear level density and hence the thermodynamical properties of rare earth nuclei. For instance, the ^{3}He induced inelastic scattering and single nucleon transfer reaction were used to populate $^{205-208}$Pb and the energy dependence of the NLD was extracted from the coincident γ spectrum up to $\mathrm{E}_X \sim 6$ MeV [28].

Ericson fluctuation method [29]:

Measured nuclear reaction cross sections at a compound nuclear excitation energy E_X ~20 MeV fluctuate as a function of projectile energy [30, 31]. The counting method for the nuclear levels fails for the energy region where the average width Γ is larger than the average spacing D between the CN levels. The Γ can be obtained from correlation functions of the fluctuating cross sections. The density of levels in the CN may be obtained from the statistical theory as $\rho = N/2\pi\Gamma$, where N is the total number of open channels. The quantity $\Gamma\rho$ or Γ/D can be determined from the experiment by measuring the energy averaged compound nuclear cross section. The measurement of Γ and average cross section can provide the information of D and ρ.

Particle evaporation method:

The information on variation of the NLD with E_X can be obtained from the statistical model analysis of measured particle evaporation spectrum [10]. This technique does not provide an absolute measurement ρ but is used to study its variation over a wider range of E_X and J. The extraction of the NLD from the particle evaporation spectra in the heavy-ion reactions has some advantages over other techniques are, the possibility of studying the NLD in a variety of nuclei with suitable combination of projectile and target, and over a wide range of E_X and J. Moreover, the contribution from pre-equilibrium process is negligible in heavy-ion reaction with beam energy $\leq$5 MeV/n. The difficulty involved in this method is due to the fact that the particle evaporation spectra is a result of multi-step decay process, thus sampling many nuclei at different steps leading to an average NLD. This can be overcome by restricting the first step contribution to the particle evaporation from a CN at moderate E_X. The level density in light and heavy mass nuclei have been obtained from the measured particle spectra within the frame work of statistical model of the compound nuclear reaction [32, 33, 34, 35, 36].

1.5 Shell corrected Nuclear level density

It may be noted that only a few single particle levels in the vicinity of the Fermi surface contributes to the NLD. As nucleons are added, the Fermi surface moves from the region of low single particle density at magic nucleus to the region of high single particle density at mid-shell nucleus. Thus a variation of the single particle density g (or the level density parameter a) with mass number can show the shell effect at moderate excitation energy (see Fig 1.3). Direct measurements of the

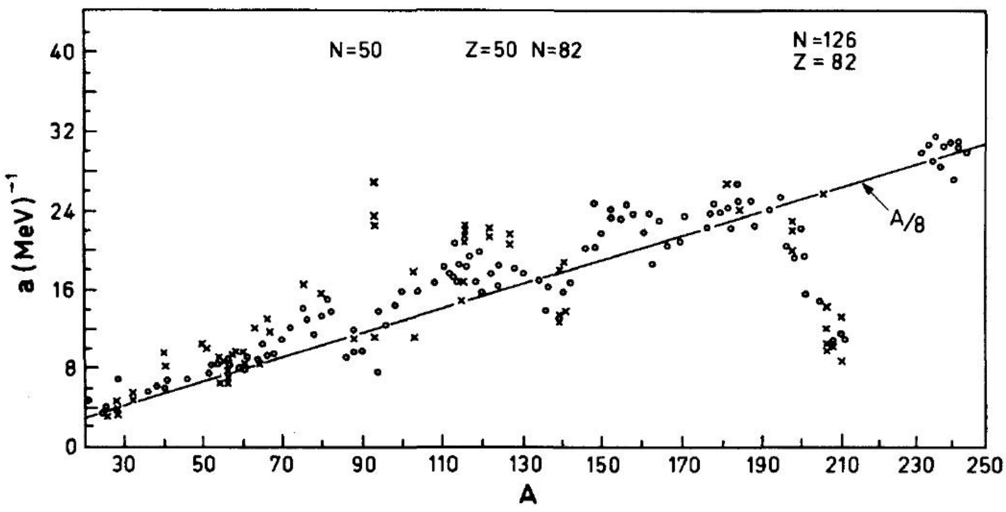

Figure 1.4: Variation of the nuclear level density parameter a with mass number A [13] determined from various experimental techniques.

NLD are based on the study of slow neutron resonances, which are mainly s- and p-wave, and are extrapolated to higher J values to estimate the angular momentum summed or total NLD. The total NLD inferred from such a measurement shows that on an average the level density parameter a increases linearly with the mass number (A) of the nucleus as a $\approx$A/8 MeV^{-1}. However, there is a significant departure from this liquid drop value at shell closures. This departure is the largest for the doubly magic nucleus ^{208}Pb, where a (at E$_X$ $\sim$7 MeV) is as low as A/26 MeV^{-1} as shown in Fig 1.4. This shell effect on the NLD parameter is expected to damp with excitation energy so that a approaches its liquid drop value at E$_X$ $\sim$ 40 MeV [37]. Figure 1.5 shows how the shell effects on nuclear entropy ($S^2 = 4aE_X$, S being the nuclear entropy) disappear even at medium excitation energies of the order of 40 MeV.

The general form of the NLD with all microscopic nuclear effects in order to explain the experimental data is far from reality. The analytic form for the

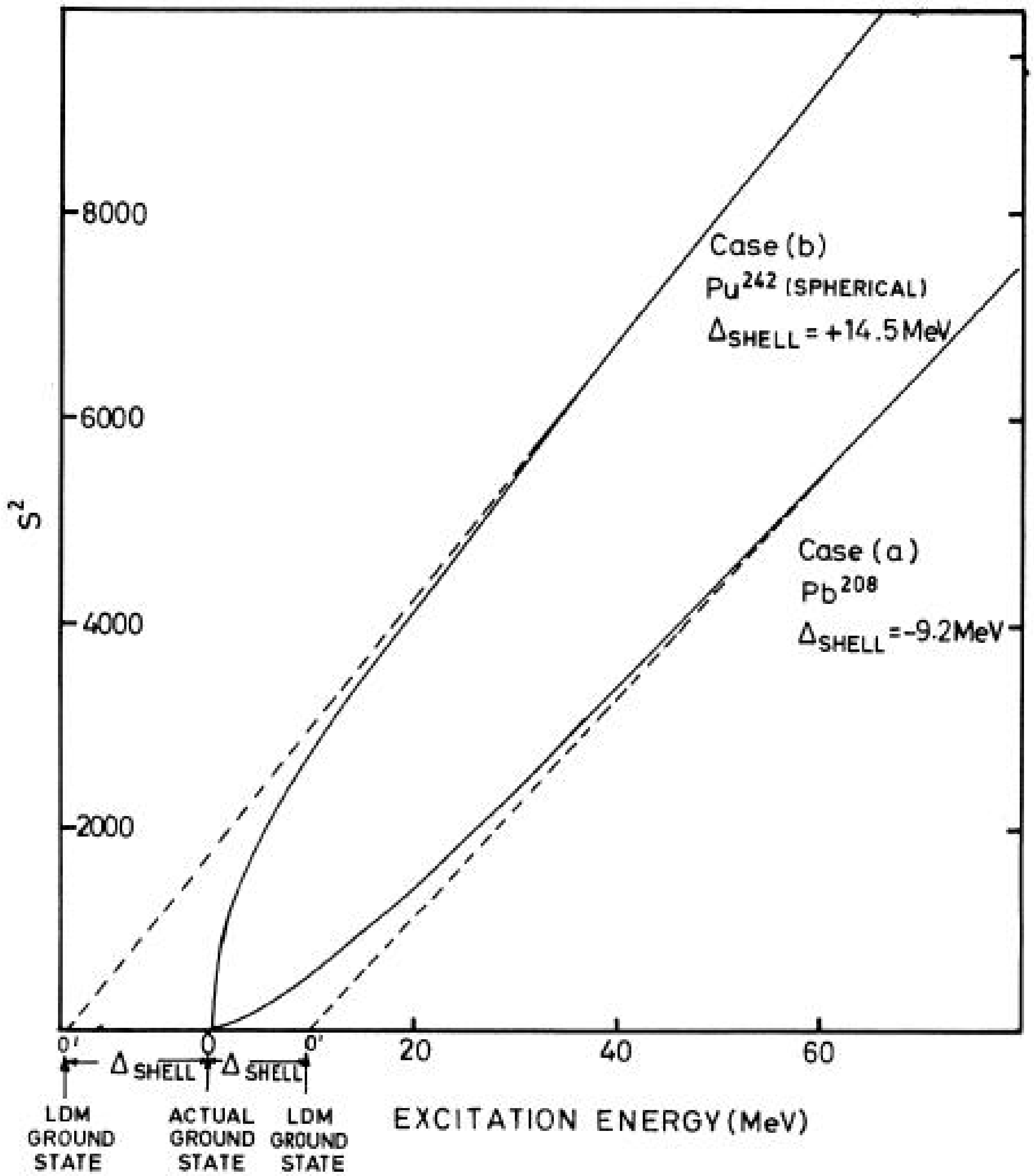

Figure 1.5: The variation of entropy with excitation energy for the case of doubly magic nucleus ^{208}Pb and the nucleus ^{242}Pu [37].

level density resulted from the pioneer work of Bethe is normally used to explain most of the experimental data. Bethe's formula is not adequate to explain all the microscopic feature but is used as a basis to build the phenomenological NLD expression which includes all known nuclear structure effects such as shell effects, odd-even effects, collective enhancements etc. The phenomenological expression for NLD, used in the statistical model (SM) for the analysis of the particle spectra, is given by :

$$\rho(E_X, J) = \frac{2J+1}{12}\left(\frac{\hbar^2}{2\Im}\right)^{3/2}\frac{\sqrt{a}}{U^2}e^{2\sqrt{aU}}, \tag{1.7}$$

where

$$U = E_X - E_{\text{rot}} - \Delta_P, \tag{1.8}$$

and

$$E_{\text{rot}} = \left(\frac{\hbar^2}{2\Im}\right)J(J+1), \tag{1.9}$$

where Δ_P is the pairing energy and $\Im$ is the moment of inertia. The excitation energy dependence of the NLD parameter a, which includes the shell effect and its damping, has been parameterised by Ignatyuk [38] as:

$$a = \tilde{a}\left[1 - \frac{\Delta_S}{U}(1 - e^{-\gamma U})\right] \tag{1.10}$$

Here $\tilde{a}$ is the asymptotic value of the NLD parameter in the liquid drop region, Δ_S is the shell correction energy, which is calculated as discussed earlier and γ is the damping parameter.

1.6 Motivation and structure of the present thesis

The Nuclear Level Density (NLD) is a basic property of the nucleus. Apart from the fundamental interest e.g. transition from order to chaos, it is a key parameter for any statistical model calculation. Many measurements have been done to explore how level density varies with the excitation energy (E_X) and angular momentum (J) in different mass region. The level density ($\rho(E_X, J)$) extracted from the experimental data shows a lower value near the shell closure i.e. the large departure of level density parameter (a) from the what is predicted by the Fermi gas model. However, so far there is no direct measurement reported on the damping of nuclear shell effect over a wide excitation energy range or a critical energy where the shell effect vanishes.

There is a long standing prediction which shows the shell effect on nuclear level density vanishes with excitation energy beyond 40 MeV. To understand the phenomenon in detail we would like to measure the variation of the shell effect on NLD as a function of excitation energy around the doubly closed shell ^{208}Pb where this effect is expected to be more pronounced. One way to populate this nucleus at low excitation energy is via triton transfer in ^{7}Li induced reaction on ^{205}Tl. The transfer process has a sizable cross section in the mass region of our interest and the coincidence measurement of neutrons with the ejectile would be possible with a suitable detector system for both neutrons and the alpha particles. The statistical model analysis of measured neutron evaporation will reveal the more physical insight for the understanding the variation of shell effect. The physical parameters relevant to the the damping factor and the level density parameter will be extracted from the measured data at various excitation energies. A control experiment using ^{181}Ta target will be carried out for comparison which populate the ^{184}W away from the the closed shell nucleus. The thesis is organized into five chapters as follows:

Chapter 1 describes the historical perspectives of the magic nuclei and shell effect and experimental evidences of the shell effect. This chapter also introduces the nuclear level density and the important physical parameter characterizing the NLD. The motivation and structure of the thesis work is described.

Chapter 2 describes the detector arrays developed for the measurement of the fast neutrons and alpha particles. The details of the neutron detector array and the characterization with radioactive sources and beams are described. A brief description of the Monte Carlo simulation for the energy dependent efficiency is also presented. The second part of this chapter describes the charged particle array developed for the measurement of light charge particles using the PSD technique. The detailed characterization of the CsI(Tl) detectors such as energy non-linearity, PSD and count rate effects are also described.

Chapter 3 includes a brief description of the pelletron linac facility (PLF). This is then followed by the detailed description of the experiments conducted for the measurement of nuclear level density, and the study of nuclear shell effect and its damping with the excitation energy.

Chapter 4 briefly discusses the statistical model of compound nuclear reaction. The statistical model analysis of the experimental results are discussed. The extracted parameters related to the damping of shell effect are presented.

Chapter 5 contains the summary and conclusions. The future outlook including possible improvements pertaining to the study of the nuclear shell effect in NLD is presented.

2

Detector Array for the Measurement of Neutrons and Charged Particles

2.1 Introduction

The conversion of the energy deposited by incoming particles or radiation into photons can lead to particle detection, energy determination and discrimination between particles of different masses. Historically, Rutherford first used a ZnS screen in his α-scattering experiments for counting alpha particles. When alpha particles hit the screen, they produced scintillations which were counted visually with the aid of a microscope. However with the advancement of photo sensitive devices such as the photomultiplier tube (PMT) and Si-photodiodes (PD), it is possible to amplify the tiny scintillation light produced in the scintillation process and convert it to an electronic signal which is amenable to further processing leading to a better characterization of the energy deposited by the charged particle.

The function of a scintillator is twofold: first, it converts the excitation of the medium caused by the energy loss of a particle into visible light, and second, it transfers this light either directly or via a light guide to PMT or PD for a detectable signal. Scintillator materials can be organic compounds, liquids, gases and inorganic crystals. The detailed review of the physical principles and characteristics of scintillation detectors are explained elsewhere [39, 40, 41].

The production of light in organic scintillators is the result of molecular transitions. The ionizing radiation passing through the scintillator excites the molecule to an excited state (A_1 in Fig 2.1). The transition from A_1 to B_1 takes place through lattice vibrations (that energy is eventually dissipated as heat). Then, the excited state B_1 decay to the ground state B_0 by emitting the photon. A large class of organic scintillators is based on the organic molecules with π-electron structure as shown in Fig 2.1.

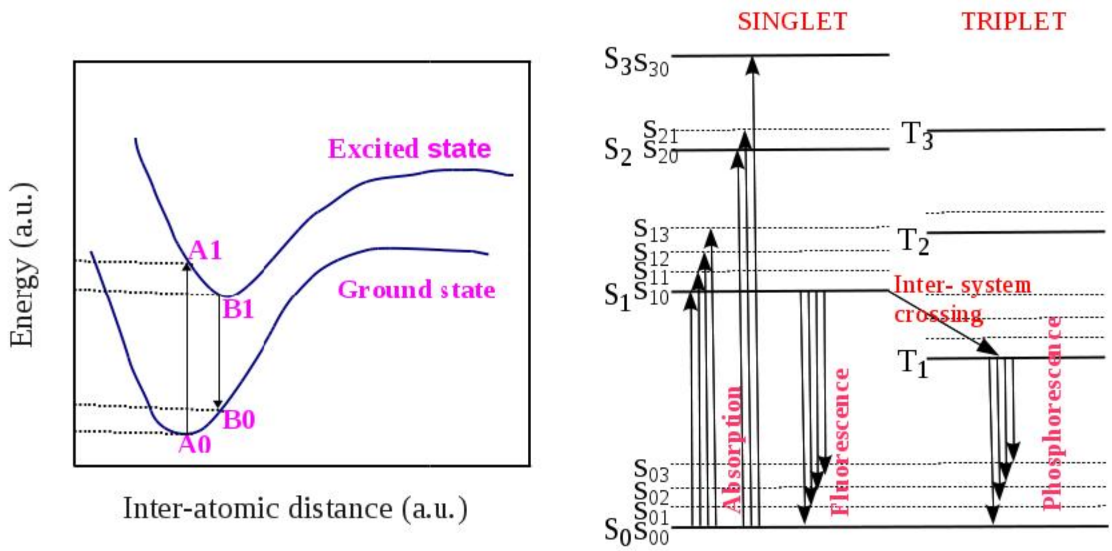

Figure 2.1: Typical energy diagram and π-electron structure of an organic molecule.

Energy from a charged particle is absorbed and excites the electron into a variety of excited singlet states (spin = 0) labeled S_1, S_2, S_3 . For organic scintillators

Table 2.1: Some organic scintillating material (SM) and their properties (SP).

Type	Plastic	Liquid	Loaded Plastic	Loaded Liquid
SM / SP	EJ-200	EJ301	EJ254	EJ331
Density (g/cm^3)	1.02	0.874	1.03	0.89
H/C ratio	1.104	1.212	1.17	1.31
Emission wavelength (nm)	425	425	425	424
Decay time (ns)	2.1	3.2	2.2	4
Refractive index	1.58	1.51	1.58	1.5
Light output (%) vs Anthracene	64	78	48	60
Commercial equivalent	BC-408 PilotF	BC-501A NE213	BC454	BC521 NE323
Application	TOF counters	PSD Liquid fast n-γ discrimination	B loaded, neutron studies	Gd ($\sim$1%) loaded, neutron spectroscopy

the spacing between S_0 and S_1 is 3 to 4 eV, whereas the spacing between the upper states is much smaller. Each of the S levels is subdivided into a series of levels with much finer structure (corresponding to the vibrational states of the molecule). The typical spacing is 0.15 eV. The second subscript is to distinguish between the vibrational states. At room temperature, all molecules are in the S_{00} state as the thermal energy is approximately 0.025 eV . When the charged particle passes through the scintillator, it loses its energy and excites electrons to the upper levels. The higher states deexcite quickly ($\sim$ps) to the S_1 state through radiationless transitions. States such as S_{11}, S_{12} that have extra vibrational energy quickly lose energy. After a negligibly short time a population of excited molecules in S_{10} state is produced as the net effect of the excitation process. The transition between S_{10} and one of the vibrational states of the ground electronic state gives rise to the principal scintillation light or the prompt fluorescence. The light emitted from the deexcitation from T_1 to S_0 is the phosphorescence. The wavelength of this phosphorescence spectrum is longer than that for fluorescence. Some examples of the organic scintillators are listed in the Table 2.1.

The mechanism of scintillation for inorganic scintillators is a lattice effect. The passage of a charged particle through the crystal may produce ionization in the crystal if the incoming particle transfers sufficient energy to the electrons in the valence band to move to the conduction band, leaving a hole in the valence band (Fig 2.2). If the incoming energy is not enough to raise the electron from the

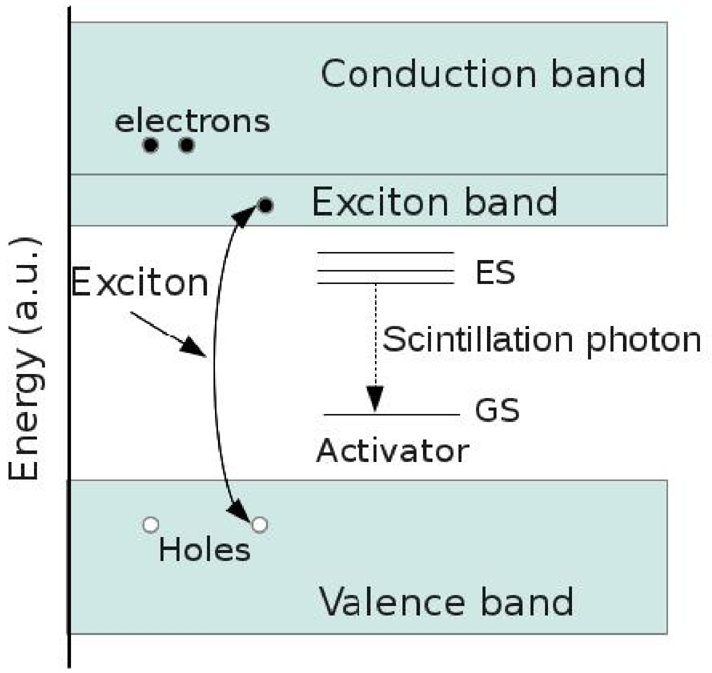

Figure 2.2: Energy bands of a crystal

valence band then the electron may form a bound state with a hole. This bound state is called an exciton and located in an exciton band below the conduction band. Finally, there exist activator centers in the scintillator which occupy energy

Table 2.2: Properties of some inorganic scintillators(IS).

Properties \ IS	BGO	BaF_2	CsI(Tl)	$LaBr_3$(Ce)
Density (g/cm^3)	7.13	4.88	4.53	5.29
Radiation length (cm)	1.12	2.05	1.85	1.88
dE/dx (MeV/cm)(for mip)	9.2	6.6	5.6	6.9
Decay time (ns)	300	0.6, 620	1000	20
Emission wavelength (nm)	480	220, 310	550	356
Refractive index	2.2	1.56	1.8	1.9
light yield (per MeV)	8×10^3	10^4	5×10^4	6×10^4

levels in the gap, between the conduction and the valence bands. When a charged particle passes through the scintillator medium it generates a large number of free electrons, free holes and electron-hole pairs which move around in the crystal lattice until they reach an activator center. Then they transform the activation center into an excited state. The subsequent decay of this excited state to the activator center ground state produces light. Some examples of inorganic scintillators without an activator are BGO ($Bi_4Ge_3O_{12}$), BaF_2 and pure CsI. NaI(Tl) or CsI(Tl) requires the presence of thallium (Tl) as an activator for the production of luminescence. Inorganic scintillators have a higher density and atomic number compared to organic scintillators. These scintillators have high absorption for γ, X-rays and also for charged particles. These detectors have rather short radiation lengths, between 0.9 and 2.6 cm, and densities from 3.7 up to 8.3 g/cm^3. The properties of some inorganic scintillators used in the experiment are given in the table 2.2.

2.2 Fast neutron detection

Neutron being a neutral particle cannot be detected directly unlike charged particle which interacts by electromagnetic interaction. It has to generate a charged particle through nuclear reactions which can be detected. Thus, the neutron induced reactions are the basis for neutron detection in which neutron is converted directly to the detectable charged particles. The common reactions used for slow neutron detection are ^{3}He(n,p), ^{10}B(n, α), ^{6}Li(n, α) and fission with fissile targets. The cross sections of neutron induced reactions are shown in Fig. 2.3 [40]. The cross section (σ) of the slow neutron induced reaction decreases with increasing energy(E_n) as $\sigma \propto 1/\sqrt{E_n}$. Thus, the conventional slow neutron detectors based on these reactions have very low detection efficiency for fast neutrons. The most common method for the detection of fast neutrons is elastic scattering of neutrons by light particles. It is required in many practical applications to detect the fast neutron in presence of γ-rays or other low energy background. The pulse shape discrimination (PSD) or time of flight (TOF) method is used for the discrimination of neutron induced event from the γ-ray induced events.

If a neutron of energy E_n undergoes elastic scattering with target nucleus of mass number A, then the recoil energy (E_R) can be obtained using 2-body kinematics as follows,

$$E_R = \frac{4A}{(1+A)^2} E_n cos^2\theta, \tag{2.1}$$

where θ is the scattering angle of the recoil nucleus in lab system. The transfer of neutron energy to the recoil nucleus will depend on the mass of the target nucleus. As mass of target nucleus increases, the fractional energy transfer decreases. The neutron transfers about half of its energy, on the average, in a single encounter if

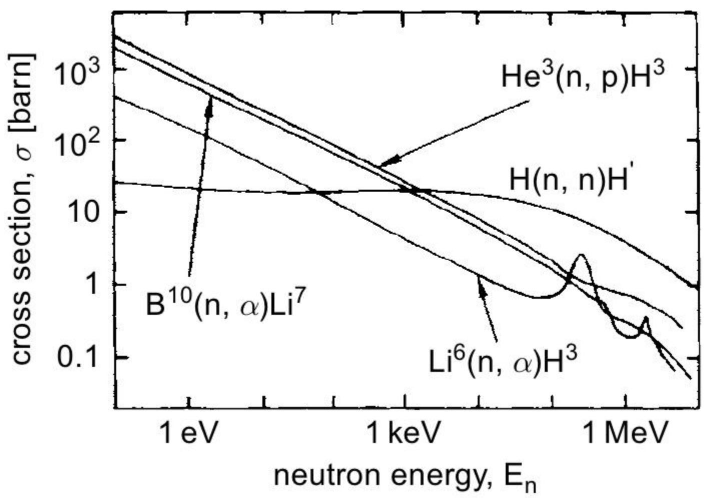

Figure 2.3: Energy dependent cross sections of neutron induced reactions.

the target is hydrogen. Thus, a high hydrogen content material such as organic scintillator is important for efficient fast neutron detection.

2.3 Neutron Detector array

The measurement of neutron spectra is important in many nuclear reaction studies. One example is the study of the statistical decay of compound nuclei populated in low energy fusion reactions. In particular, it is interesting to make a measurement in the ^{12}C+^{93}Nb reaction because an unusual structure has been reported in the angular momentum gated proton and alpha spectra in this reaction at E(^{12}C) = 40 and 42.5 MeV [42]. This would require measurements of neutron spectra down to ~ 0.1 μb sr^{-1} MeV^{-1} with an energy resolution ~ 10 %. A large area neutron detector is needed to meet these requirements. Another example of interest is the study of shell effects, and their damping with excitation energy, on the nuclear level density(NLD) in the region of doubly closed shell nuclei. The variation of NLD for a wide range of the N/Z ratio, where N and Z are the neutron and proton numbers in a nucleus, using radioactive ion beams is an interesting topic that can be addressed. A large neutron detector array would also be useful in coincidence measurements involving neutrons, e.g. study of fission dynamics and neutron decay following the transfer reaction.

Plastic scintillators have been widely used for neutron measurements by the time of flight (TOF) technique because of their fast response and the relatively low cost, enabling the construction of a large detector system. A long scintillator detector with photomultiplier tubes (PMTs) at either end was first used by Charpak et al.[43]. While economizing on the number of PMTs for a given areal coverage, the detector was shown to have good TOF and position resolution using the timing information from both the PMTs. An array consisting of a number of such long scintillators stacked one above the other is a cheaper and simpler alternative to an array of a larger number of discrete detectors with a comparable efficiency. For example, a 1 m^2 array with 16 bars of cross section 6 cm $\times$ 6 cm needs 32 PMTs of 5 cm diameter. An array of similar overall dimensions but more granularity could have 256 plastic scintillators each of size 6 cm$\times$6 cm and would require 256 PMTs. An array of 49 square plastic scintillators of size 14 cm$\times$14 cm could be viewed by 12.7 cm diameter PMTs or 5 cm diameter PMTs with light guides. Either option would increase the complexity and cost of the detector system. We have chosen to set up a 1 m$\times$1 m plastic detector array consisting of 16 long scintillators.

Figure 2.4: A photograph of the plastic scintillator detector array taken with 15 bars.

2.3.1 Description of Neutron Detector Array

The neutron detector array consists of 16 plastic scintillator bars (equivalent to Bicron BC-408 and procured from SCIONIX, Holland) of square cross section[44]. Each bar has a dimension 6 cm$\times$6 cm$\times$100 cm and is coupled to two 5 cm diameter XP2020 PMTs, one each at either end. The scintillator has a light output of $\sim$ 65% compared to that of anthracene, a scintillation decay time of $\sim$4 ns and a bulk attenuation length $>$ 3 m. The polyvinyl toluene based plastic scintillator was used which has a carbon to hydrogen ratio of $\sim$1:1.1. The density and refractive index of the scintillator are 1.03 gm/cm^3 and 1.58, respectively. The spectral sensitivity of the XP2020 PMT peaks at 420 nm, with a quantum efficiency of $\sim$

25%, and matches the emission spectrum of the plastic scintillator. The PMTs have a fast response time (rise time $\sim$1.3 ns) and a gain of $\sim 10^7$ at about 2 kV bias voltage. The PMTs are powered by a 32 channel programmable high voltage power supply developed in-house [45]. The plastic scintillators are stacked one above the other on a stand with wheels for horizontal movement of the array and a four bolt arrangement to adjust the height and level. A photograph of the array is shown in Fig. 2.4.

Lead (Pb) sheets of total thickness 25 mm can be placed in front of the array to shield the low energy γ-ray background while not significantly attenuating the neutrons from the target. Apart from the target neutrons directly reaching the detector, there are those following a circuitous path, such as scattering from various materials in the experimental hall. In order to compare the contributions from these two sources, a 30 cm thick mild steel (MS) shield consisting of several plates of increasing transverse dimension was fabricated. This can be placed near the target to block the target neutrons from reaching the array. The measurements with and without the MS shield allows an estimation of the contribution due to the scattered neutrons that are not in the line of sight of the target.

2.3.2 Time, position and energy response

The important parameters deduced from the time and integrated charge of the PMT signals are as follows

(a) The time of flight(TOF), derived from left and right PMT trigger times

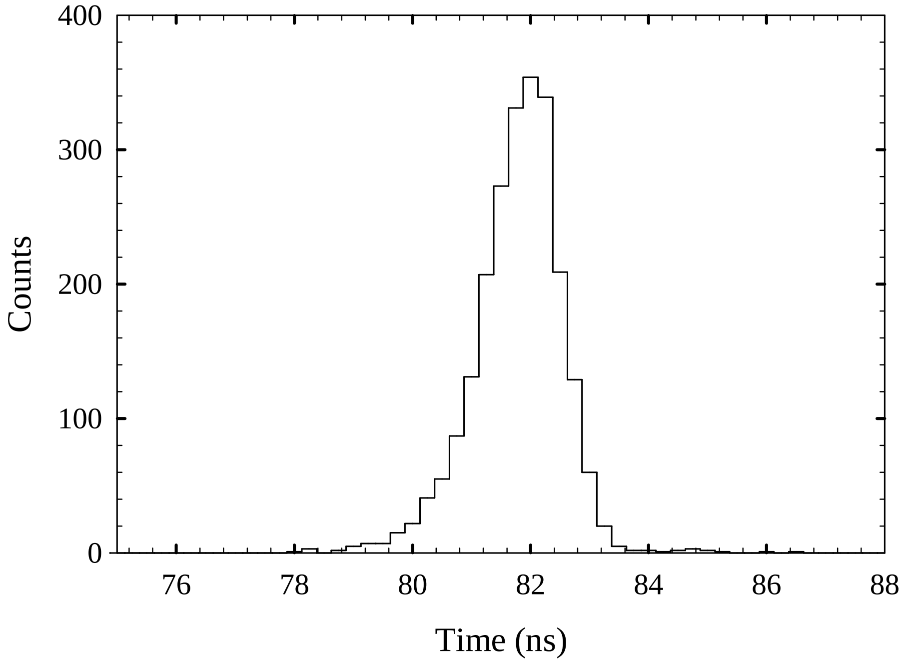

Figure 2.5: TOF spectrum,with an arbitrary offset(see eq.1) derived from the left and right time (T_L,T_R) of PMTs by exposing the centre of the detector to 511 keV photons from a ^{22}Na source.

(T_L, T_R), with respect to a reference time, is given by

$$TOF = (T_L + T_R)/2 + T_{offset} \tag{2.2}$$

where T_{offset} is independent of the position of the interaction point.

(b) The position (X) of interaction point is obtained from the time difference between T_L and T_R

$$X \propto (T_L - T_R). \tag{2.3}$$

In addition, the position information can also be obtained from the integrated

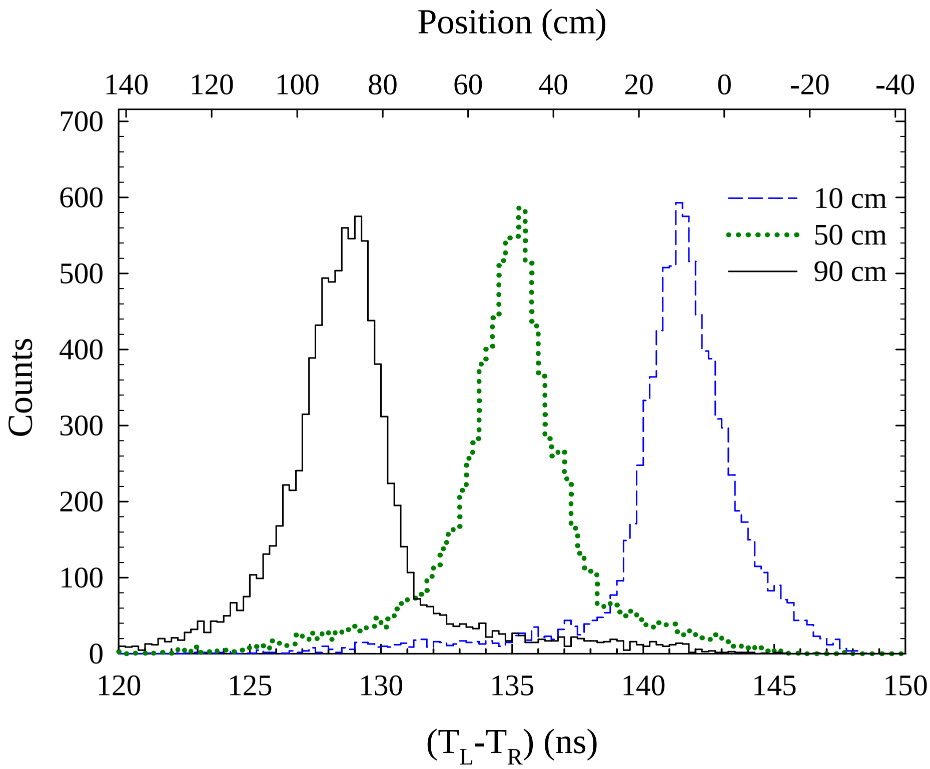

Figure 2.6: Position response measured by exposing $\sim$ 1 cm wide portion along the length of the scintillator bar, using lead collimators and a ^{22}Na γ-ray source, for various distances of the exposed part from one end. The upper axis shows the distance calculated using the fit shown in Fig. 2.7. The lower axis shows the measured time difference (T_L-T_R).

charges of the left and right PMT signals (Q_L, Q_R) as

$$X \propto ln\,\frac{Q_L}{Q_R}. \tag{2.4}$$

(c) The integrated charge information is necessary for the determination of

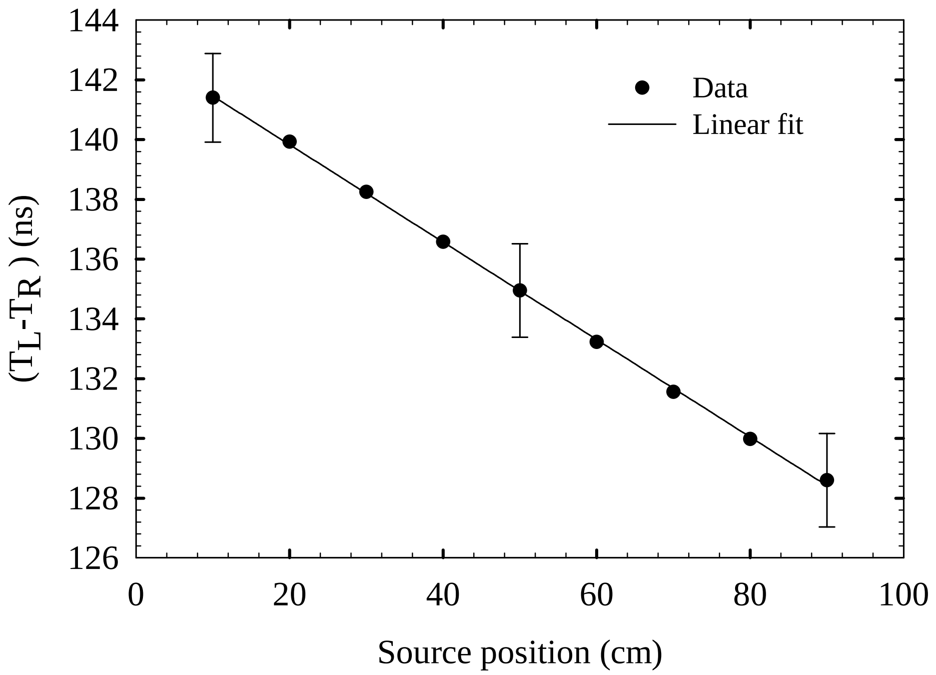

Figure 2.7: Measured ($T_L - T_R$) for various source positions along the length of the scintillator. The vertical lines (shown only for three points) represent FWHM of the position response shown in Fig. 2.6.

neutron detection efficiency. The geometrical mean Q_{GM} of two signals

$$Q_{GM} = \sqrt{Q_L \, Q_R} \tag{2.5}$$

is roughly independent of the position and is proportional to the energy deposited in the detector (see for example Ref.[46]).

Response to electrons

The time, position and energy response of the plastic scintillator was measured with collimated γ-rays from various radioactive sources. The 511 keV γ-ray from

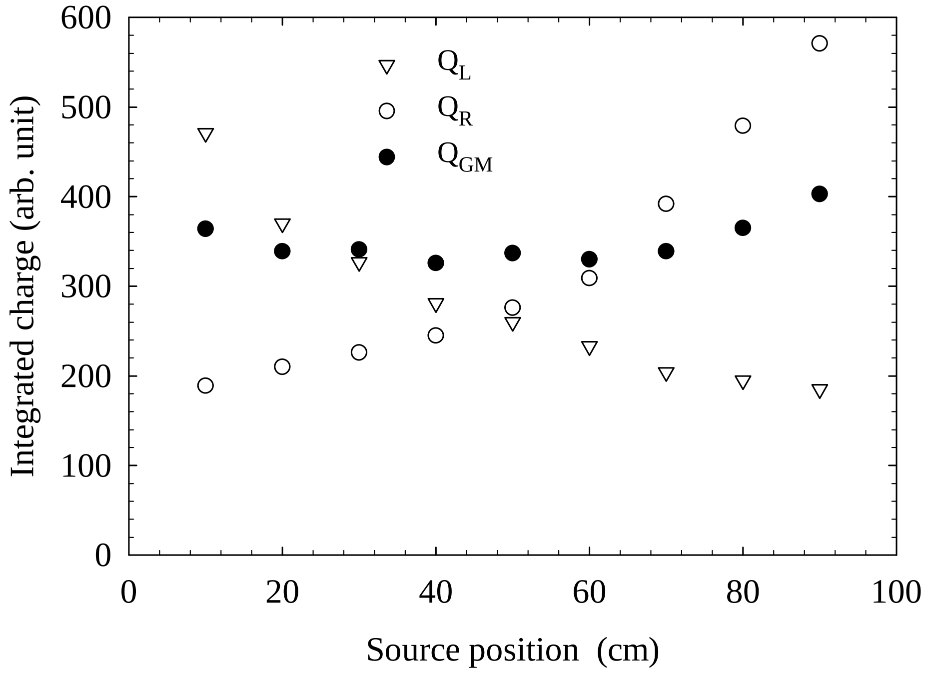

Figure 2.8: Variation of Q_L, Q_R and Q_{GM} (see text) as a function of distance from one end.

^{22}Na was detected in a plastic bar in coincidence with the complementary 511 keV γ-ray detected in a 8 cm thick BaF_2 detector with a hexagonal cross section and having a face to face distance of 6 cm. Both T_L and T_R, measured with respect to BaF_2, were recorded. The TOF and position information were extracted using the expressions given earlier. The TOF spectrum obtained is shown in Fig. 2.5. The full width at half maximum (FWHM) is $\sim$ 1.4 ns, which includes the contribution from the electronics as well as the transit time spread of PMTs. Fig. 2.6 shows the position spectrum derived from T_L and T_R. The position resolution is $\sim$ 20 cm and the response is linear as shown in Fig. 2.7. For a given amount of energy deposition the integrated charge from a PMT varies by a factor of $\sim$3 from one

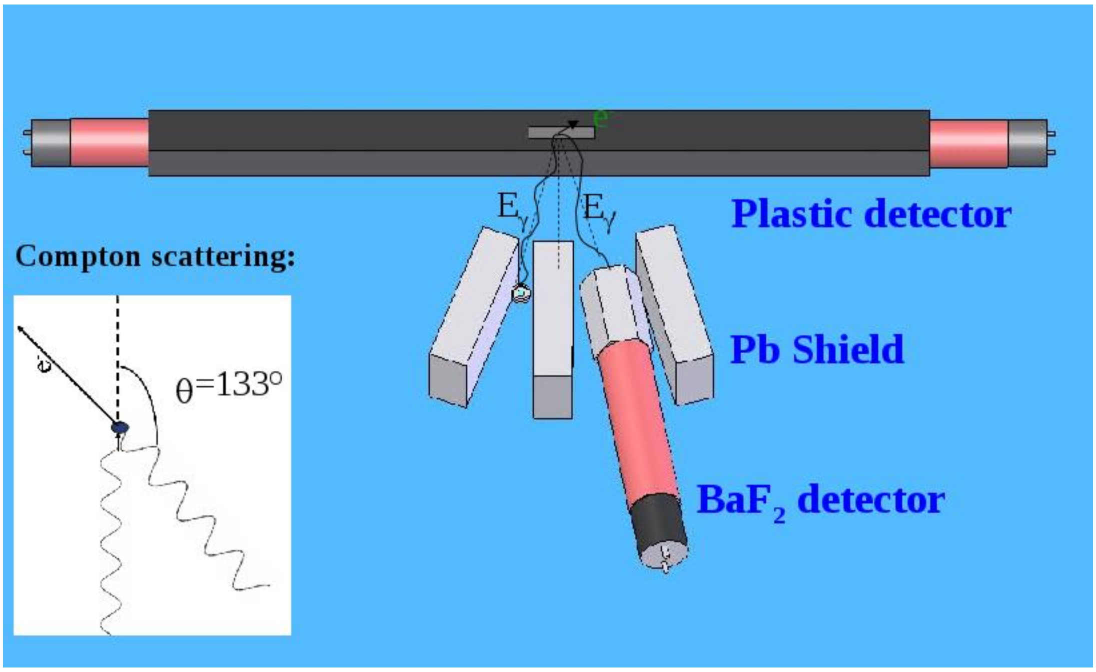

Figure 2.9: A schematic setup for the measurement of energy response of the plastic scintillator for electrons.

end to other as shown in Fig. 2.8. The geometric mean Q_{GM} is almost independent of position, within 5%, except at the ends where it increases up to $\sim$ 15%.

The energy resolution for mono-energetic electrons produced within the plastic scintillator was measured using the response to a recoiling electron in the Compton scattering of γ-rays. The back scattered photon was detected in a BaF_2 detector for tagging on the energy of the electron. γ-rays from radioactive sources ^{137}Cs, ^{60}Co and ^{241}Am-Be were collimated using appropriately placed lead bricks to illuminate a 2 cm wide portion of the plastic scintillator. A schematic setup for this measurement is shown in Fig. 2.9. The source and collimator assembly was moved along the length of the plastic to measure the position dependence of the response. The measured energy spectra of the electrons for the central source position are shown in Fig. 2.10. The energy response is linear as shown in Fig. 2.11. The

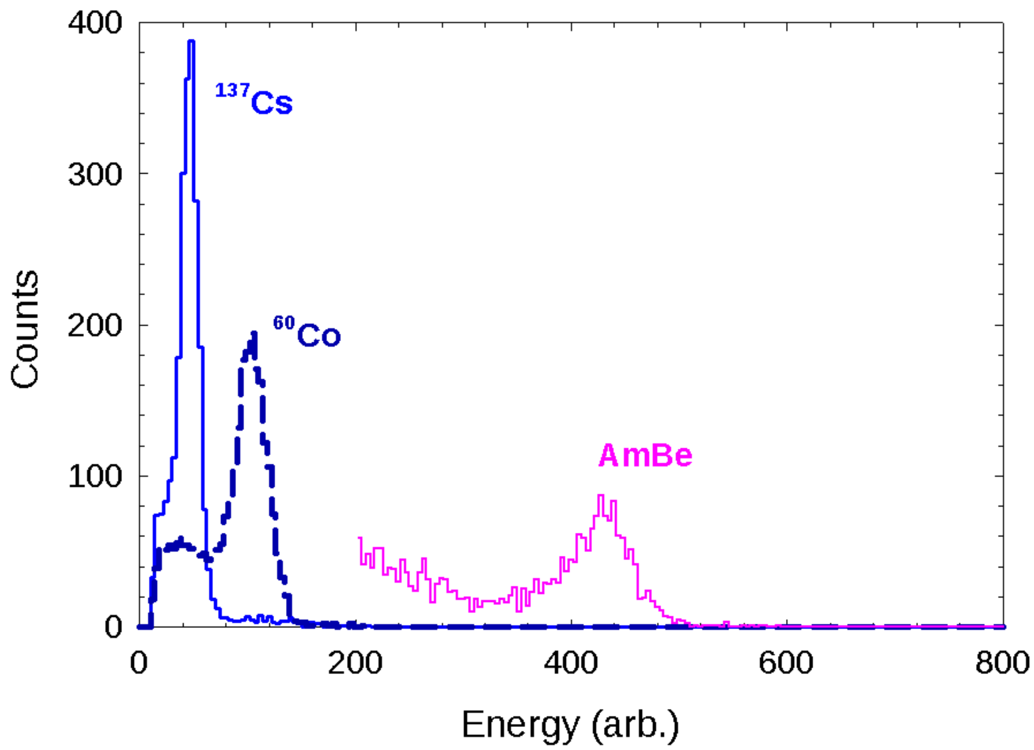

Figure 2.10: Energy spectra measured in the plastic scintillator for ∼450 keV, 1 MeV and 4.15 MeV electrons using various radioactive sources illuminating the central position.

$\triangle E_{FWHM}/E$ was measured to be $\sim$ 35% and $\sim$ 12% for 450 keV and 4.15 MeV electrons, respectively, produced at the centre of the plastic scintillator. This was almost independent of the position in the plastic. The finite size of the BaF_2 detector and the illuminated zone in the plastic had an insignificant contribution to the measured energy resolution.

Response to monoenergetic neutrons

Monoenergetic neutrons were produced by bombarding a $\sim$ 2 mg/cm^2 thick ^{nat}Li metal target with proton beams of energies 6.3, 8, 12, 16 and 19 MeV from the

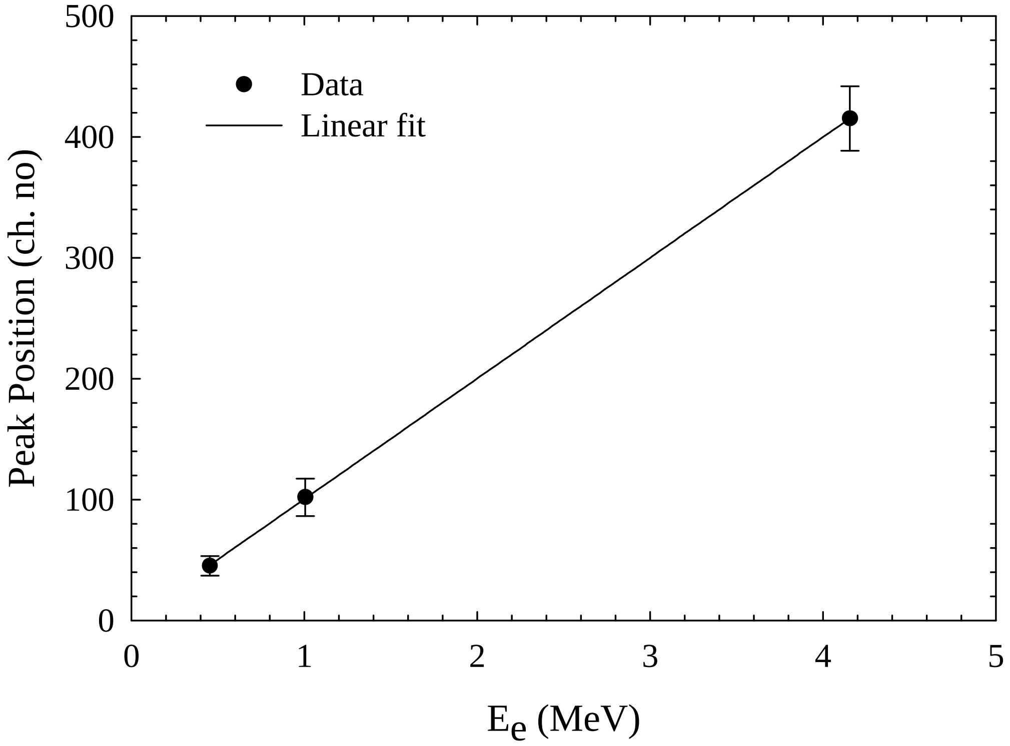

Figure 2.11: Electron energy response of the plastic scintillator. The vertical error bars depict the FWHM of the peaks shown in Fig. 2.10

Mumbai Pelletron. The neutrons produced in the reaction ^{7}Li(p,n$_1$)^{7}Be* were detected by one of the plastic scintillators in coincidence with the 429 keV γ-ray emitted from the first excited state of ^{7}Be. The γ-ray was measured in the BaF$_2$ detector, mentioned earlier, placed at $\sim$ 2 cm from the target. The plastic scintillator detector was placed at a distance of 3 m from the target and at 45° with respect to the beam direction. The TOF of the events in the plastic scintillator was measured with respect to the BaF$_2$ detector using time to amplitude converters (TAC) calibrated using a high precision time calibrator. The measured TOF

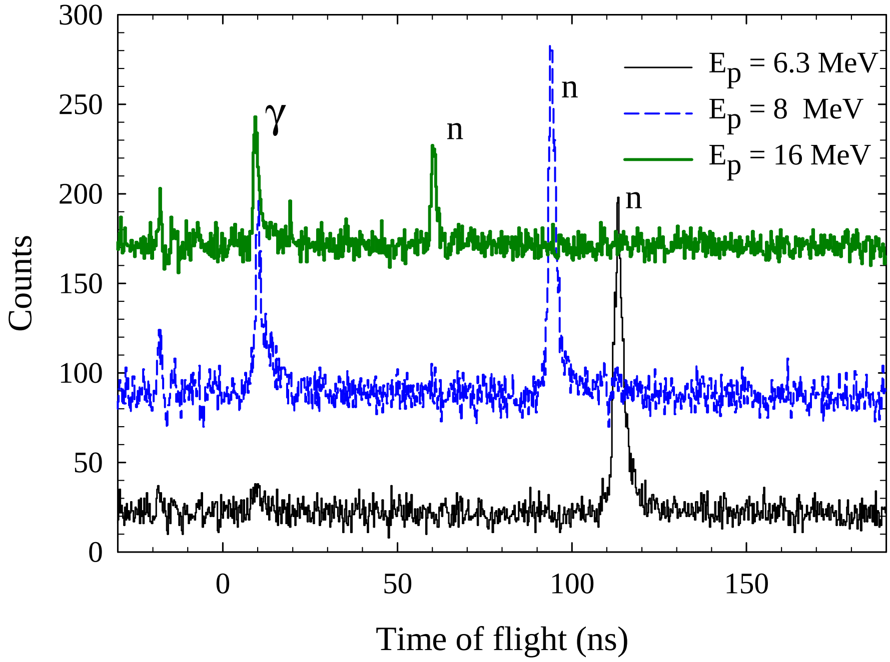

Figure 2.12: TOF spectra from p + ^{nat}Li reaction at $E_p = 6.3$, 8 and 16 MeV. The position of the gamma and neutron peaks are indicated.

spectra for the neutron group populating directly the 0.429 MeV excited state in ^{7}Be are shown in Figs. 2.12 and 2.13. The peaks in the TOF spectra correspond to neutrons of energies 3.7, 5.3, 9.0, 12.7, 15.4 MeV, respectively. The relative time differences between the neutrons and γ-ray peaks decrease with increase in neutron energy and agree with the expected values within 2%.

In order to assess the attenuation of neutron and γ-rays by the lead shield a measurement was made at E_p=6.3 MeV. In the same measurement the contribution of scattered neutrons were assessed by placing the MS shield near the target. The TOF spectra are shown in Fig. 2.14. A comparison of the spectra shows that the lead shield attenuates the neutron group by $\sim$ 10% and the γ-rays by $\sim$70%.

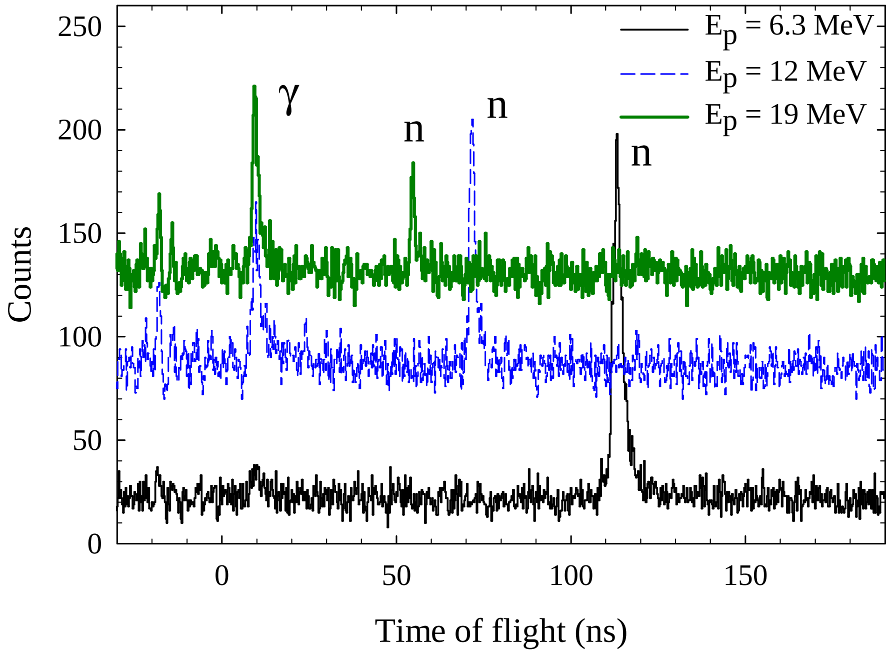

Figure 2.13: Same as in Fig. 2.12 for E_p = 6.3, 12.0 and 19 MeV.

Moreover, the contribution from the scattered neutrons is negligible (with an upper limit of 5%).

2.3.3 Efficiency measurement for monoenergetic neutrons

The efficiency of plastic detector for monoenergetic neutrons was measured using the same reaction. The proton beam energies were 10 and 16 MeV corresponding to neutron energies of 7.1 and 12.7 MeV, respectively. One plastic bar was used to measure neutrons in coincidence with 429 keV γ-rays detected in an array of seven close-packed hexagonal BaF_2 detectors of dimensions mentioned earlier. The plastic detector was placed at 45° with respect to the beam and at 1.5 m from the

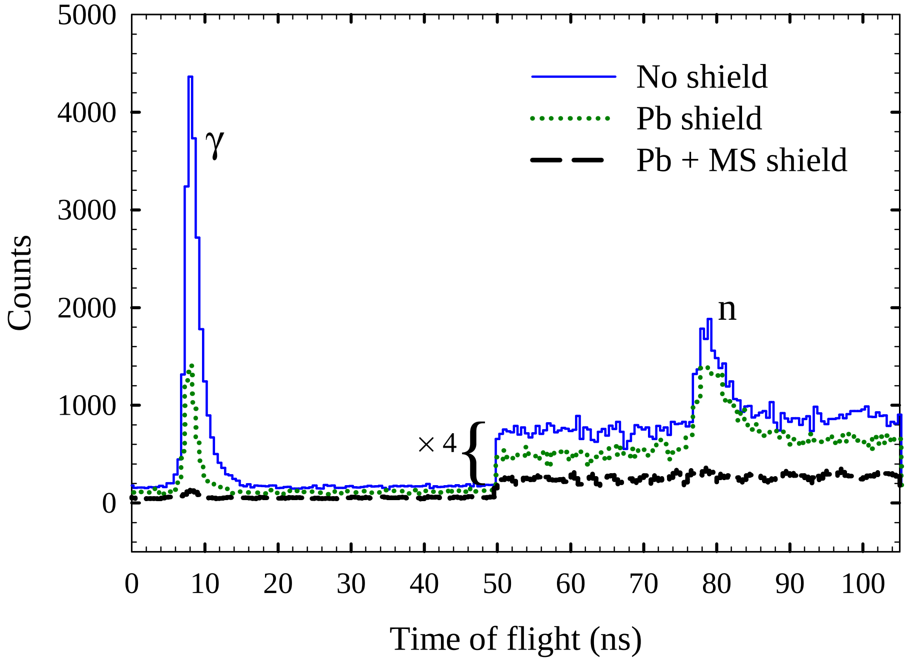

Figure 2.14: TOF spectra with and without lead and MS shields for a plastic scintillator.

target. The BaF_2 array was placed at $\sim$ 2 cm from the target. The anode signal from PMT of each BaF_2 detector was amplified and split to measure energy and pileup. The split signals were fed to two charge sensitive analog to digital converters (QDC) with gate widths of 2 μs and 200 ns. The dynode signals from both left and right PMTs of the plastic scintillator were amplified for pulse height measurement and the anode signals were processed to measure TOF with respect to the logical OR of BaF_2 timing signals. The energy calibrations of plastic and BaF_2 detectors were done using ^{137}Cs and ^{60}Co γ-ray sources. The measured energy spectrum for 429 keV γ-rays in a BaF_2 detector is shown in Fig. 2.15. The energy spectrum of the plastic detector for a given neutron energy was obtained by gating on the

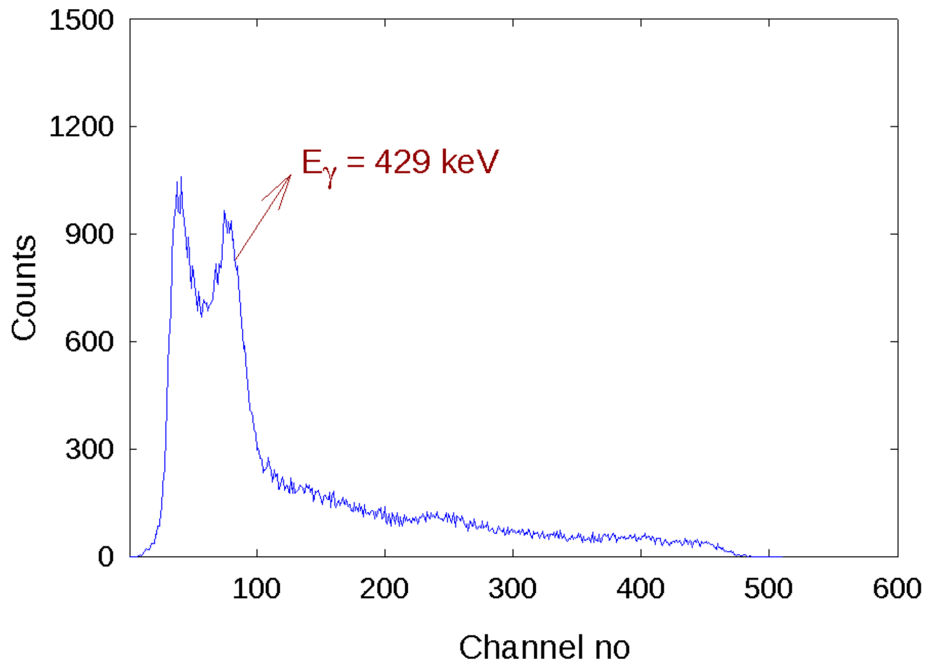

Figure 2.15: 429 keV γ-rays measured in a BaF_2 detector

corresponding peak in the TOF spectrum. Fig. 2.16 shows the energy spectrum of the plastic scintillator without random subtraction for 7.1 MeV neutron. The random contribution subtracted energy spectra are shown in Fig. 2.17. Here the energy corresponds to the electron equivalent energy (E_{ee}) of the charged particles produced by neutron interaction in the scintillator.

The efficiencies of the plastic scintillator for the two neutron energy groups mentioned above were estimated as follows. In the data analysis the number (M) of BaF_2 detectors detecting the 429 keV γ-ray in coincidence was generated event by event. The events with M >1 obviously correspond to random events. The yield of the n_1 group at each proton energy was obtained from the TOF spectra for the condition of M = 1 and E_{ee} $\geq$250 keV. The neutron detection efficiencies were obtained from these yields, the target thickness and the angle dependent cross

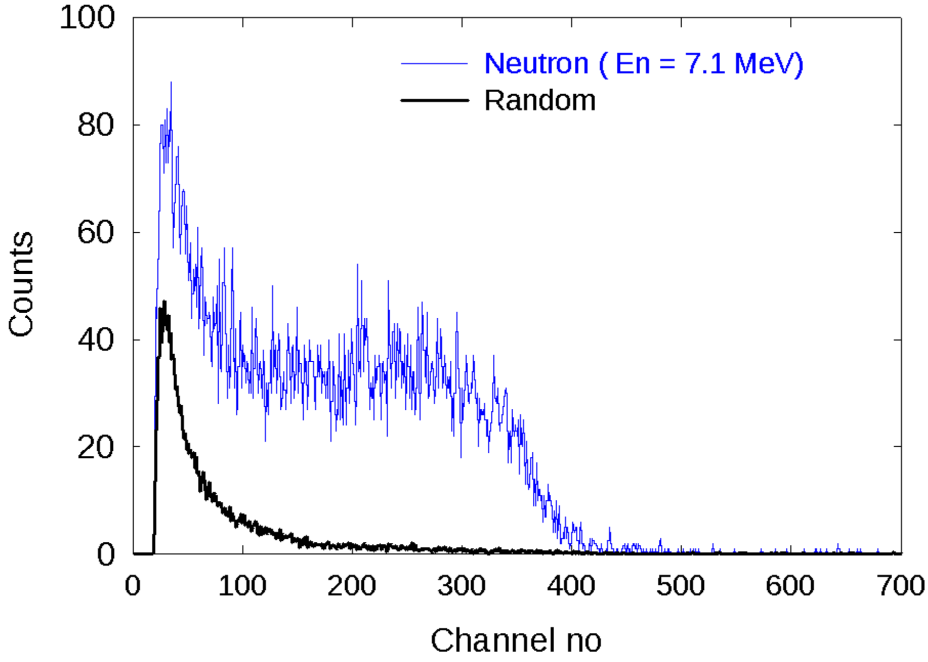

Figure 2.16: Geometric mean of deposited energy at E_p=10 MeV for suitable gate on TOF for neutron and random events

section of the n_1 group. This cross section was taken from Poppe *et al.* [47]. The target thickness was obtained from the singles γ-yield in all seven BaF_2 detectors measured at 16 MeV proton energy. The efficiency of the BaF_2 array for 429 keV γ-rays was calculated as 26.7 % using the Electron Gamma Shower (EGS) simulation program [48]. The target thickness extracted using the angle integrated cross section from Ref.[47] was 2.8 $\pm$ 0.3 mg/cm^2. The neutron detection efficiencies estimated from the above procedure were divided by the geometrical efficiency of the detector to get the intrinsic efficiencies. These are shown in Table 2.3. These measured efficiencies, however, include the contributions of the scattered neutrons from the BaF_2 array. This effect was estimated to be $<$ 7% from the Monte Carlo simulation discussed in the next section.

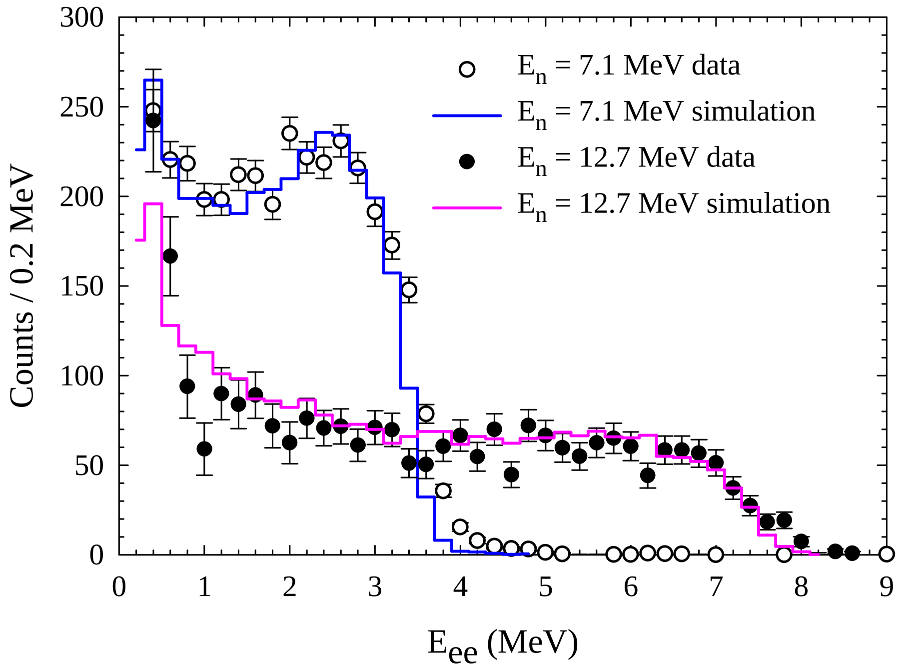

Figure 2.17: Experimental and simulated energy (electron equivalent) response of the plastic scintillator to neutrons of energies 7.1 and 12.7 MeV.

2.3.4 Monte Carlo simulation of the neutron detector array

The simulation of the response of the plastic detector array to fast neutrons has been performed by a Monte Carlo program developed in our laboratory. The processes by which neutrons of energy up to $\sim$ 20 MeV interact with the detector material were taken as (a) elastic scattering on hydrogen and ^{12}C, (b) inelastic scattering to the 4.4 and 7.6 MeV states in ^{12}C and (c) ^{12}C(n,α), ^{12}C(n,p) reactions. Among these the first process is the dominant one. The cross sections were taken from Ref. [49].

In the program, neutrons of a given energy are made incident on the plastic

Table 2.3: Measured and simulated intrinsic efficiency of plastic scintillator detector for mono-energetic neutrons in the absence (A) and presence (B) of the BaF_2 array.

E_n(MeV)	Measured efficiency (%)	Simulated efficiency(%) (A)	Simulated efficiency(%) (B)
7.1	27.4 ± 2.8	26.4	27.2
12.7	22.7 ± 3.2	20.8	22.3

array, placed at a certain distance from the source, assuming angular isotropy. The energy dependent total interaction cross section determines whether the neutron scores a hit in the detector. If it scores a hit, the interaction process is chosen randomly on the basis of the relative magnitude of the respective cross section. If the process is elastic scattering on hydrogen, the scattering angle in the centre of mass (c.m.) system is chosen randomly. This decides the energy of the recoiling proton which is assumed to be fully deposited in the detector. In (n,p), (n,α) and (n,n$'$)3α processes, the energy of p and α were calculated assuming isotropic emission in the c.m. system. For the (n,n$'\gamma$) process, the 4.4 MeV γ-ray deposits energy depending on the attenuation length and the available path in the scintillator for a given propagation direction. The electron energy equivalent (E_{ee}) of the deposited energy for heavy charged particles are obtained using the following empirical expression

$$T_e = a_1 T_p - a_2\big[1.0 - exp(-a_3 {T_p}^{a_4})\big]. \tag{2.6}$$

The choice of the parameters a_1 to a_4 was guided by those given by Cecil *et al.* [49] with some fine tuning for proton. These are presented in Table 2.4. The light output due to recoiling ^{12}C nuclei is small and therefore neglected. The time of

Table 2.4: Parameters in the light response function for proton and alpha.

	Present work				Cecil et al.			
Particles	a_1	a_2	a_3	a_4	a_1	a_2	a_3	a_4
Proton	0.97	7.6	0.1	0.90	0.95	8.0	0.1	0.90
Alpha	0.41	5.9	0.065	1.01	0.41	5.9	0.065	1.01

occurrence of the PMT signal was derived from the neutron flight times and the scintillation photon propagation time. The simulated left and right PMT times (T_L, T_R) and E_{ee} from each event were used to generate TOF and E_{ee} spectra provided E_{ee} is greater than the experimental threshold. The TOF spectrum for a given neutron energy shows a peak with a width arising from the intrinsic time resolution of the plastic scintillator as well as the variation in the interaction position. The shapes of the simulated E_{ee} spectra at neutron energies of 7.1 and 12.7 MeV compare well with the experiment as shown in Fig. 2.17.

The ratio of detected events to the number of incident neutrons gives the intrinsic neutron efficiency. The simulated intrinsic efficiencies of one plastic scintillator for neutrons of energies 7.1 and 12.7 MeV were obtained for the experimental threshold (E_{ee}) of 250 keV. These are shown in the third column of Table 2.3. The energy dependent neutron efficiencies for various thresholds are shown in Fig. 2.18 for a single plastic scintillator with the lead shield in front. It can be seen that while an increase in E_{ee} does not substantially change the neutron detection efficiency at higher energies, it increases the effective threshold energy for neutron detection.

The presence of the BaF_2 array near the target provides material against which neutrons can scatter, some of which reach the plastic detector. In order to estimate their contribution to the measured efficiencies, the simulation program was

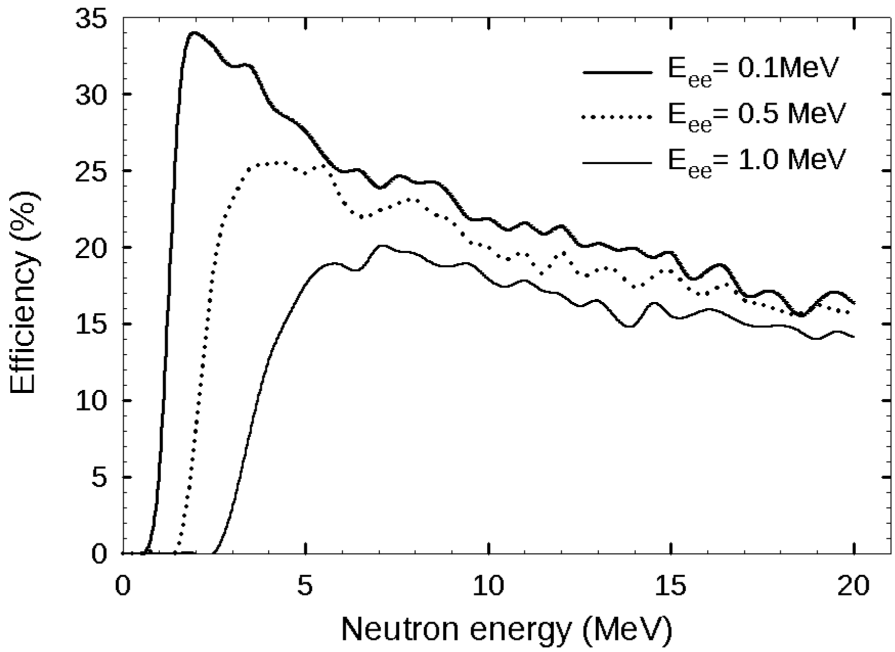

Figure 2.18: Simulated neutron efficiency of a plastic bar for different energy thresholds E_{ee}.

extended to include the elastic and non-elastic processes from Ba and F in BaF_2. The increase in the TOF of the elastically scattered neutrons is too small to distinguish them from those directly reaching the plastic. The non-elastic processes lead either to a loss of neutrons as in the (n,p), (n,α), (n,γ) reactions or to lower energy neutrons from the (n,n$'$) and (n,2n) reactions. These processes, therefore, do not contribute to the counts in the TOF peak. The intrinsic efficiencies in the presence of BaF_2 are renormalised by the extra contribution in the TOF peak essentially due to elastic scattering. These are shown in the last column of Table 2.3. The renormalised efficiencies are increased up to about 7%. These are however the upper limits because we have assumed isotropy in the scattering processes whereas the limited elastic scattering data shows forward peaked distribution (see for example Ref. [50]). It may be mentioned that the elastic scattering process on BaF_2

does not lead to any significant change in energy spectrum shown in Fig. 2.17.

2.4 CsI(Tl) Detector Array for Charged particles

CsI(Tl) scintillation crystals have been used for the detection of both γ- rays and charged particles. This scintillator has higher density and higher atomic number than NaI, therefore its efficiency for gamma detection is higher. The light-conversion efficiency of CsI(Tl) is about 45% of that for NaI(Tl). The emission spectrum of CsI(Tl) extends from 420 to 600 nm. There is a little overlap between the CsI(Tl) scintillation emission spectrum and the spectral sensitivity of photo multipliers, which prevents its widespread use with PMTs. However, the development of low capacitance, large area silicon photodiodes with high quantum efficiency matches the emission spectrum of CsI(Tl). The CsI(Tl) scintlators are widely used with Si-PIN photodiode as the readouts. The detector is used for charged particle detection making use of its property of pulse shape discrimination [39].

2.4.1 Description of CsI(Tl) detector array

An array of eight CsI(Tl) scintillators, each coupled to a Si(PIN) photodiode was assembled to detect the charged particles in the heavy ion induced reaction using the Mumbai PLF. Since the size of the photodiode is small a compact closed packed configuration can be made. The detectors were grouped in to two arrays, each consisting of four detectors and mounted in aluminum frames as shown in Fig. 2.19. The CsI(Tl) scintillators coupled to Si(PIN) photodiode have been procured from M/s SCIONIX, Holland. The active area of the CsI(Tl) is 25×25 mm^2 and the

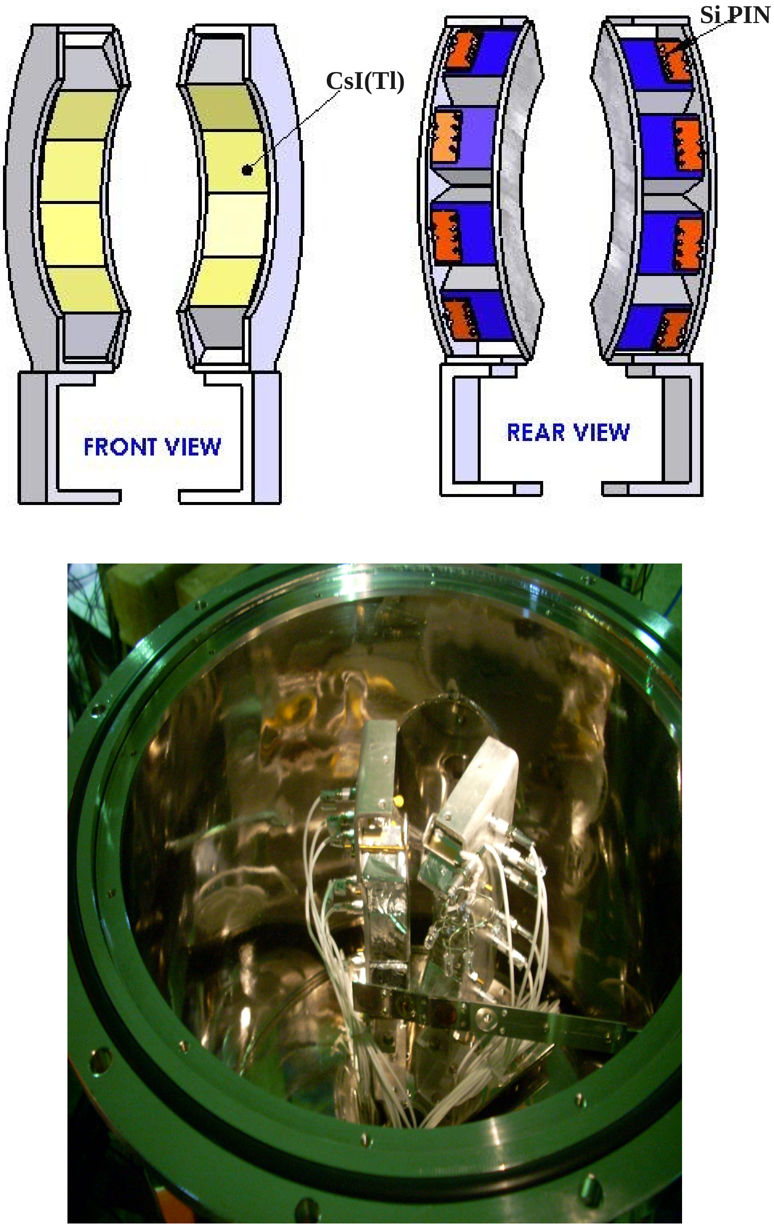

Figure 2.19: At the top is shown the schematic assembly of the CsI(Tl) detectors mounted in the frames and the bottom figure is the photograph of the CsI detector array mounted in the aluminum frame and placed in a multi-purpose, mini scattering chamber.

thickness is 10 mm. The coupling of Si-PIN photodiodes (Hamamatsu S3204-08) to the scintillators was done (by Scionix) using a perspex light guide of dimension 25×25×15 mm^3. The sensitive area of the photodiode is 18×18 mm^2. Some of its important features are good energy resolution, good stability, fast response, low capacitance and high quantum efficiency (85% at peak wavelength 540 nm). The signal readout was taken through a high gain (∼9 V/pC) charge sensitive preamplifier mounted close to the Si-PIN photodiode for further processing. The preamplifier is vacuum compatible and has low power dissipation (∼100 mW). The dc offset in the preamplifier signal output was eliminated by using a capacitor (∼6 μF) and a battery was used to supply 12 V to preamplifier in order to reduce the pick-up problem and, thus, to improve the signal to noise ratio. The preamplifier signals were amplified and split for the measurement of energy and PSD. The typical energy resolution of these detectors is about 6% at ∼5 MeV for alpha particles.

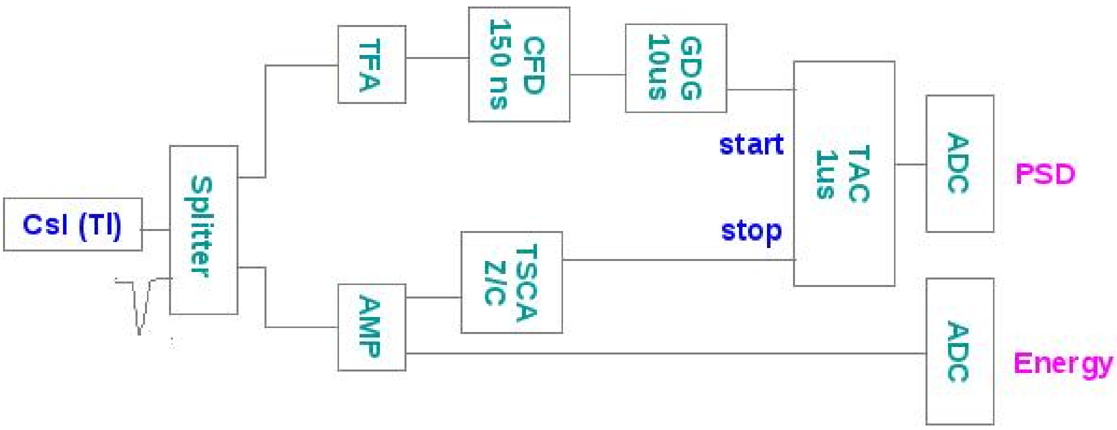

Figure 2.20: Circuit diagram of zero cross over technique for particle identification.

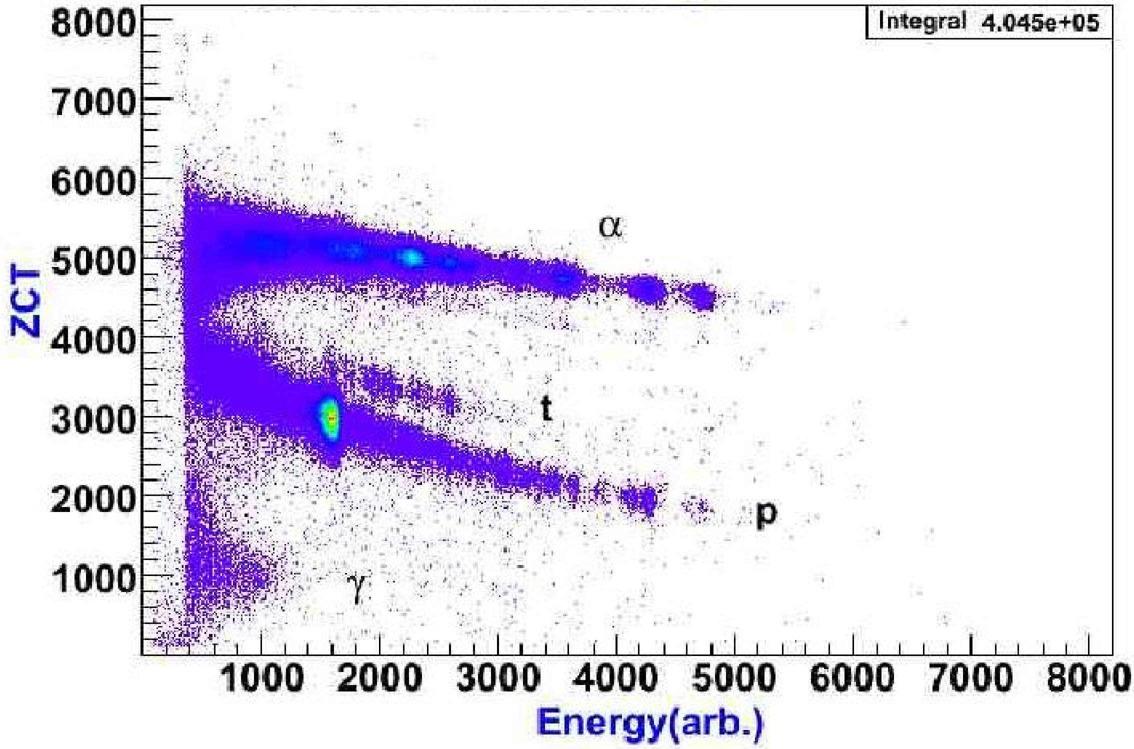

Figure 2.21: A 2D plot between the energy deposited and ZCT in $^{12}C+^{12}C$ reaction at $E(^{12}C) = 30$ MeV.

2.4.2 Pulse Shape Discrimination

The scintillation light of the CsI(Tl) detector is composed of a slow and a fast component. The amplitude ratio of these components as well as the decay time constant of the fast component vary with the type of radiation interacting with the crystal. These properties of CsI(Tl) can be used to identify the particle that caused the scintillation. Many techniques such as the charge comparison [52], zero cross over time (ZCT) [53] and ballistic deficit [54] are used for the charged particles identification. In the charge comparison method, the ratio of integrated charge of linear signal for a short time($\sim$ 200ns) to long time ($\sim 2\mu$s) window provides the identification of charged particles. The amplitude degradation at the output of a pulse shaping circuit due to the finite rise time of the input pulse is used for the particle identification in the ballistic deficit method. The ZCT

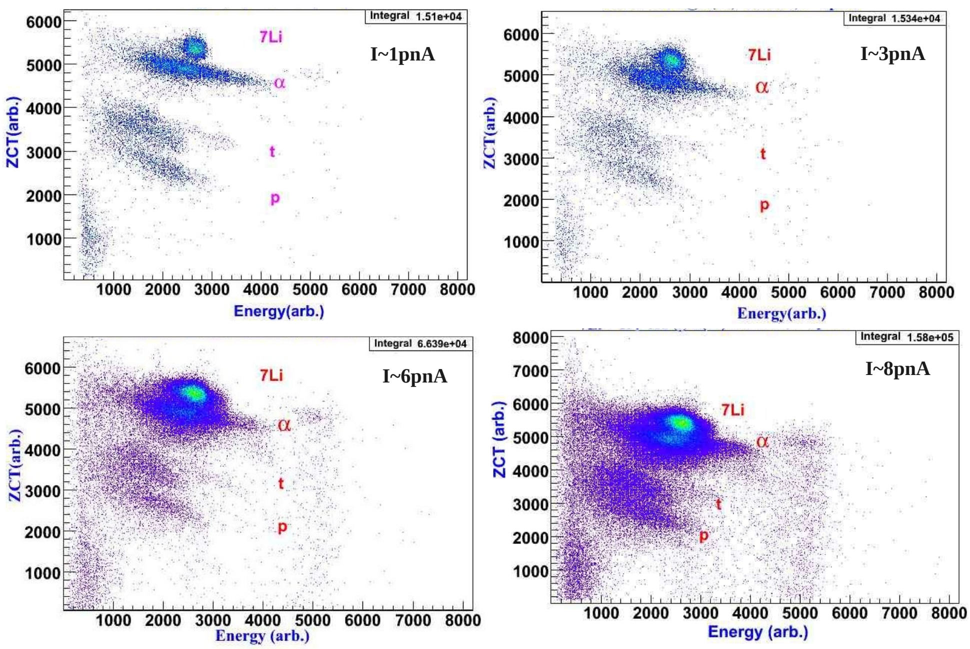

Figure 2.22: Count rate effect on the PSD of CsI(Tl) detector in ^{7}Li+^{197}Au reaction at 30 MeV.

method is based on passing the signal through a shaping amplifier to produce the bipolar shape. The time at which the bipolar pulse crosses zero does not depend on pulse amplitude but depends on the pulse shape and rise time. The time interval between the beginning of the pulse and zero cross over point depends on the type of particle interacting with the CsI(Tl) detector. The block diagram used for particle identification by the ZCT method is shown in Fig. 2.20. The performance of the detector for particle identification and the count rate effect for the PSD has been studied in an in-beam experiment in ^{7}Li+^{197}Au reaction at beam energy 30 MeV.

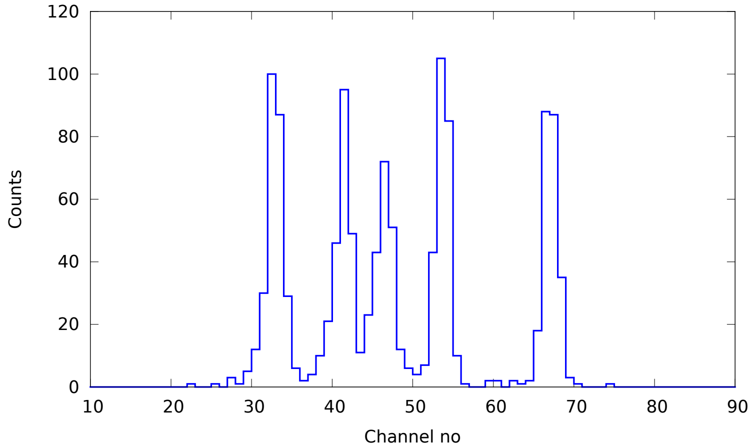

Figure 2.23: Alpha energy spectrum in a CsI(Tl) detector using ^{229}Th source. The alpha peaks with energies 4.845, 5.830, 6.341, 7.067, 8.376 MeV are used for the calibration of the detector up to 8.4 MeV.

The ZCT technique was used to identify the particles produced in the reaction. The electronic block diagram used in this reaction is similar to that in Fig. 2.20. Two six-channel modules for sensing the zero crossing of a bipolar pulse have been developed in-house for use with the CsI(Tl) detector array. These modules were used for the charged particle identification in ^{7}Li+^{197}Au reaction and the study of CsI(Tl) detector response to alpha particles in ^{12}C+^{12}C reaction. Fig. 2.21 is a two-dimensional (2D) plot between the energy and ZCT in ^{12}C+^{12}C reaction which shows clear discrimination of various particles. It was also observed that the PSD of CsI(Tl) detector using the laboratory made ZCT module was similar to that with the commercial one. It is important to study the PSD of CsI(Tl) detector in ^{7}Li induced reaction of heavy nuclei and the count rate effect on the PSD. The experiment was carried out to study the count rate effect on the PSD in ^{7}Li+^{197}Au reaction at 30 MeV by varying the incident beam current from 1-8 pnA. Typical 2D spectra characterizing the PSD of CsI(Tl) detector for various beam current are shown in Fig. 2.22. It is clear that the discrimination of particles, mainly alpha and ^{7}Li, is very good at low current while the PSD deteriorates at high current. The PSD by ZCT technique was found to be limited at high rates due to the pile up of pulses. The count rate of the CsI(Tl) was therefore be restricted to $\leq$3 kHz for good discrimination of particles using PSD technique.

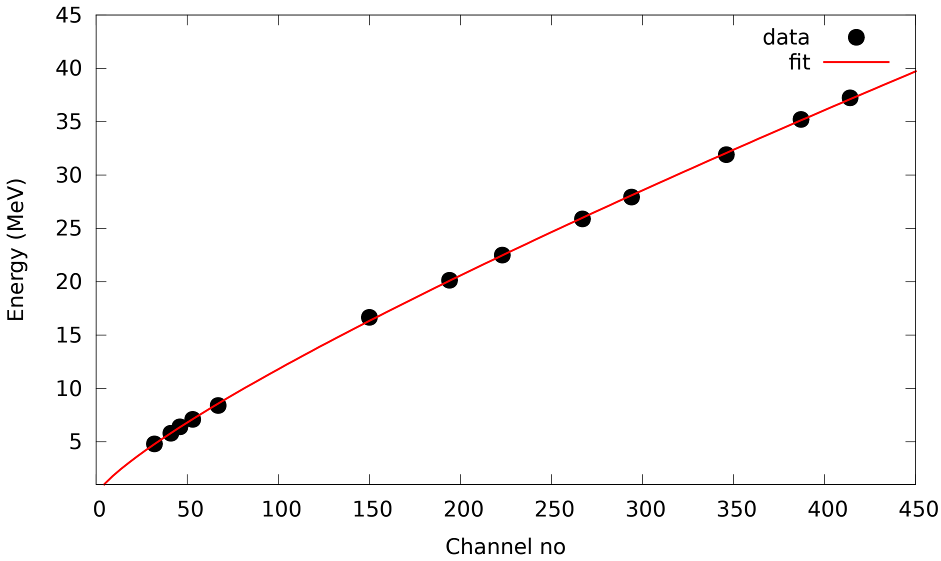

Figure 2.24: Calibration of a CsI(Tl) detector for alpha particles using Th source and ^{12}C(^{12}C, α)^{20}Ne reaction.

2.4.3 Response of CsI(Tl)detector to α-particles

The amount of light produced by a CsI(T1) scintillators depends on the energy, charge and mass of the particle interacting with the scintillator. The light output of the scintillator is related to the stopping power (energy loss per unit length) of the particle in the crystal and is described by Birks empirical relation. It is a non-linear function of the energy of the alpha particles. Thus, in order to use these detectors for the alpha spectroscopy, it is necessary to measure the light output over a wide energy range for alpha particles. The non-linearity of the light output of CsI(Tl) detector in the energy region from $\sim$5 to 40 MeV has been measured for α-particles. The measured alpha response from $\sim$5 to 8 MeV using Th source is shown in Fig. 2.23. The response at higher energies was measured with alpha particles from ^{12}C(^{12}C, α)^{20}Ne reaction populating discrete states in ^{20}Ne.

The experiment was carried out to measure alpha particles in (^{12}C, α) reaction at 24, 30 and 40 MeV ^{12}C beam using the Mumbai PLF . The carbon target backed by 1 mil thick Ta foils was mounted 9.5 cm upstream of the centre of the reaction chamber and the detectors were placed at 4.5 cm from the centre. The detectors were brought to 0° to reduce the kinematic energy spread and alpha particles were detected by the ZCT technique similar to Fig. 2.22. The projected alpha energy spectra were corrected for the energy loss in the Ta foil using the energy loss of alpha particles in Ta calculated using SRIM [55]. The measured energy calibration for alpha particles is shown in Fig. 2.24. It can be seen from the figure that the calibration is not linear over the full energy range and can be fit to a function having a linear term and a power function of light output [56]. This measured non-linearity in energy of alpha particles has been used for calibrating the CsI(Tl) detectors in the neutron alpha coincidence experiment.

3

Measurements and Data Analysis

3.1 Pelletron Linac Facility

The Mumbai Pelletron Linac facility (PLF) has a Pelletron tandem accelerator procured from NEC, USA [57] and an indigenously developed superconducting linear accelerator(LINAC) [58, 59] based on lead plated copper quarter wave resonators. The schematic layout of the Mumbai PLF is shown in Fig. 3.1. Since the commissioning, these accelerators have been used for the basic research in the fields of nuclear, atomic and condensed matter physics as well as accelerator based applications. The main purpose of the LINAC is to boost the energy of the heavy ion beams so that the scope of research in nuclear physics can be extended to heavier projectile which are unexplored by the Pelletron energy. Some technical specifications of these accelerators are given in Table 3.1.

The source for the charged particles is located at the top of the accelerator tower. The ion sources used for providing the various species of beam are: (a) direct extraction duo-plasmatron (DEDP), (b) rf source with Rb exchange canal

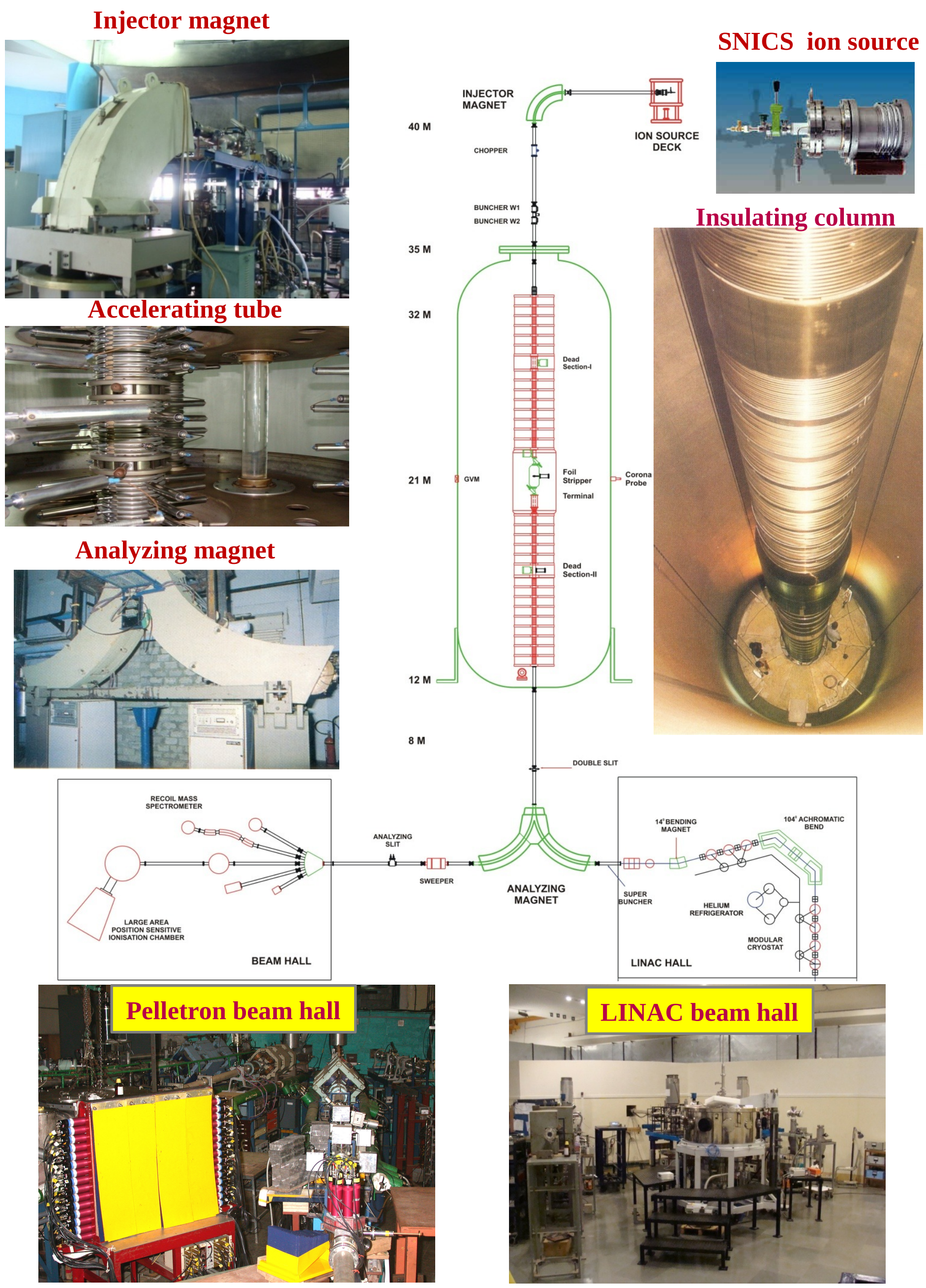

Figure 3.1: A schematic layout of Mumbai Pelletron Linac Facity

Table 3.1: Specifications of the Pelletron and LINAC

Pelletron		LINAC	
Accelerating tube voltage rating	14 MV	Resonators	28 nos
		Modules	7 nos
Voltage stability	±2 keV	Energy gain	14 MV/n
Proton energy range	up to 28 MeV	Heavy ions	up to A 80
Heavy ion energy range	up to 14(n+1) MeV	Energy range	5-12 MeV/n

(Alphatross) and (c) source of negative ions with Cs sputtering (SNICS). A Cesium sputter ion source (SNICS) generates negative ions, which are initially accelerated to low energies (150-250 keV) in a short horizontal section. These low energy negative ions are then bent through 90° into the vertical accelerating column using an injector magnet. In the first stage, the acceleration results from the electrostatic attraction of the negative ions by the positively charged high voltage terminal situated at the center of the column. The high electric potential at the terminal is achieved by a continuous transfer of charge to the terminal by means of the chain of steel pellets and hence the name Pelletron accelerator. Inside the terminal the ions pass through a thin carbon foil or a small volume of a gas, where they lose electrons and acquire a high positive charge. The average charge of the ion depends upon the type of ion and the terminal voltage. The resulting positive ions now enter the second or high energy stage of acceleration where the positive voltage of the terminal acts repulsively on the positive ions. The accelerated ions can be switched to either the Pelletron experimental area or to superconducting LINAC booster using a two way 90° analyzing magnet. The analyzed beam is transported to the five experimental stations of Pelletron beam hall through a switching magnet. The energy (E) of the analyzed ions of mass A and charge state n, neglecting relativistic effects, is related to the magnetic field (B) of the

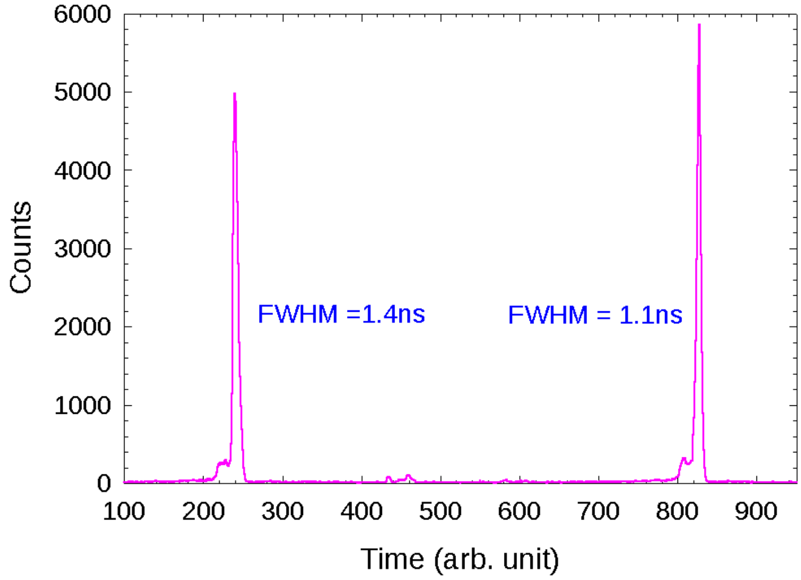

Figure 3.2: Time spectrum of pulsed beam measured with a BaF_2 detector for E_γ>2 MeV

analyzing magnet as follows:

$$B(Gauss) = 720.76\frac{\sqrt{AE(MeV)}}{n} \tag{3.1}$$

The final energy of the ion that has acquired a positive charge of n units will be $(n+1)V_T$, where V_T is the terminal voltage (maximum of 14 MV).

3.2 Pulsed Beam

A pulsed beam is obtained using an indigenously designed double harmonic buncher situated at the entrance of the Pelletron accelerator [60]. The bunchers operate at f/16^{th} and f/8^{th} sub-harmonics, where f is LINAC reference clock frequency ~150 MHz. The dark beam current between the beam bunches is swept away by a RF parallel plate sweeper, situated at the exit of the Pelletron (High

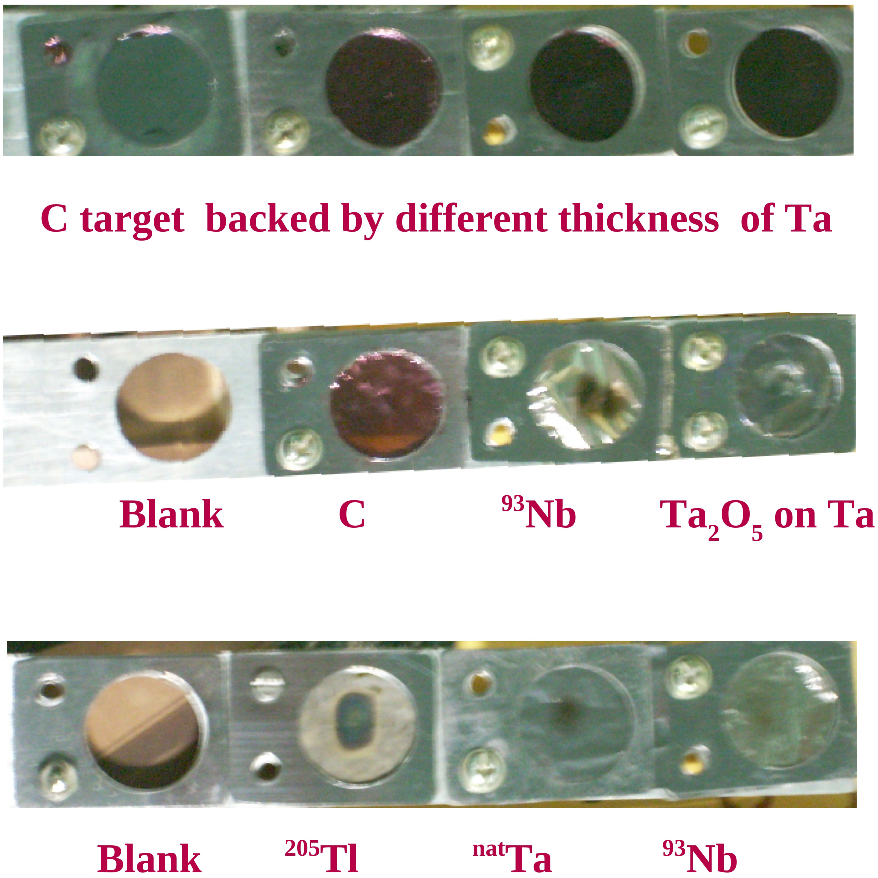

Figure 3.3: Various targets used in the experiments mounted in an Al ladder with Ta frames.

Energy section), operating at f/32 frequency. The beam bunches have a typical resolution (FWHM) of 1.5 ns with a bunching efficiency of ~66%. The beam pulsing system installed at the Pelletron is designed for heavy ions and not suitable for light ions such as proton and alpha. Since the time resolution of the pulsed beam is very important for neutron TOF measurement, a feasibility experiment was carried out to measure the resolution of pulsed ^{7}Li beam with respect to a BaF_2 detector. A typical time spectrum of pulsed ^{7}Li beam is shown in Fig. 3.2.

The measured pulse width was found to be $\sim$1.4 ns, which is adequate for the neutron TOF experiment.

3.3 Target

Various techniques such as rolling, evaporation, electro-deposition etc. are used to prepare isotopic targets for experiments. The targets used for the entire experimental program are self supported ^{12}C, ^{nat}Li, ^{93}Nb, ^{181}Ta and ^{205}Tl. In some experiments, C with Ta backing was used for alpha energy calibration purpose and Ta_2O_5 with Ta backing used as an Oxygen target for estimating the oxygen impurity in the primary targets. A typical view of various targets mounted on an Al ladder during one of the measurements is shown in Fig. 3.3.

3.4 Scattering Chamber

A compact thin wall, multi-purpose scattering chamber has been designed and fabricated to study the nuclear reactions involving measurements of charged particles in coincidence with neutrons and gamma-rays [61]. A schematic diagram along with a picture of the chamber is shown in Fig. 3.4. The chamber is made of stainless steel and has an internal diameter of 30 cm and height of 27.5 cm. The wall thickness in the central region of the chamber is 2 mm to minimize the attenuation of the neutrons or γ-rays to be detected by the corresponding detector array placed outside the chamber. The rest of the wall has a thickness of about 4 mm. The top and bottom lids have thicknesses of 10 mm. Special features of this chamber are:(a) two rotatable arms for mounting the charged particle detectors, (b) two ports (KF 40) for mounting the main targets from top and horizontal port

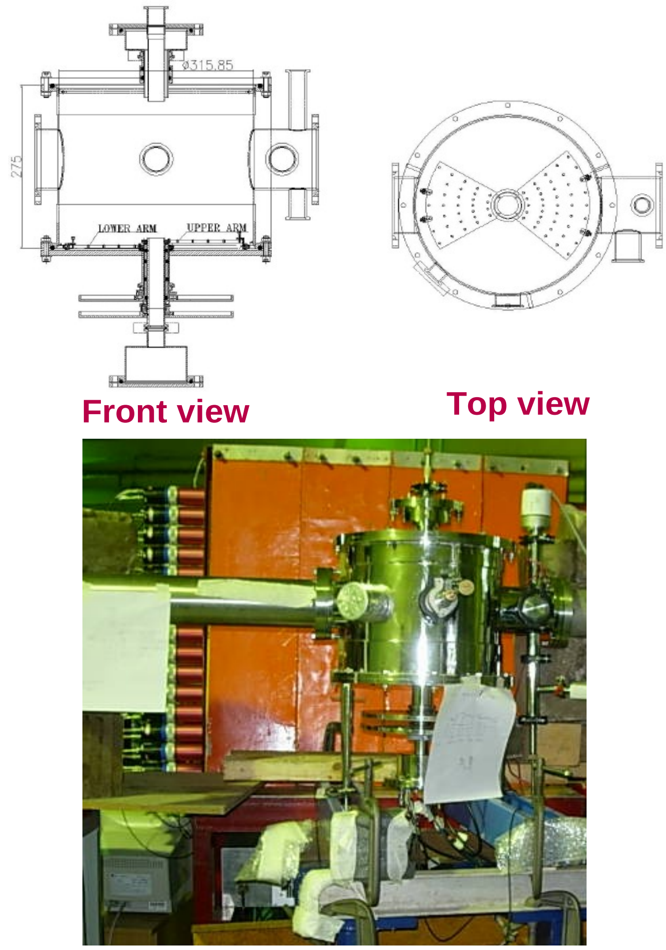

Figure 3.4: Schematic diagrams of front and top views of the scattering chamber and a picture of chamber used in the n-α coincidence experiment.

(90° with respect to beam direction), (c) a KF 25 port at the entry of the beam used for mounting off-centre targets (d) view ports with LED arrangement and ports for signal feed-through.

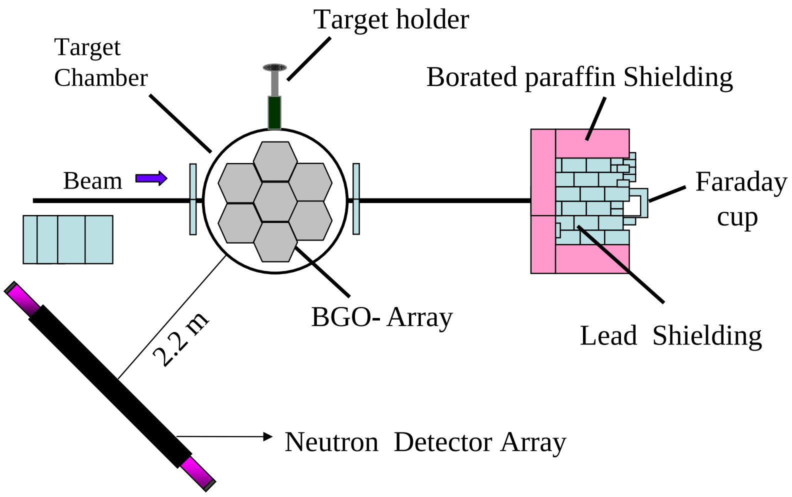

Figure 3.5: A schematic of the experimental setup used in the ^{12}C + ^{93}Nb experiment.

3.5 Data Acquisition System and Analysis Tool

A software package "Linux Advanced MultiParameter System (LAMPS)" has been developed in-house at the PLF for the data acquisition and offline data analysis [62, 63]. This package supports VME, CAMAC-FERA and a number of CAMAC controllers for data acquisition. The data acquisition system based on CAMAC crate controllers CC2000 has been developed at Electronics Division, BARC. The acquired data is buffered inside the controller and can be read out into a computer via the PCI card. Salient features of LAMPS are a user friendly graphical interface, a setup file that can be edited by a user, data compacting, writing list-mode data to hard-disk, spectrum building, pseudo-parameter building (constructing derived parameters using mathematical operations) and processing. The data can be collected either in spectra mode where the final spectra are built on-line or in the event-by-event mode where the raw data is stored in the hard disk with or without compression and off-line analysis of the data is possible using a user defined subroutine for building the derived parameters. The event trigger for data collection for various experiments generated using appropriate coincidence conditions is based on the physics requirement. Part of the data acquired in list mode using LAMPS were rewritten in ROOT compatible format and CERN ROOT package [64] used for further analysis.

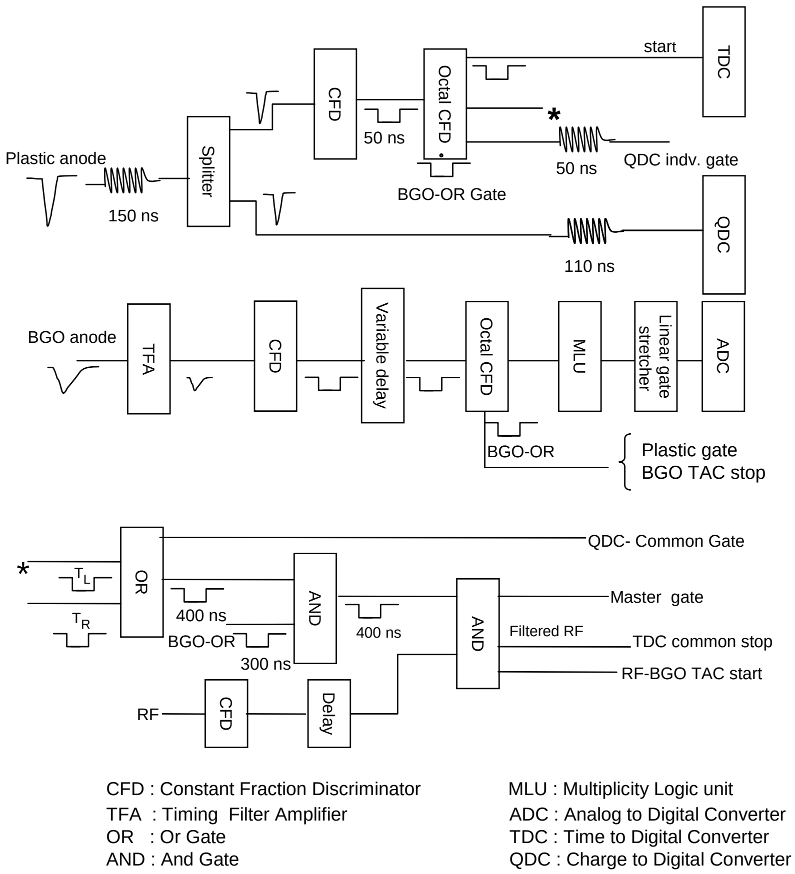

Figure 3.6: Block diagram of the electronics set up used in the ^{12}C+^{93}Nb experiment.

3.6 Angular Momentum Dependence of Nuclear Level Density

Measurements of evaporation spectra (proton, neutron and α-particles) in heavy-ion reactions have been used to study the excitation energy(E_X) and angular momentum (J) dependence of the NLD [32]. The heavy-ion reactions bring a wide range of E_X and J in the CN and offer the possibility of studying a larger variety of systems. The statistical model analysis of the measured γ-ray multiplicity gated evaporation spectra have been used to infer the angular momentum dependence of the NLD in the residual nucleus [42]. The motivation of the present measurement was to use the neutron detector array for the study of continuum neutron spectra in the ^{12}C + ^{93}Nb reaction and also to infer the angular momentum dependence of the NLD by analyzing the γ-ray multiplicity gated neutron spectra within the framework of statistical model of compound nuclear decay. A collimated, pulsed ^{12}C beam (9.4 MHz) of 40 MeV from the Mumbai PLF bombarded a self supporting ^{93}Nb target of thickness 0.5 mg/cm^2. Neutron spectra were measured by the time of flight technique with 15 plastic scintillators. The detector array was placed at 2.2 m from the target and at 135° with respect to the beam direction. It was covered with a 25 mm thick lead shield to attenuate low energy γ-rays. The beam collimators and the beam dump were shielded with lead bricks and borated paraffin blocks to reduce the gamma and neutron background. The measurements were made in coincidence with low energy γ-rays originating from the yrast transitions of the fusion residues. These γ-rays were detected in an array of 14 bismuth germanate (BGO) detectors [42]. The BGOs were shielded from the background gamma rays coming from the collimators and beam dump with suitably placed

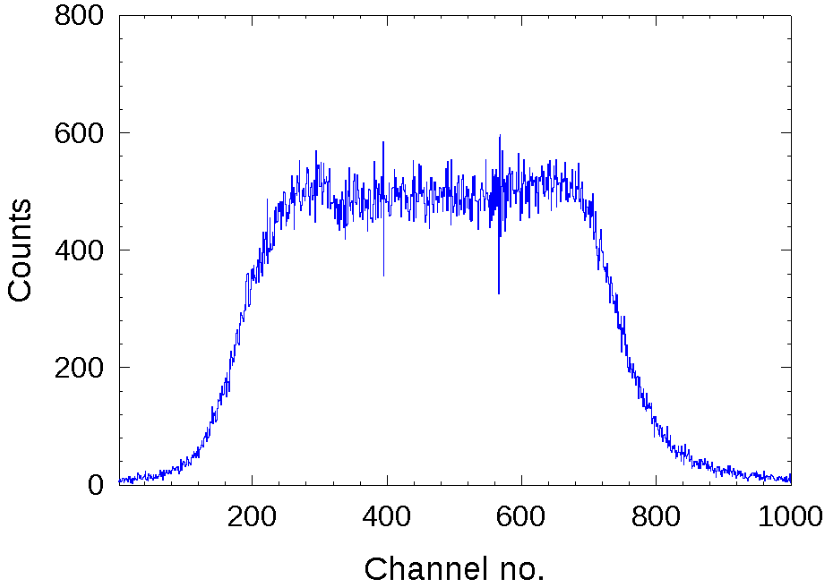

Figure 3.7: A position spectrum derived from the integrated charge collected from both sides of the plastic scintillator.

lead bricks. The schematic experimental setup is shown in Fig. 3.5. The total efficiency of BGO array for 662 keV γ-rays, measured using a ^{137}Cs source kept at the target position, was $\sim$ 65%. The schematic electronic block diagram is shown in Fig. 3.6. The high voltage applied to the PMTs of individual plastic scintillator detectors was adjusted to provide the same pulse height for 4.44 MeV γ-rays from ^{241}Am-Be source placed at the centre of the detector. The full energy range was $E_{ee} \sim$ 28 MeV. The signal from the anode was split into two parts. One was fed to a QDC for the energy measurement and the other was sent to a constant fraction discriminator (CFD) to generate the timing signal. The CFD thresholds were set at $\sim$100 keV. One of the CFD outputs was sent to the corresponding start channel of the time to digital converter (TDC) filtered through the condition that at least one of the BGO detectors fire. The second CFD output was used to generate the

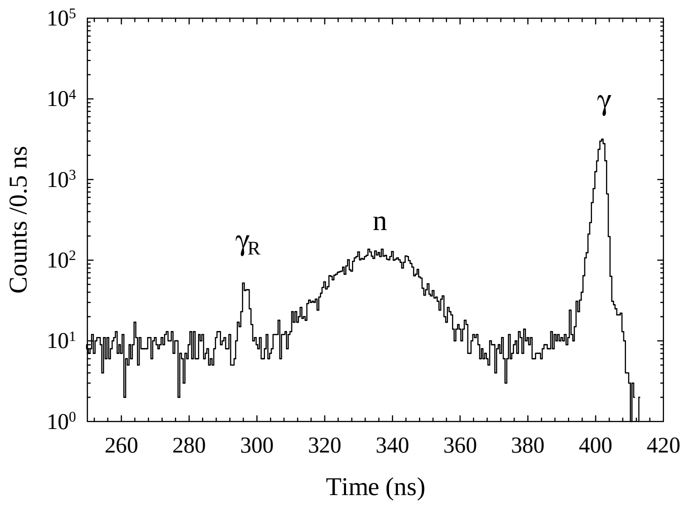

Figure 3.8: Measured TOF spectra in the reaction ^{12}C+^{93}Nb at E(^{12}C)=40 MeV for BGO fold $\geq$1. The prompt gamma peak (γ), the broad bump due to neutrons (n) and the gamma peak from the adjacent beam burst (γ_R) can be seen.

QDC gate. The third output was used to define a valid event by combining signals from all the scintillators in a logic OR unit. This OR output (Plastic-OR) was used for the common QDC gate. The timing signals from the BGO detectors were time matched and sent to a multiplicity logic unit (MLU) [51]. The time matched OR-output (BGO-OR) was used to filter the plastic CFD signals as mentioned above. A coincidence between the BGO-OR and the Plastic-OR was used to filter the RF signal derived from the beam pulsing system. The filtered RF was used as the common stop for all the TDC channels. The left and right times of each plastic scintillator were measured with respect to the filtered RF. In addition, the integrated charges (Q_L, Q_R), number of BGO detectors firing simultaneously (fold) and the RF-BGO time were recorded in an event by event mode. The time calibration was done with a high precision commercial time calibrator. The en-

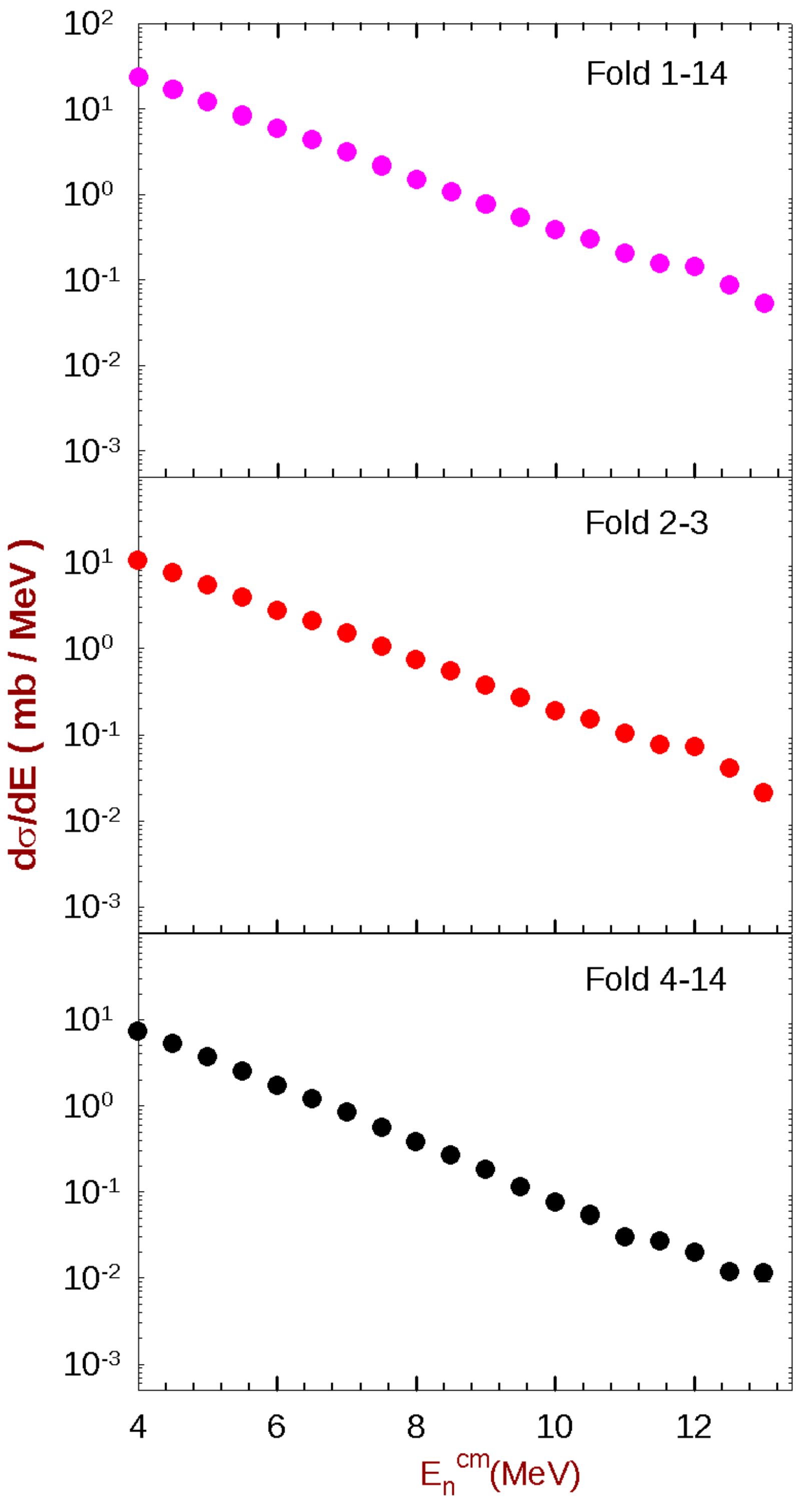

Figure 3.9: Measured energy differential neutron cross sections in the reaction ^{12}C+^{93}Nb at E(^{12}C)=40 MeV for various folds.

ergy calibration of the plastic scintillator was performed by taking Compton edges of 1.17 and 1.33 MeV(^{60}Co) and 4.44 MeV (^{241}Am-^{9}Be) γ-rays. The background contribution to the neutron spectra due to the presence of C and O impurities in the Nb target was measured to be less than 10% for fold 2-14.

In the offline analysis, the TOF was derived from T_L and T_R. The zero of the time scale was determined from the prompt gamma peak in the TOF spectrum. The position information was obtained from the ratio of integrated charges. A typical position spectrum deduced from the integrated charges is shown in Fig. 3.7. Four position gates were decided by inspecting the position spectrum. A TOF spectrum for a typical plastic scintillator with position gating on a quarter of its length and at least one BGO in coincidence is shown in Fig. 3.8. The random background reduces drastically with the BGO coincidence requirement allowing the measurement of neutrons with low production cross section. The fold gated neutron time of flight spectra, after subtracting the random background for each position cut, were converted to energy spectra. The energy dependent efficiencies of the neutron detectors of the array for different position gates were calculated using the Monte Carlo simulation program as mentioned in earlier chapter. The energy threshold used in the simulation was the same as that used in deriving the experimental spectra. The calculated efficiencies were used to obtain the energy differential cross-sections in the c.m. system. The c.m. spectrum for each fold was derived as the average of the corresponding spectra from all the 15 detectors and four positions. The energy differential cross sections in the c.m. system for folds $\geq$1, 2-3 and 4-14 are shown in Fig. 3.9.

The presence of the BGO detector array also contributes to scattered neutrons some of which are detected in the plastic array. In order to assess this contribution,

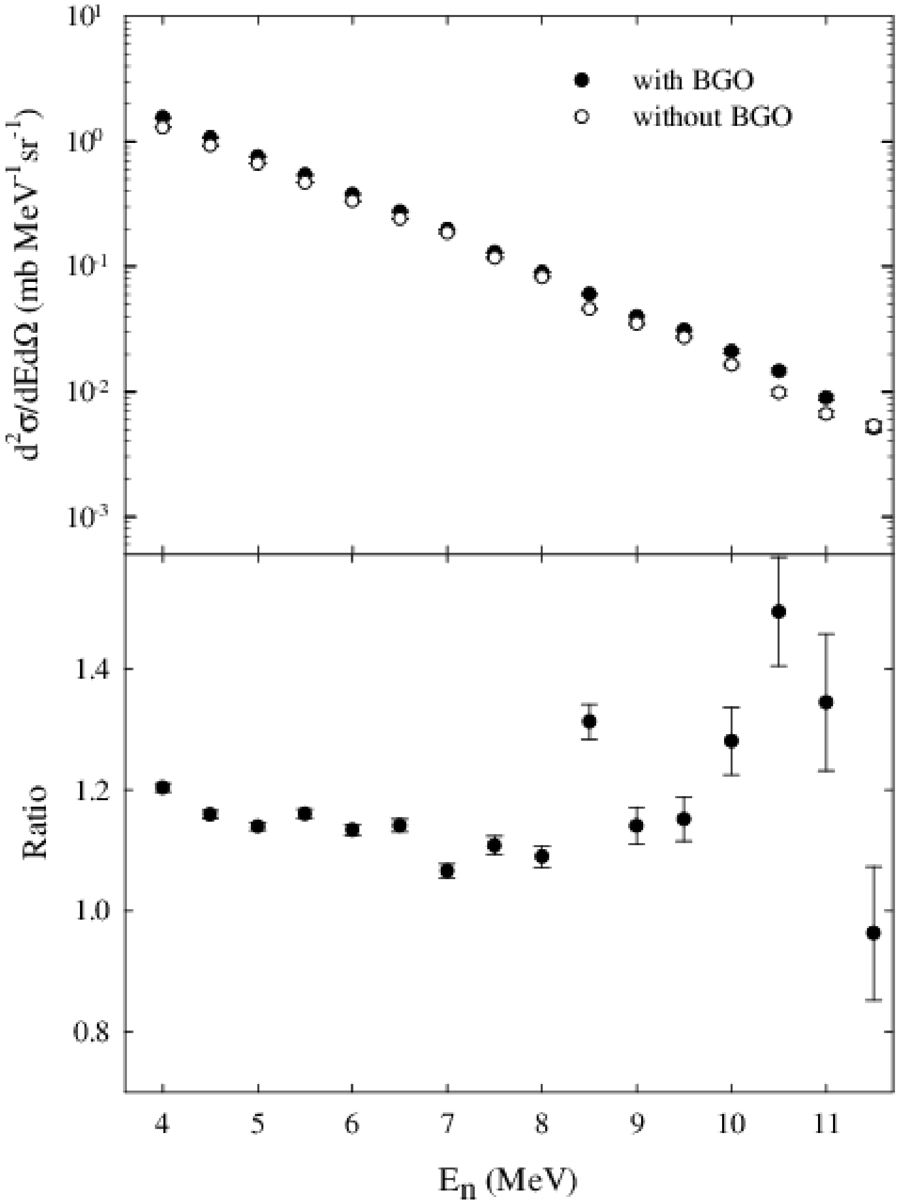

Figure 3.10: Measured energy differential neutron cross sections in the reaction $^{12}C+^{93}Nb$ at $E(^{12}C)=40$ MeV for fold ≥ 1 with and without top BGO array and the ratio between them at different neutron energies.

the neutron TOF measurements were performed with and without the top BGO detector array. Only the lower BGO array was used to generate the gamma ray multiplicity in both the cases. The measured differential neutron cross sections and their ratio for these two cases are shown in Fig 3.10. The presence of the top BGO array gives rise to an additional ∼13% contribution, almost independent of neutron energy, which is in reasonable agreement with the Monte Carlo simulation. This implies an additional ∼26% contribution due to the presence of the full BGO γ-multiplicity array.

3.7 Measurement addressing the Damping of the Nuclear Shell Effect

The NLD increases steeply with excitation energy (E_X). The excitation energy (E_X) dependence of the NLD is described by the level density parameter (a) . On the average a increases linearly with the mass number (A). However there is a large deviation from this linear behaviour at doubly closed shells and is maximum near the ^{208}Pb. This shell effect on the NLD parameter is expected to decrease asymptotically to its liquid drop value at excitation energies of $\sim$ 40 MeV[37]. Experimental information on such a damping is very limited. It is necessary to access the E_X dependence over a large range of energy, say from 5 to 50 MeV, to observe this effect on the NLD. The effect of shell correction on 'a' can be seen by comparing the particle spectra in the nuclei both near and away from shell closure. With this motivation, the triton transfer fusion reaction on ^{205}Tl was carried out at the PLF to populate the CN ^{208}Pb and evaporation neutron spectra measured by the time-of-flight (TOF) technique. A control experiment was also performed with ^{nat}Ta where the expected shell effect in the residual nucleus is small. The experiment was performed at the Mumbai PLF using a 30 MeV ^{7}Li

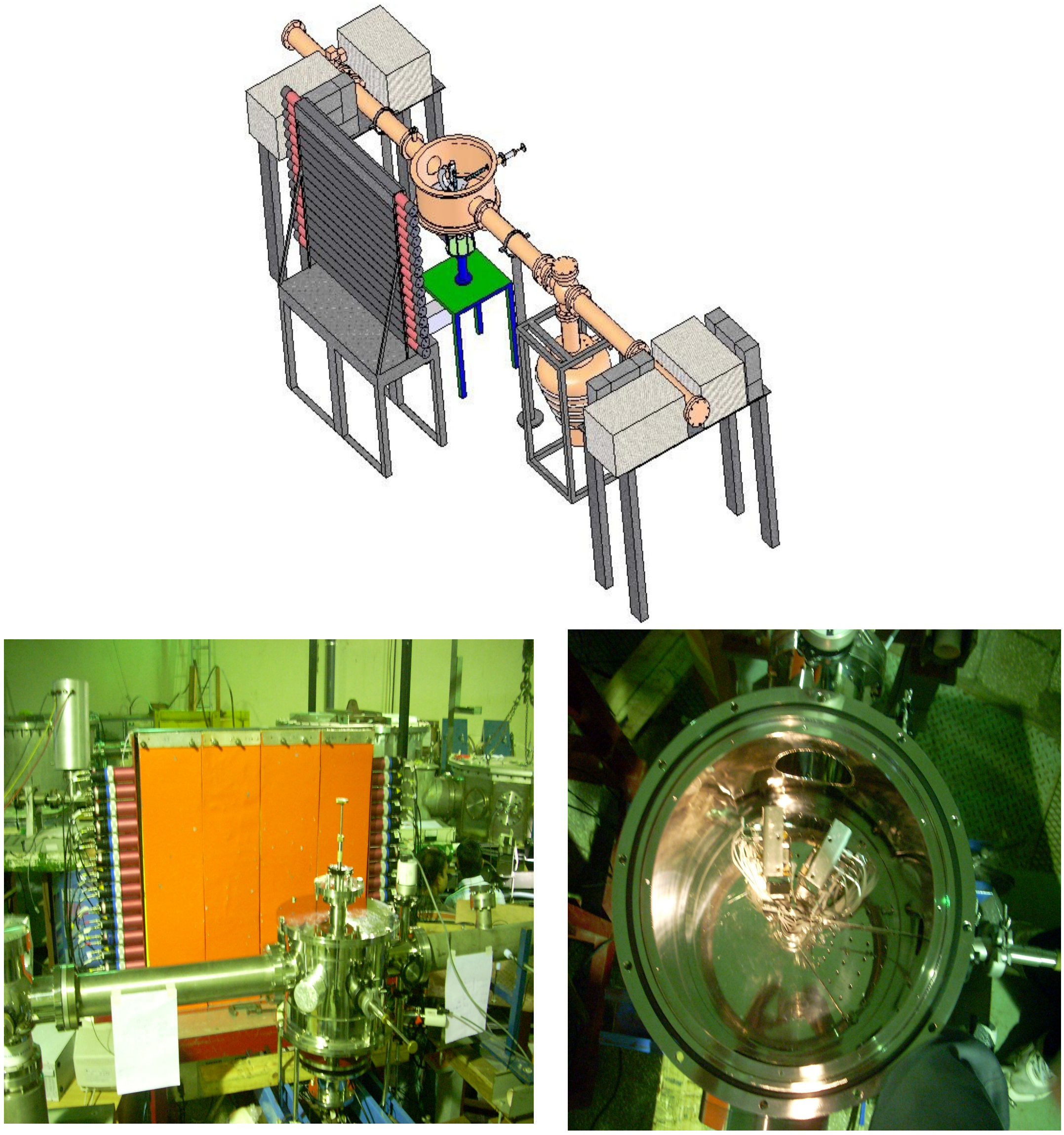

Figure 3.11: A schematic experimental setup (top) and photographs (bottom) show the neutron detector array covered with the Pb sheets and CsI(Tl) detectors mounted in the arms of the scattering chamber.

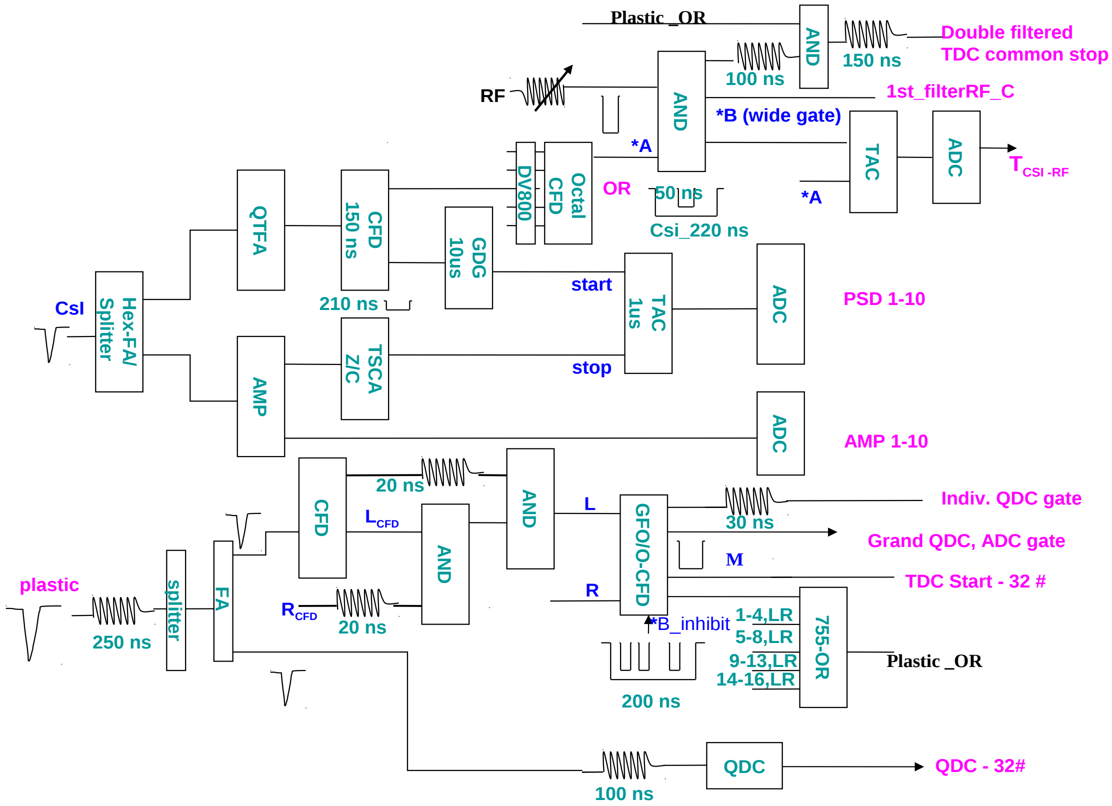

Figure 3.12: Block diagram of the electronics set up used in the neutron-alpha coincidence experiment.

pulsed beam of width ~1.5 ns (FWHM) and period ~107 ns. Self-supporting foils of 4.7 mg/cm^2 ^{205}Tl (enriched to >99%) and 3.7 mg/cm^2 ^{181}Ta (~100% natural abundance) were used as targets. Alpha particles were detected at backward angles (~125°-150°) with the CsI(Tl) detector array described in the previous chapter. Neutrons were detected using the detector array, also described earlier, with 15 elements and placed at 90° to the beam at a distance of 1 m from the target. The neutron energy was measured using the TOF. The schematic experimental setup with few photographs are shown in Fig. 3.11. The signals from each detectors were processed as per the electronics block diagram (see Fig. 3.12). The data

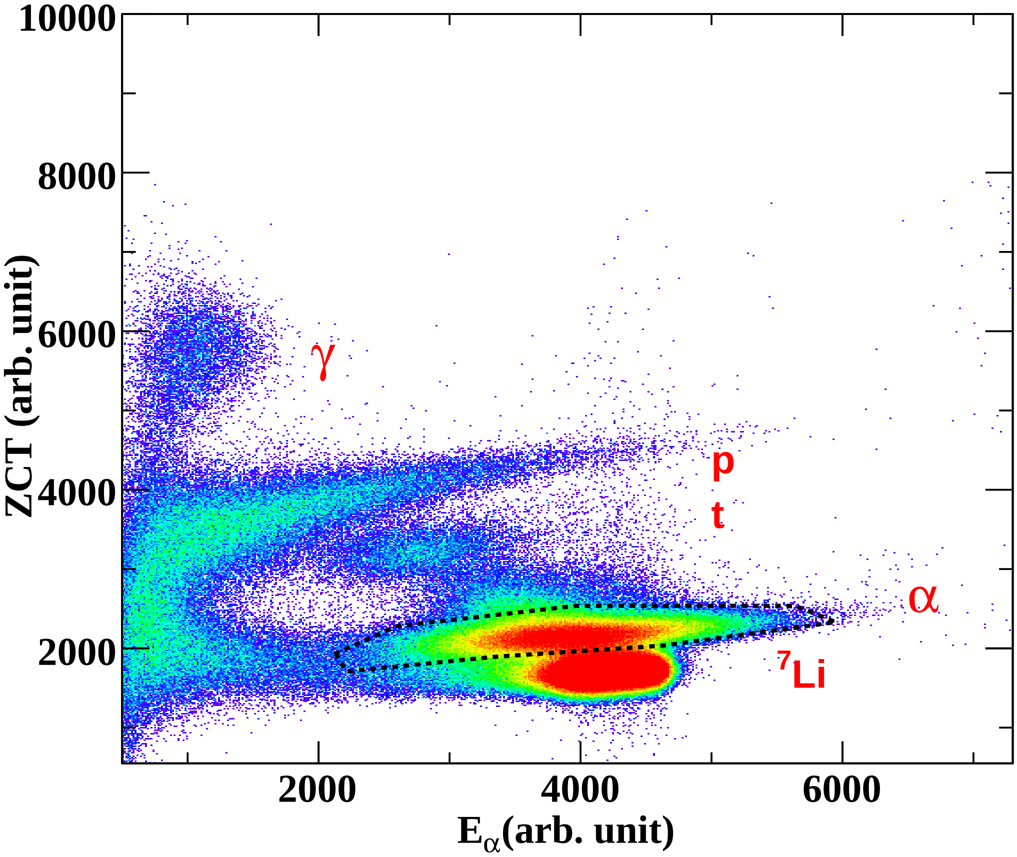

Figure 3.13: Two dimensional plot of ZCT vs energy deposited in one of the CsI(Tl) detectors in ^{7}Li+ ^{205}Tl reaction.

were collected in an event by event mode using a CAMAC based data acquisition system. The parameters recorded were (a) left (T_L) and right (T_R) timing of plastic scintillator with respect to the double filtered RF (RF filtered by both the CsI(Tl) and plastic scintillator) using time to digital converter (TDC), (b) deposited charge from left (Q_L) and right (Q_R) photo-multiplier tube(PMT) with charge to digital converter(QDC), (c) time of CsI(Tl) detectors with respect to the filtered RF using a TDC, (d) energy of CsI(Tl) detectors and (e) ZCT of the CsI detector for particle identification.

A typical ZCT - E_{CsI} 2D-spectrum is shown in Fig. 3.13 displaying a clean

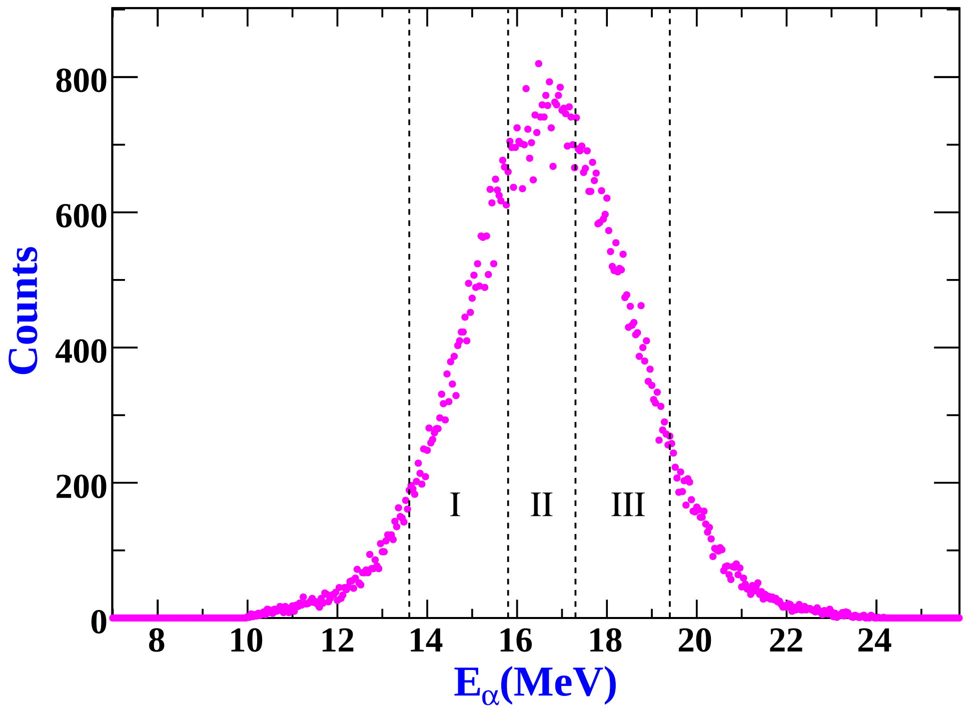

Figure 3.14: The projected alpha particles spectrum in ^{7}Li+ ^{205}Tl reaction for a suitable gating condition defined by the dotted two dimensional gate as shown in the Fig. 3.13. The vertical lines define three alpha energy bins (see text).

separation of various groups of particles. The energy calibration of the CsI(Tl) detectors, in the range $E_\alpha \sim$ 5 - 25 MeV, was done using a ^{229}Th alpha source and the ^{12}C(^{12}C, α)^{20}Ne reaction at E(^{12}C) = 24 MeV populating discrete states in ^{20}Ne. The projected alpha energy spectrum for the ^{205}Tl target is shown in the Fig. 3.14. The alpha spectrum peaks at 16.9 MeV(FWHM$\sim$4.5 MeV) with the ^{205}Tl target and at 16.3 MeV(FWHM$\sim$4.2 MeV) with the Ta target. These peaks correspond to α-particles having a beam like velocity ($E_\alpha \simeq \frac{4}{7}E_{^7Li}$). The calibration of the energy deposited in the plastic detector (in E_{ee}) was done using Compton tagged recoil electrons from ^{137}Cs and ^{60}Co γ-ray sources. The time calibration was done using a precision time calibrator.

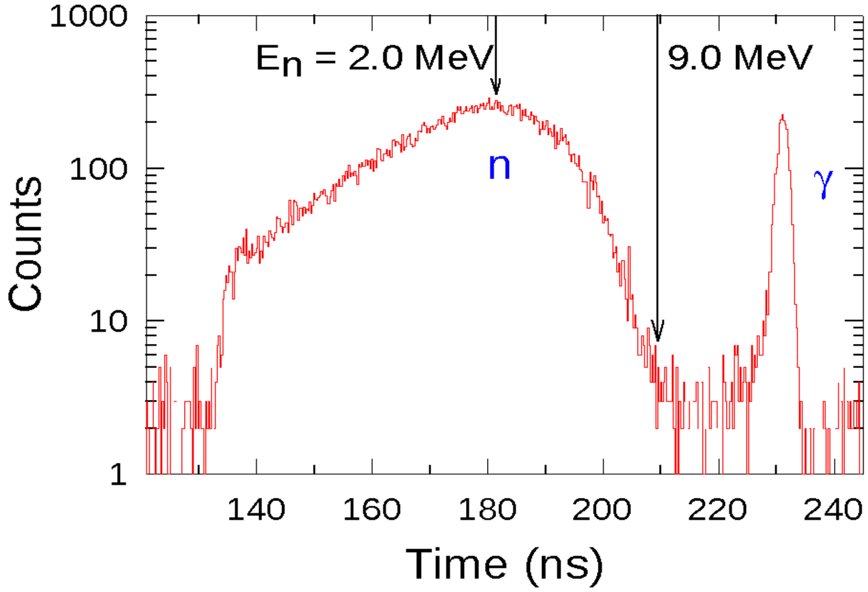

Figure 3.15: Time of flight spectrum in ^{7}Li + ^{205}Tl reaction for the central energy bin of alpha particles. The arrows indicate the positions for two representative neutron energies.

The time and energy spectrum of the plastic scintillator were calibrated. The time walk correction was done to better than 0.25 ns by inspecting the prompt gamma line in the 2D spectrum between the energy deposited in plastic and time of flight. The TOF, position information and geometric mean of the energy deposited for the neutron events in the plastic detector have been derived as explained in the previous chapter. In order to minimize the contribution of scattered neutrons a TOF dependent energy threshold (increasing with decreasing TOF) was used to obtain the final TOF spectra. A typical TOF spectrum is shown in Fig. 3.15. The efficiency of the plastic detector as a function of incident neutron energy and energy threshold was calculated using a Monte Carlo simulation code [65]. The efficiency corrected energy spectra of neutrons were derived from the TOF data. Furthermore, the random background was obtained by fitting the the data for

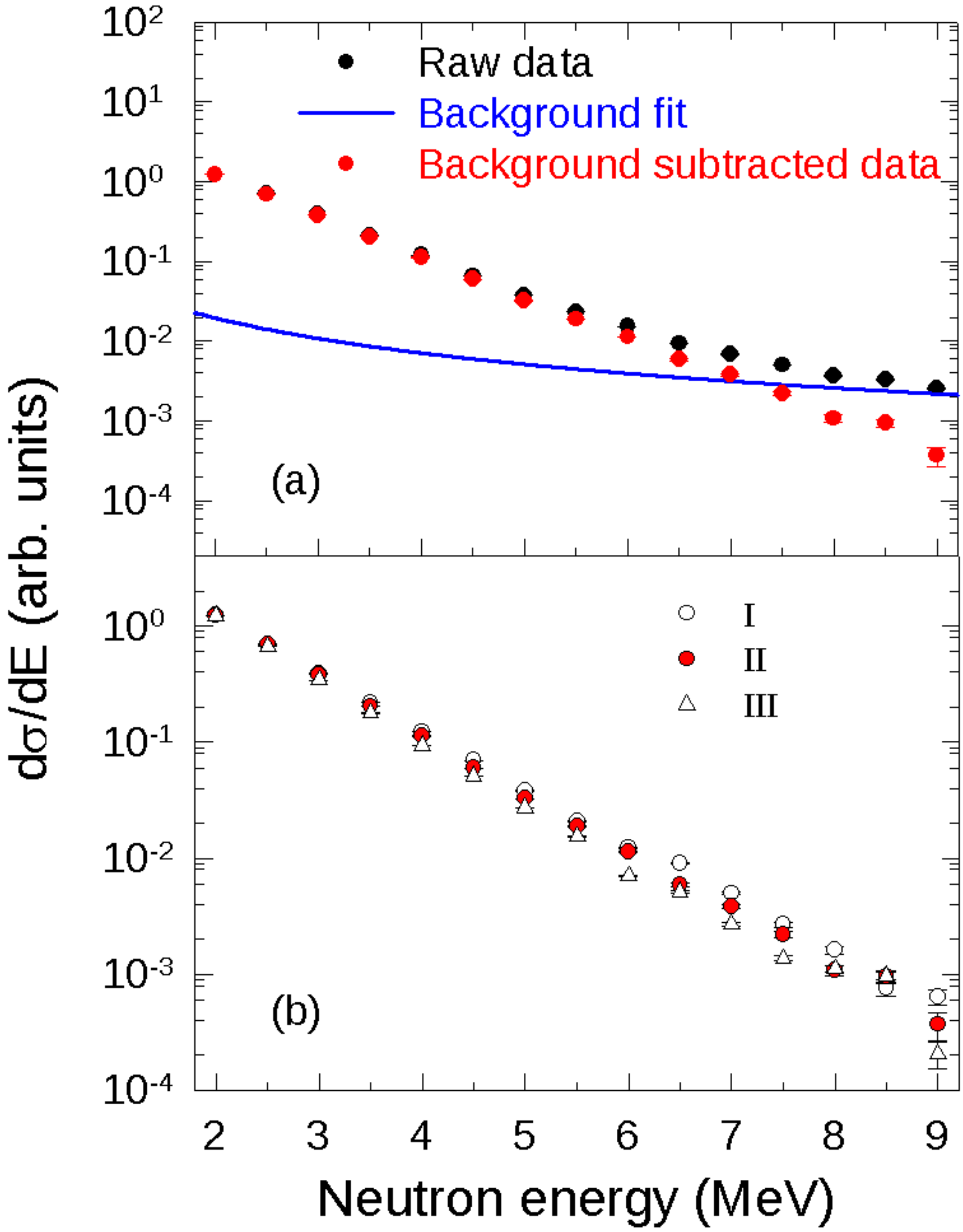

Figure 3.16: (a) Neutron spectrum from ^{205}Tl target and the corresponding background fit and background subtracted spectrum for the central alpha bin, (b) Measured neutron spectra after background subtraction for three alpha bins I, II, III (see Fig. 3.14).

$E_n \geq$9.5 MeV with a function ($\propto E_n^{-b}$, where b is a constant) and subtracted from efficiency corrected energy spectrum. An example of the background subtraction method used to obtain the final energy spectrum is shown in Fig. 3.16(a) for Tl target for the central alpha bin. The final neutron energy spectra for the Tl target are shown in Fig. 3.16(b) for three alpha energy bins, defined in Fig. 3.14. An overall decrease in the slope of the spectra with the increase in alpha energy (implying a decrease of E_X in ^{208}Pb) is consistent with the statistical nature of the neutron decay from an equilibriated nucleus.

4

Statistical Model Analysis

4.1 Introduction

The measurements of neutron reaction cross sections at low bombarding energies with various targets show resonances over a smoothly varying continuum. The widths of these resonances ($\sim$ 0.1 eV) are small compared to the spacing (typically 1-10^3eV) between them. The narrowness of these resonances with neutron reaction could be not explained with the potential-well model. In order to explain the width of these resonances, Bethe postulated that the resonances corresponds to many-particle excited states of the product nucleus rather the virtual single particle state of neutron in a nuclear potential well. This led to the conclusion by Bohr that the incoming neutron rapidly shared its energy with the nucleons of the target nucleus to form a composite system named as "compound nucleus". Bohr visualised the reaction as two step process in which the incident neutron undergoes multiple scattering in the target nucleus rapidly sharing the incident energy among all of the nucleons and forming a meta stable state. At this stage the memory of the entrance channel is lost and the subsequent evolution of the composite system depends only on conserved quantities. If the excitation energy reconcentrates on a nucleon or a group of nucleons near the surface of the nucleus as a result of random collisions there may be enough energy to eject the particles from the compound system or de-excitation may occur by the emission of γ-rays. Since the decay of the compound nucleus depends only on the conserved quantities of the compound nucleus, not on how it was formed, the compound nucleus formation and its decay were assumed to be independent.

If the projectile 'a' collides with a target nucleus 'A' forming the excited compound nucleus 'C' which subsequently emits a particle (or a γ-ray) 'b' leaving a residual nucleus B, the nuclear reaction can be depicted as,

$$a + A \rightarrow C \rightarrow B + b. \tag{4.1}$$

Let the channel a+A be represented by the symbol α and B+b by β. As a consequence of the independence hypothesis the cross-section associated with the reaction A(a, b)B may be factored into two parts, one corresponding to the formation cross section (σ_α =(a+A→C) capture cross-section of incoming particles) and the other corresponding to the probability of the compound nucleus (C) decaying into B+b (P_β=P(C→B+b)). Bohr's hypothesis can be written as

$$\sigma_{\alpha\beta} = \sigma_\alpha . P_\beta \tag{4.2}$$

The decay probability can be expressed as the ratio of the partial decay width

(Γ_β) to the total width (Γ) . The above expression can be rewritten as

$$\sigma_{\alpha\beta} = \sigma_\alpha . \frac{\Gamma_\beta}{\Gamma} \tag{4.3}$$

Weisskopf formulated the theory of compound nuclear decay [66, 67] based on classical statistical and geometrical arguments, which is the earliest statistical theory of decay of excited nuclei. The quantum mechanical treatment of this theory was presented by Hauser and Feshbach [68], which relies on the notion of the transmission coefficient.

4.2 Weisskopf formalism for compound nucleus

Weisskopf developed the statistical model (SM) of the compound nuclear reaction by comparing the emission of nucleons from an excited nucleus to the evaporation of molecules from a liquid drop as conceived by Frenkel.

Let the compound nucleus (C) be formed at excitation energy E and emit a neutron with energy ϵ. The residual nucleus (B) is left with an excitation energy $E_B = E - B_n - \epsilon$, where B_n is the binding energy of neutron. If a nucleus B with energy E_B and a neutron with energy between ϵ to ϵ+$d\epsilon$ and velocity v is enclosed in a volume V, then the probability per unit time (W_c) that the neutron will be captured to form the nucleus C with energy between E and E+dϵ is given by

$$W_c = \sigma(E, \epsilon) \frac{v}{V} \tag{4.4}$$

where $\sigma(E, \epsilon)$ is the mean cross section for the collision of a neutron with energy ϵ with a nucleus $B(E_B)$ producing the compound nucleus $C(E)$.

The decay probability per unit time of the nucleus C can be obtained as

$$W_n(\epsilon)d\epsilon = \sigma(E,\epsilon)\frac{gm\epsilon}{\pi^2 h^3}\frac{\rho(E_B)}{\rho(E)}d\epsilon \tag{4.5}$$

Using the relation of the entropy and temperature of the nucleus as defined in Chapter 1, The above expression can be rewritten as

$$W_n(\epsilon)d\epsilon = \sigma(E,\epsilon)\frac{gm}{\pi^2 h^3}e^{-E/T}\epsilon e^{-\epsilon/T}d\epsilon \tag{4.6}$$

This equation provides the expected kinetic energy spectrum similar to the spectrum of particles evaporated from an ideal fluid at a fixed temperature. Weisskopf's theory makes use of the reciprocity relation (given below) to relate the CN decay to the inverse reaction cross section which is calculated under certain assumptions.

$$\frac{\sigma_{\alpha\beta}}{k_\beta^2} = \frac{\sigma_{\beta\alpha}}{k_\alpha^2}. \tag{4.7}$$

where, k_α and k_β are the wave vector of the system in the entrance and exit channels.

4.3 Hauser-Feshbach formalism for compound nucleus

The angular momentum of entrance and exit channels were not considered while deriving the Weisskopf theory of particle evaporation. This was a fundamental drawback as the density of the nuclear states are strongly angular momentum dependent. The theory of Hauser and Feshbach is identical to the Weisskopf evaporation theory with proper angular momentum treatment to over come the short-comings.

Let the compound nucleus (C) be formed by the collision of the particle a to the target nucleus, A in the entrance channel a + A, denoted by α and the decay of the nucleus, C in to the exit channel B + b (denoted by β). According to Bohr hypothesis, the decay can be written as,

$$\sigma_{\alpha\beta} = \sigma_\alpha P_\beta \tag{4.8}$$

where P_β is the probability for compound nucleus decay to channel β. In the Hauser-Feshbach formalism, the Bohr hypothesis by assuming that independence applies to cross-sections corresponding to given values of the total angular momentum and parity. The independence hypothesis can be written for the channel α using the transmission coefficients (T_l), as

$$\sigma_{\alpha\beta}(l) = \frac{\pi}{k_\alpha^2}(2l+1)T_l(\epsilon_\alpha)P_\beta(l) \tag{4.9}$$

where $P_\beta(l)$ is the decay probability to a specific final state. The inverse reaction cross section for the same partial waves and the compound nucleus at same excitation energy can be written as,

$$\sigma_{\beta\alpha}(l) = \frac{\pi}{k_\beta^2}(2l+1)T_l(\epsilon_\beta)P_\alpha(l) \tag{4.10}$$

Using the reciprocity theorem and from the above two equations, we obtained the following inequality,

$$\frac{P_\alpha(l)}{T_l(\epsilon_\alpha)} = \frac{P_\beta(l)}{T_l(\epsilon_\beta)} \tag{4.11}$$

The decay to any channel β can be obtained as follows using this inequality,

$$P_{\beta}(l) = \frac{T_l(\epsilon_\beta)}{\sum_\gamma T_{\gamma,l}} \tag{4.12}$$

The above expression can be generalized by taking care the level densities in the residual nucleus and the compound nucleus as,

$$P_{\beta}(l) = \frac{T_l(\epsilon_\beta)\rho(E_B)}{\sum_\gamma T_{\gamma,l}\rho_C(E)} \tag{4.13}$$

Therefore, the basic Hauser-Feshbach equation for spinless particles [69] using the reciprocity relation and the inverse cross section for a given partial wave (l) which depends on the transmission probability (T_l), can be written as

$$\sigma_{\alpha\beta}(l) = \frac{\pi}{k_\alpha^2}(2l+1)\frac{T_l(\epsilon_\alpha)T_l(\epsilon_\beta)\rho(E_B)}{\sum_\gamma T_{\gamma,l}\rho_C(E)} \tag{4.14}$$

Since intrinsic angular momenta of the projectile (s) and the target (S) are almost always involved, this expression for spinless particles in practice is not very useful for the calculation of cross section. Let J be the angular momentum of the CN, $J = l + j$, where $j = s + S$ and S' be the angular momentum of the residual nucleus B. Then the above expression can be modified as

$$\sigma_{\alpha\beta}(J,S) = \frac{\pi}{k_\alpha^2}\sum_{l,j}(2l+1)g_\alpha T_l(\epsilon_\alpha)\frac{\displaystyle\sum_{l',j'} T_{l'}(\epsilon_\beta)\rho(E_B*, S')}{\displaystyle\sum_{\gamma,l'',j''} T_{\gamma,l''}\rho_C(E*)} \tag{4.15}$$

and

$$\sigma_{\alpha\beta}(J,S) = \frac{\pi}{k_\alpha^2}\frac{2J+1}{(2s+1)(2S+1)}\frac{\sum\limits_{lj,l',j'} T_l(\epsilon_\alpha)T_{l'}(\epsilon_\beta)\rho(E_B*,S')}{\sum\limits_{\gamma,l'',j''} T_{\gamma,l''}\rho_C(E*)} \tag{4.16}$$

where unprimed symbols represent quantities associated with the entrance channel and primed symbols for the exit channel.

4.4 Statistical model algorithm

In the heavy ion fusion reaction the compound nucleus is created at an excitation energy(E) and angular momentum(J). The decay rate through any channel is calculated by the reciprocity relation using the capture cross section in the inverse channel. The total decay rate is the sum of the decay rates of all possible channels. The probability of decay to a particular channel can be obtained by the ratio of the particular decay rate to total decay rate. The cross section for that particular channel is given by the decay probability multiplied by the fusion cross section to form the CN [10, 70].

The decay width for particle emission can be obtained from the following equation

$$\frac{d\Gamma}{d\epsilon} = \frac{1}{2\pi}.\frac{\rho(J_B,E_B)}{\rho(J,E)}\sum T_l \tag{4.17}$$

where the summation extends over all possible orbital angular momenta(l) and channel spins and T_l is the transmission coefficient calculated from the optical potential seen by the particle due to the excited target at excitation energy E_B and spin J_B. It can be seen from this equation that the rate (or the decay width) of particle evaporation from an excited CN depends upon the NLD of the residual nucleus. The details of the NLD have been discussed in Chapter 1.

The transmission coefficient for the l^{th} partial wave, T_l, is given by

$$T_l = 1 - |\eta_l|^2 \tag{4.18}$$

where $\eta_l = e^{2i\delta_l}$ is the complex scattering amplitude and δ_l is the optical model phase shifts. The compound nuclear formation cross section is given by

$$\sigma_\alpha = \frac{\pi}{k_\alpha^2} \sum_{l=0}^{\infty} (2l+1) T_l \tag{4.19}$$

The SM starts with the assumption that the CN is formed in statistical equilibrium with respect to all degrees of freedom. The spin distribution of the CN is usually calculated from the known fusion cross section using a strong-absorption model. The decay of the excited CN by particle emission is calculated from the Hauser and Feshbach formula. The decay probability is determined by the transmission probability, which is calculated from the optical potential and the E_X and J dependence of the NLD including the structure effects of the residual nucleus. The relative decay widths for n, p, α-particle and γ-ray emission are calculated and a matrix, containing the population of the daughter nuclei as function of E_X and J, is generated. The CN decays primarily with the emission of light particles such as n, p or α-particles. These particles carry most of its excitation energy and the particle emission stops once the nucleus reaches an excitation energy below the particle emission threshold ($\sim$8 MeV above the yrast line). The nucleus decays subsequently to its ground state by losing the residual energy and most of its angular momentum by emission of many low energy γ-rays. The statistical model based computer code CASCADE [71] with extensive modifications [32, 42] has been used to understand the γ-ray multiplicity or fold gated p, n and α-particle spectra and also study the influence of shell effect on the nuclear level density.

4.5 Systematic behaviour of breakup alpha in ^{7}Li induced reaction

The production cross section of α particles in ^{7}Li+^{205}Tl reaction at 30 MeV is one of the important input parameters of the SM calculation to simulate the neutron evaporation spectrum from an excited ^{208}Pb in the present work. The production of α particles was measured in ^{7}Li induced reaction on heavy targets from ^{181}Ta - ^{209}Bi at the energies near the Coulomb barrier from 25-35 MeV. The total inclusive α cross sections were obtained from the measured angular distributions for various targets. In order to eliminate the geometrical effects, the reduced cross section was calculated by scaling the total alpha cross section by r_{pt}^{2}, where $\mathrm{r}_{pt} = A_p^{1/3} + A_t^{1/3}$ and the reduced energy was obtained by dividing the center of mass energy by $Z_p.Z_t/r_{pt}$ [72]. Here Z_p , Z_t are the atomic numbers and A_p, A_t are the mass numbers of the projectile and target, respectively. The reduced cross sections are plotted against the reduced energies for all targets in Fig. 4.1. The calculated reduced total cross sections have a universal behaviour at near barrier energies. Triton capture cross section measured by offline γ-ray counting techniques in ^{7}Li+^{198}Pt system [73] reasonably fits the same behaviour. The total α cross section in ^{7}Li+^{205}Tl at 30 MeV is found to be $\sim$40 mb [74].

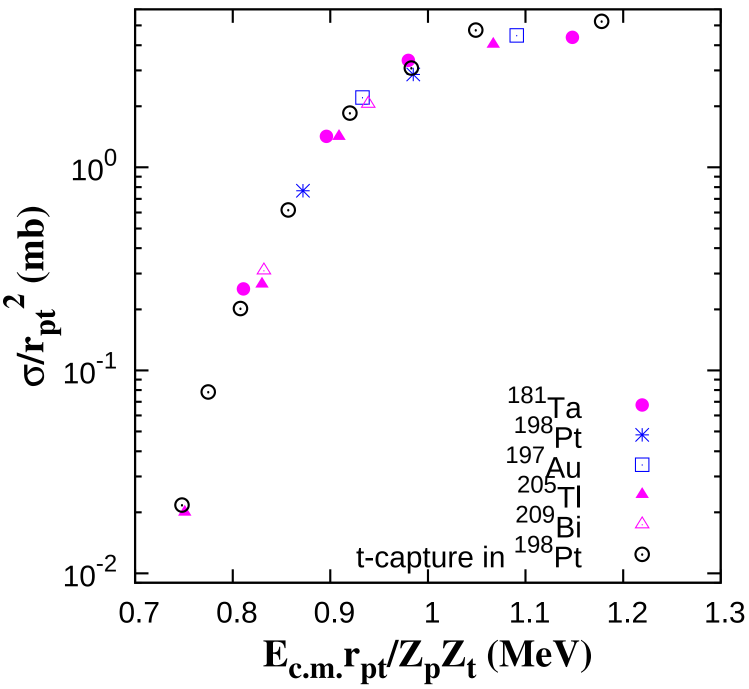

Figure 4.1: Systematic of the reduced cross section for ^{7}Li induced reaction on heavy targets.

4.6 Statistical Model simulation of fold gated neutron spectra in $^{12}C+^{93}Nb$ reaction

The γ-ray multiplicity gated particle spectra reveal the information of the E_X and J dependent NLD in the residual nucleus. A statistical model calculation using the simulated Monte Carlo CASCADE (SMCC) [75] code was performed to compare with the measured spectra. The calculation was done for the projectile energy of 39.5 MeV (at the centre of the target), a fusion cross-section of 188 mb [42] and a probability distribution of angular momentum populated in the CN. The

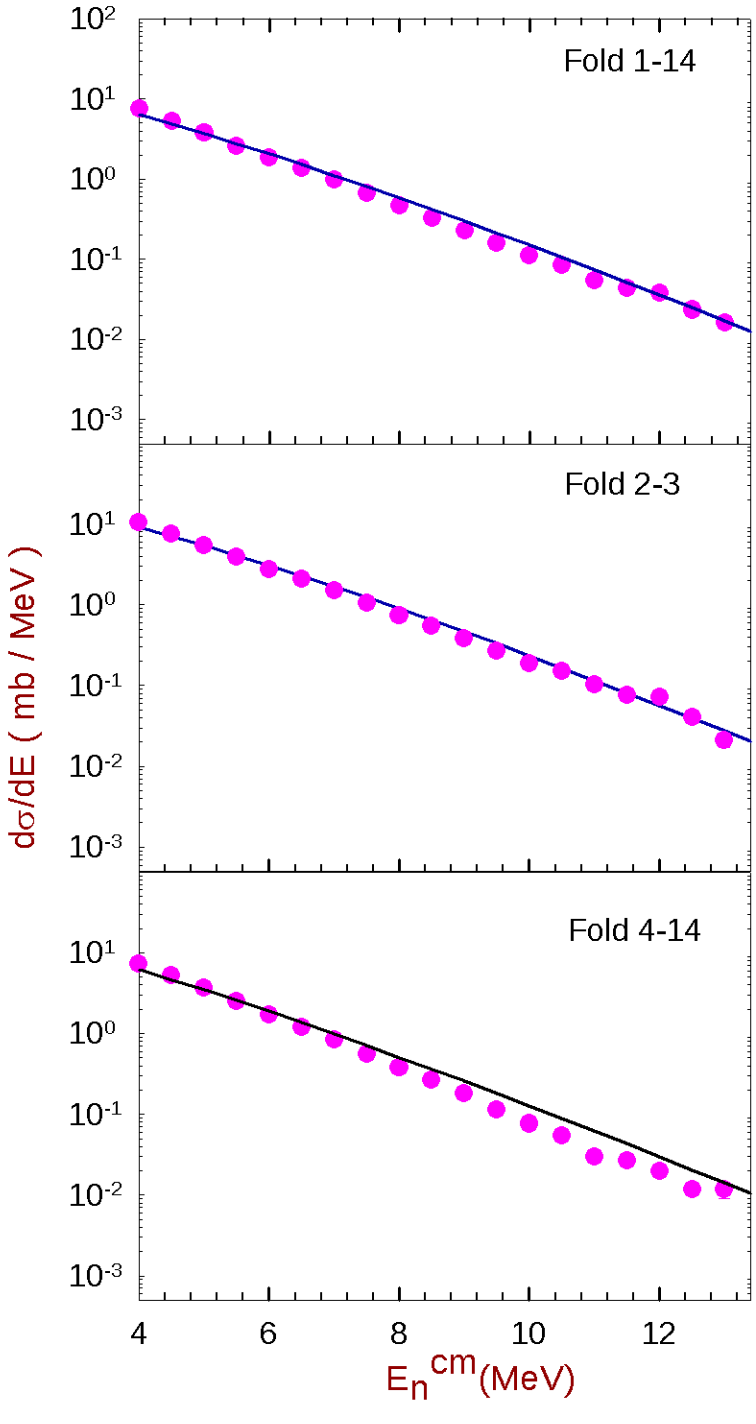

Figure 4.2: Measured energy differential neutron cross sections in the reaction ^{12}C+^{93}Nb at E(^{12}C)=40 MeV for various folds and statistical model calculations (SMCC) with a=A/8.5 MeV^{-1}.

probability distribution used for the angular momentum is given by

$$P(l) \sim \frac{(2l+1)}{1+exp[(l-l_0)/\delta_l]} \tag{4.20}$$

Here $l\hbar$ is the orbital angular momentum of incident channel and δ_l is the diffuseness parameter. The value of $l_0 = 10\hbar$ and $\delta_l = 3\hbar$ were used in this SM calculation. The particle emission from the CN was computed within the framework of the statistical model using proper transmission coefficients for n, p and α-particles and the (E_X and J) dependent NLD prescription for the residual nucleus. Eventually the SMCC calculation generated the population matrix $\sigma(E_n, J_{res})$, where J_{res} refers to the residue spin. The J_{res} to F (fold) response function was calculated using a Monte Carlo program with BGO efficiency and inter-detector cross talks as inputs and assuming the multiplicity$M = J_{res}/1.9 + M_0$ with M_0=1.4. Using this response function, the fold gated neutron spectra were obtained from $\sigma(E_n, J_{res})$. The calculated energy spectra for various folds are shown in Fig 4.2. The shape of the experimental fold gated neutron spectra agree well with those given by the SMCC calculation for a level density parameter of A/8.5 MeV^{-1} [76]. This level density parameter is similar to that derived from the analysis of the proton spectra from an earlier measurement in the same system [77].

The broad structures in the proton spectra in the same system at the same beam energy were seen [42] at the proton energies of >15 MeV for Fold$\geq$4. Considering the difference in the neutron and proton separation energies from the compound nucleus and the difference in pairing energies of the nuclei after the first step decay, these structures are expected for neutron energies above 12 MeV. While no prominent structure can be seen in Fig 4.2, a higher statistics measurement with better beam timing is needed to extract unambiguous data in the high energy part of the neutron spectrum.

4.7 Damping of the nuclear shell effect in ^{208}Pb region

The exclusive measurement of neutron spectra from ^{208}Pb, formed in the excitation energy range 19 - 23 MeV following triton transfer in the ^{7}Li+^{205}Tl reaction was carried out, in coincidence with ejectile alpha particles. The ^{208}Pb nucleus decays predominately by first step neutron emission populating ^{207}Pb in the $E_X \sim 3$ - 14 MeV. Over this E_X range, the NLD parameter is expected to show a significant change due to the damping of the shell effect. An important assumption is that the nucleus formed in this technique is in equilibrium with respect to all degrees of freedom. The SM analysis of the neutron spectra from the ^{208}Pb can reveal important parameters related to the damping of the shell effect in this mass region. It may be noted that the contribution of second step neutrons populating the ^{206}Pb where the shell effect is also significant was included in the calculation. Another control measurement was carried out with a ^{181}Ta target populating nuclei in the ^{184}W region where the shell effect is expected to be small. The SM analysis of the neutron spectra was done using the code CASCADE [71] with the E_X and J dependent NLD, $\rho(E_X, J)$, and the production cross section $\sim$ 40 mb. The excitation energy dependence of the NLD parameter a, which includes the shell effect and its damping, has been parameterised by Ignatyuk [38] as

$$a = \tilde{a}[1 - \frac{\Delta_S}{U}(1 - e^{-\gamma U})].$$

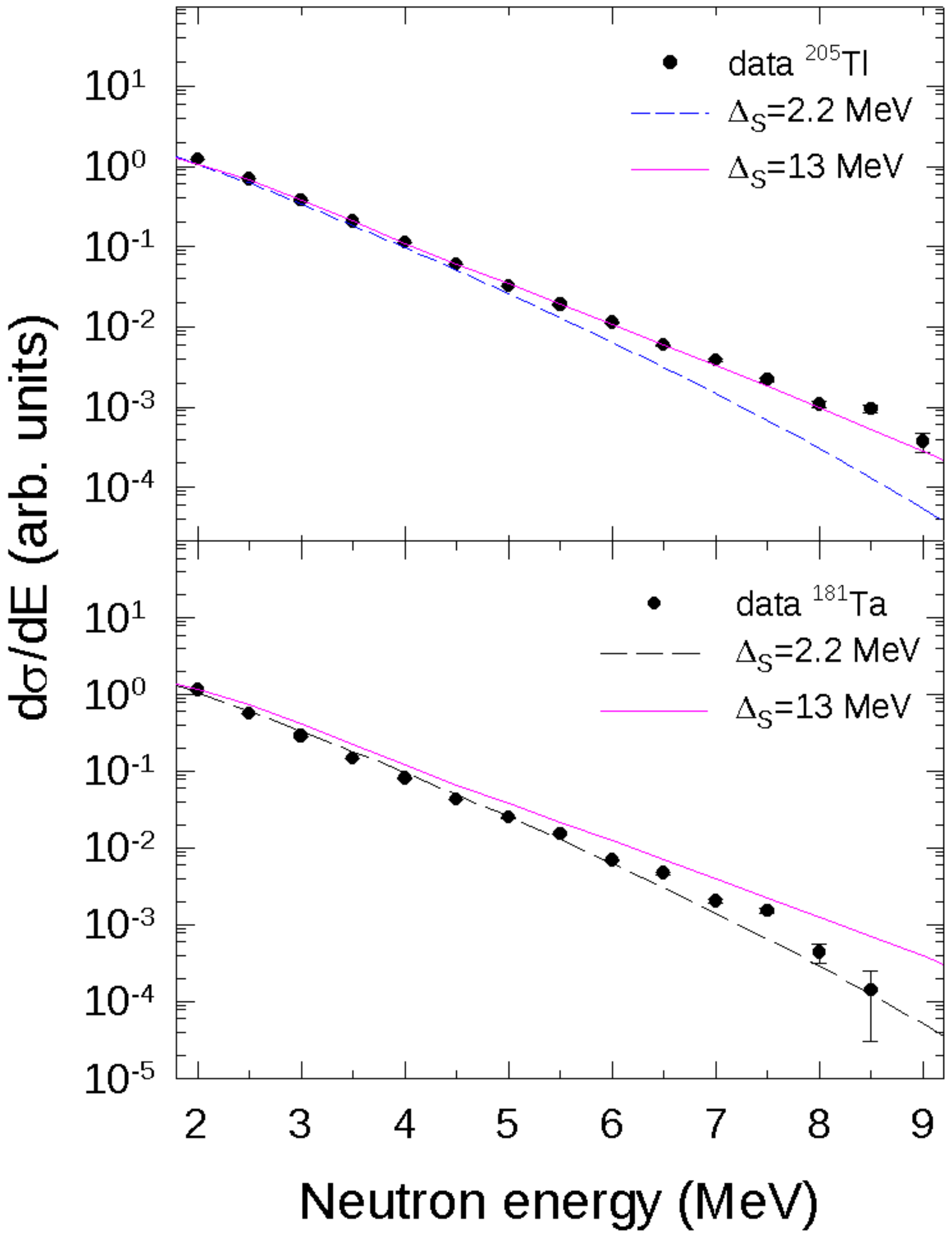

Figure 4.3: (a) and (b) show measured neutron spectra from ^{205}Tl and ^{181}Ta targets and statistical model (SM) calculations for the central alpha energy bin which corresponds to an excitation energy of ^{206}Pb $\sim$ 21 MeV.

Here $\tilde{a}$ is the asymptotic value of the NLD parameter in the liquid drop region, Δ_S is the shell correction energy, which is the difference between the experimental binding energy and that calculated from the LDM and γ is the damping parameter. Figs. 4.3(a) and (b) show the calculated spectra using $\tilde{a}$ = A/8.5 MeV^{-1} and γ = 0.055 MeV^{-1} [78]. It is seen from the figure that a shell correction energy Δ_S = 13.1 MeV (for ^{207}Pb) fits the shape of neutron spectrum for the Tl target while Δ_S = 2.2 MeV does not. An opposite behaviour is seen for the Ta target. These values agree with those obtained from the experimental nuclear masses and the calculated LDM values[7]. The present data, therefore is consistent with the shell correction energies derived from the nuclear masses.

4.7.1 Exclusion plot between the δa and γ

It may be pointed out that constraining all the three parameters, $\tilde{a}$, Δ_S and γ, is not possible from the data even if one can access a much wider excitation energy range. By fixing any two parameters the third one can be constrained. Since the shell correction energy is known with a reasonably good accuracy (within a few hundred keV [7]), an acceptable range of $\tilde{a}$ and γ have been searched for a fixed Δ_S. The shell correction energy was taken as 13.1 and 11.7 MeV for ^{207}Pb and ^{206}Pb, respectively. These two nuclei are only relevant in the present case because the first two steps of neutron emission describe the full spectra. The calculations were performed with δa (= A/$\tilde{a}$) ranging from 6.5 - 11.0 MeV varying with a step of 0.5 MeV and γ ranging from 0.02 - 0.08 MeV^{-1} varying with a step of 0.005 MeV^{-1}. Fig. 4.4(a) shows statistical model fits for the central alpha energy bin for δa = 8.5 MeV and three γ values. The quality of the fits can also be judged from the ratio plots shown in Fig. 4.4(b). A value of γ=0.060 MeV^{-1} gives a

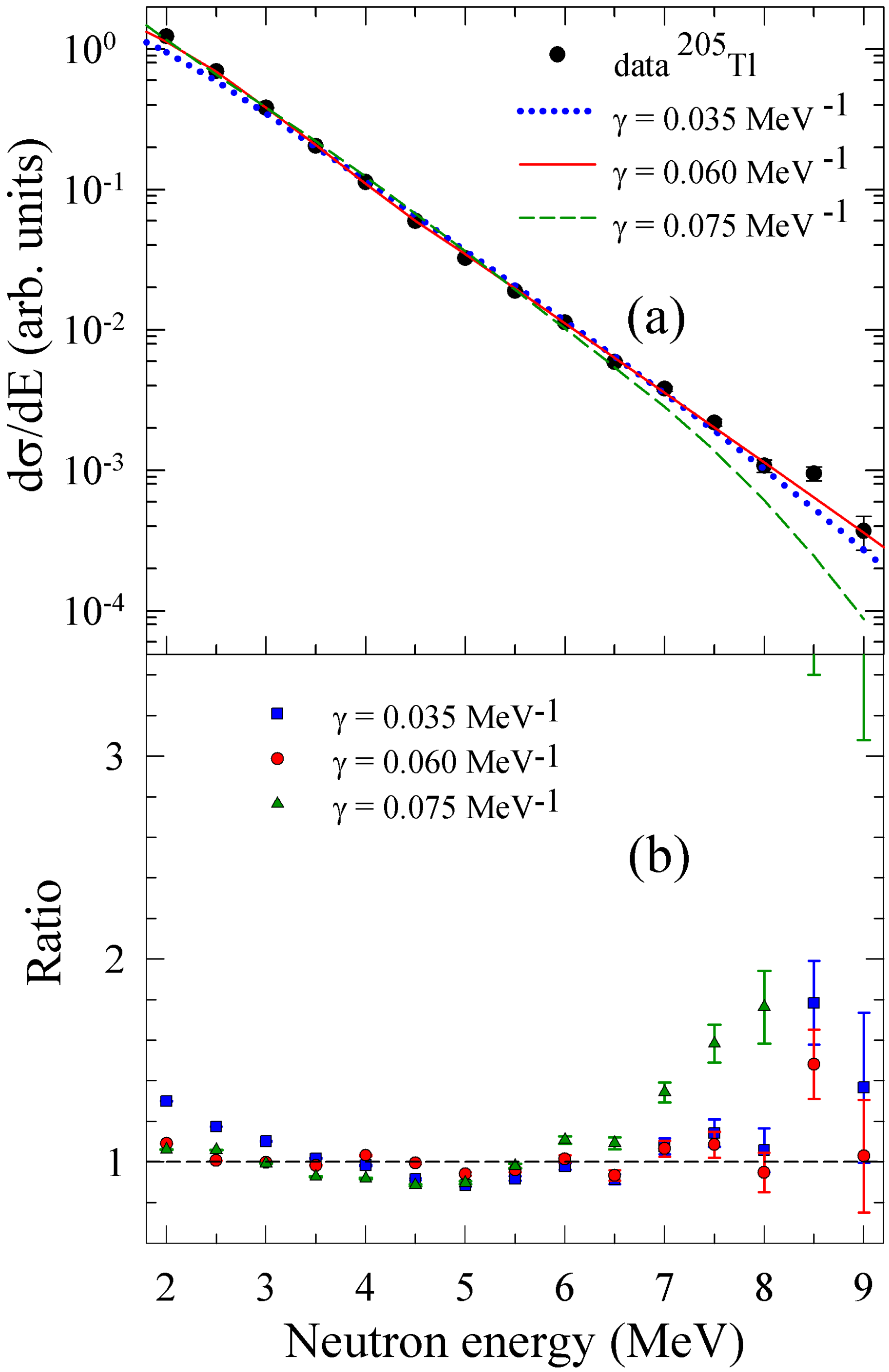

Figure 4.4: (a) Comparison of data with SM calculation using $\Delta_S = 13.1$ MeV (for ^{207}Pb) and 11.7 MeV (for ^{206}Pb) for three values of γ and (b) Ratio plot of data to fits for these γ values

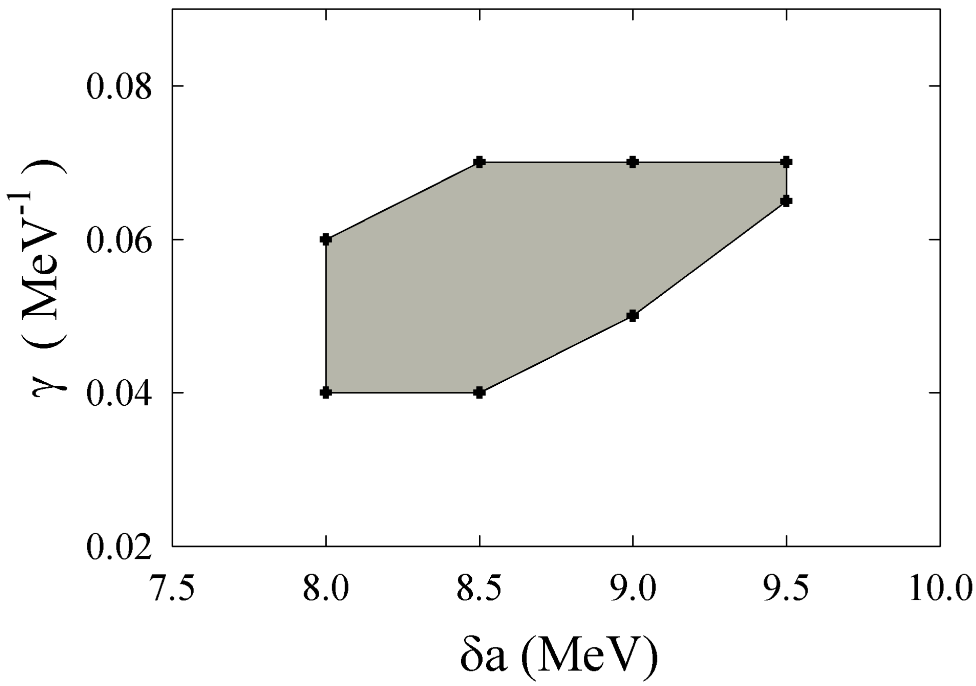

Figure 4.5: Exclusion plot of δa - γ, where δa = A/$\tilde{a}$, for the shell correction energies quoted in Fig. 4.4. The acceptable values are within the contour.

good fit while the other two values can be discarded. It may be mentioned that a change in shell correction energies up to 0.5 MeV has <2% effect on the shape of the spectra. Similar analysis has been done for the other two alpha energy bins. Fig. 4.5 shows a (δa - γ) two dimensional exclusion plot, the region inside the contour representing the acceptable range of the parameter values for fitting the present data. The criterion of rejection is based on both the relative χ^2 values and the visual inspection of the fits over a range of E_n=2 - 9 MeV. It can be seen from the figure that the acceptable range of δa lies between 8.0 and 9.5 MeV. The parameter γ controlling the damping of the shell effect can be constrained to ($0.060^{+.010}_{-.020}$) MeV^{-1}. This is different from the value extracted from the neutron resonance data within errorbars *viz.* (0.079 ± 0.007) MeV^{-1} [79]. This could be due to the differences in the angular momentum states sampled in the two works. Moreover, the present work addresses a specific nuclear region whereas the analysis of Ref. [79] is global in character.

4.7.2 Possible sources of uncertainties in the method

There could be two possible sources of uncertainties in the present experimental method. First, the pre-equilibrium contribution to the neutron spectra which may contaminate the high energy part of the spectrum and the second, the various reaction mechanisms which may contribute to the α-coincident neutron spectra.

The nucleus could decay before thermalisation and compound nucleus formation. However, such pre-compound contributions to the neutron emission are expected to be small at the near barrier energy [80, 81] relevant to the present experiment. This can be assessed by measuring the angular distribution for higher beam energy where this effect is expected.

It may be noted that the major contribution to the α-coincident neutron spectra is expected to arise from triton transfer-fusion reaction. There are other direct processes that could also contribute. The proton pickup and 2-neutron transfer cross sections are small [82] and can be ignored. A Monte Carlo calculation of the alpha-neutron coincidence spectrum reveals that the contribution from the one neutron and one proton transfer is a small fraction ($< 5\%$) in the region of interest, even if the cross sections are the same as that of the main reaction. The most relevant reaction is the deuteron transfer followed by ^{5}He breakup. However, the spectroscopic factor for the d+^{5}He configuration is expected to be much smaller than the t+^{4}He configuration [83] leading to a small contribution from this reaction.

5

Conclusion and future outlook

5.1 Summary and conclusion

The nuclear level density makes a transition from the shell-dominated regime at low excitation energy to that of a classical liquid drop at high excitation. It is important to study how the shell effect damps out with the excitation energy range. Since the shell correction in ^{208}Pb has the maximum value (∼13 MeV), the damping of the shell effect can be better studied experimentally in the Pb region. So far no such measurement on the damping of shell effect on nuclear level density has been reported. In order to address this effect over a wide excitation energy range, an exclusive measurement of neutron spectra from ^{208}Pb in the excitation energy range 19 - 23 MeV was carried out. The nucleus was populated in a triton transfer reaction with ^{7}Li projectile and the measurements were made in coincidence with alpha particles. For this purpose, an array of neutron detectors based on plastic scintillators with reasonably good efficiency (typically ∼22% at 10 MeV) and a charged particle array based on CsI(Tl) scintillation detectors (for alpha particle) have been developed.

The array of plastic detector ($\sim$1$\times$1 m^2) has been set up for the neutron time of flight measurements at Mumbai PLF. The response of the detector to electrons using radioactive sources and mono-energetic neutrons using the ^{7}Li(p,n$_1$) reaction has been measured. A Monte Carlo simulation program has been developed to calculate the response of the detector for neutrons. The results are in agreement with the experimental measurements. The detector array was used to measure the energy differential neutron cross sections in the reaction ^{12}C + ^{93}Nb at E(^{12}C) = 40 MeV in coincidence with a 14-BGO gamma multiplicity array. The measured spectral shape is in reasonable agreement with a statistical model calculation.

A charged particle detector array consisting of 8 CsI(Tl) detectors with active area of 2.5 cm $\times$ 2.5 cm and the thickness of 1 cm has been set up to detect the light charged particles with a reasonably large efficiency. The scintillation light is collected by a silicon PIN photodiode and pre-amplifier coupled to the CsI(Tl) detectors. The standard pulse shape discrimination method is used for the particle identification by measuring the zero cross over timing (ZCT) of the amplified bipolar pulse. The response of the detector to alpha particles from $\sim$5 to 40 MeV was measured with alpha particles from ^{229}Th source and ^{12}C(^{12}C, α)^{20}Ne reaction populating discrete states in ^{20}Ne.

A feasibility experiment was carried out to measure the time resolution of pulsed ^{7}Li beam with respect to a BaF$_2$ detector. The measured pulse width was found to be $\sim$1.4 ns, which is adequate for the neutron TOF experiment with the neutron detector array described earlier. In addition, the production of α particles was measured in ^{7}Li induced reaction on heavy targets from ^{181}Ta - ^{209}Bi at the energies near the Coulomb barrier. The total α cross section in ^{7}Li+^{205}Tl at 30 MeV is found to be $\sim$40 mb. This cross section in ^{7}Li+^{205}Tl reaction is adequate for meaningful neutron-alpha coincidence experiment with the above mentioned detector arrays.

The effect of the shell correction on the level density parameter over a range of excitation energy where the effect of damping is significant has been measured for the first time. The experimental results show that the shell correction is indeed necessary to explain the data and is pronounced in the Pb region while it is small for the nucleus ^{183}W which is away from shell closure. The shell damping factor $\gamma = (0.060^{+.010}_{-.020})$ MeV^{-1} has been extracted from the present data. This value is different from the value,(0.079 $\pm$ 0.007) MeV^{-1}, extracted from the neutron resonance data. An exclusion plot between δa and γ has been made from the SM analysis of the present data.

A precise measurement of the damping parameter in heavy magic nuclei will be an useful input in the study of the formation of super heavy nuclei from heavy ion fusion reactions and also useful for nuclear astrophysics.

5.2 Future outlook

The measurement of neutron evaporation spectra from ^{208}Pb trough triton transfer fusion reaction has been shown to be useful in addressing the damping of the nuclear shell effect in Pb region. However, there are scopes for improvement of the present method in the areas listed below.

1. **Use of Si strip detectors**

   The Si strip detector ΔE-E telescope can be used instead of CsI(Tl) detectors for the identification of various particles emitted in the reaction. The Si strip detector can handle a significantly higher count rate compared to the CsI(Tl) detector where the pulse shape discrimination is poor at high count rate because of the pileup effect. Moreover, this will help to quantify the various reaction mechanisms, such as ^{6}Li*+n followed by ^{6}Li* breakup to α+d, contributing to the neutron-alpha coincidence events.

2. **Use of Liquid Scintillator detectors**

   The liquid scintillator detector has very good time resolution like the plastic scintillator. In addition this detector has pulse shape discrimination property for discriminating the neutron induced events from the gamma ray induced events. Therefore, the contribution from the delayed gamma rays to the neutron spectra can be considerably reduced.

3. **Improvement on beam timing**

   The pulsed beam, used to generate the reference time for the TOF experiment, should have very good time resolution and good line shape with no structure near the baseline. The time resolution of the pulsed beam can be improved significantly by rebunching the pulsed beam using the LINAC superbuncher of the PLF. A time resolution of the pulsed beam better than 800 ps can be obtained with the LINAC prebuncher and supperbuncher.

4. **Use of VME data acquisition system and Digital Pulse processing and acquisition**

   The data of the neutron-alpha coincidence experiment were recorded using a CAMAC data acquisition system (DAQ) which can handle the event rate up to ∼1 kHz. The VME DAQ can easily accommodate an event rate of 3-5 kHz.

Therefore, the VME system can be used for acquiring the data with higher beam current in order to improve the statistics in the high energy part of the spectrum. The entire electronics and data acquisition can be augmented to the digital signal processing to increase the throughput and simplified the electronics setup.

A systematic study of the shell effect on the nuclear level density in the Pb region at higher excitation energy up to 50 MeV will be useful to understand the damping of shell effect over a wide excitation energy range. Further the damping of shell effect can be addressed using other reactions with various exit channels, namely (α,p), (α,n) etc., which produce the residual nuclei such as Pb, Bi, Po, where the shell effect is large.

Finally, it would be interesting to study the rotational enhancement effect in deformed nuclei and make a measurement of the nuclear level density and effect of shell correction in the doubly magic ^{132}Sn nucleus using radioactive ion beam.

References

[1] V. M. Strutinsky, Sov. J. Nucl. Phys. Vol. **3**, 449 (1966).

[2] W. D. Myers and W. J. Swiatecki , Nucl. Phys. **81**, 1 (1966).

[3] V. M. Strutinsky, Nucl. Phys. A **95**, 420 (1967).

[4] A. Bohr and B. R. Mottelson, Nuclear Structure (Benjamin, New York,1998), Vol.**2**.

[5] S. G. Nilsson and I. Ragnarsson, Shapes and Shells in Nuclear Structure (Cambridge University Press, 1995).

[6] V. M. Strutinsky, Nucl. Phys. **A 122**, 1 (1968).

[7] W.D. Myers and W.J. Swiatecki, Lawrence Berkeley Laboratory Report **LBL-36803** (1994).

[8] Mayer M. G., Phys. Rev., **74** (1948) 235.

[9] S. Raman, C. W. Nestor, JR., and P. Tikkanen, Atomic Data and Nuclear Data Tables, **78**, 1 (2001).

[10] R. G. Stokstad, in Treatise on Heavy Ion Science, edited by D. A. Bromley (Plenum,New York, 1985),**Vol. 3**, p. 83.

[11] J. R. Huizenga and L. G. Morretto, Ann. Rev. nucl. Sci. **22** 427 (1972).

[12] H. A. Bethe, Phys. Rev. **50**, 332 (1936).

[13] A. Bohr and B. R. Mottelson, Nuclear Structure (Benjamin, New York,1969), Vol.**1**.

[14] J. R. Grover, Phys. Rev. **157**, 832 (1967).

[15] F. S. Chang, J. B. French, and T. H, Thio, Ann. Phys. (New York) **66**, 137 (1971).

[16] J. N. Ginocchio, Phys. Rev. Lett. **31**, 1260 (1973).

[17] H. Nakada and Y. Alhassid, Phys. Rev. Lett. **79**, 2939 (1997); Phys. Lett. B 436, 231 (1998).

[18] Y. Alhassid, S. Liu, and H. Nakada, Phys. Rev. Lett. **83**, 4265 (1999).

[19] Y. Alhassid, S. Liu, and H. Nakada, Phys. Rev. Lett. **99**, 162504 (2007).

[20] Y. Alhassid, L. Fang, and H. Nakada, hys. Rev. Lett. **101**, 082501 (2008).

[21] L. G. Moretto, Nucl. Phys. **A 185**, 145 (1972).

[22] T. D. Newton, Can. J. Phys. **34**, 804 (1956).

[23] A. G. W. Cameron, Can. J. Phys. **36**, 1040 (1958).

[24] https://ntof-exp.web.cern.ch/ntof-exp/index.php?page=basicNuc

[25] A. Aspinall, G. Brown, and S. E. Warren, Nucl. Phys. **46**, 33 (1963).

[26] A. A. Katsanos, J. R. Huizenga, and H. K. Vonach, Phys. Rev. **141**, 1053 (1966).

[27] A. Schiller, L. Bergholt, M. Guttormsen, E. Melby, J. Rekstad, and S. Siem, Nucl. Instrum. Methods **A 447**, 498 (2000).

[28] N. U. H. Syed et al., Phys. Rev. C **79**, 024316 (2009).

[29] T. Ericson and T. Mayer-Kuckuk, Annu. Rev. Nucl. Sci. **16**, 183 (1966).

[30] J. R. Huizenga, H. K. Vonach, A. A. Katsanos, A. J. Gorski, and C. J. Stephan, Phys. Rev. **182**, 1149 (1969).

[31] E. Gadiolli and L. Zetta, Phys. Rev. **167**, 1016 (1968).

[32] D. R. Chakrabarty et al., Phys. Rev. C **51**, 2942 (1995).

[33] A. V. Voinov et al., Phys. Rev. C **88**, 054607 (2013).

[34] A.V. Voinov et al., Phys. Rev. C **79**, 031301(R)(2009).

[35] A.V. Voinov et al., Phys. Rev. C **77**, 034613(2008).

[36] A.V. Voinov et al., Phys. Rev. C **76**, 044602 (2007).

[37] V. S. Ramamurthy, S. K. Kataria and S S. Kapoor, Phys. Rev. Lett. **25**, 386 (1970).

[38] A. V. Ignatyuk, G.N. Smirenkin and A.S. Tishin, Sov. J. Phys. **21**, 255 (1975).

[39] G.F. Knoll, Radiation Detection and Measurement, John Wiley & Sons, Inc., 2007.

[40] N. Tsoulfanidis, Measurement and detection of radiation, Tayloy & francis, 1995.

[41] S. Tavernier, Experimental Techniques in Nuclear and Particle Physics, Springer, 2010.

[42] A. Mitra et al., Nucl. Phys. **A 765** (2006) 277; *ibid* **A 707**, 343 (2002).

[43] G. Charpak, L. Dick, L. Feuvrais, Nucl. Instr. and Meth. **15**, 323 (1962).

[44] see SCIONIX website http://www.scionix.nl.

[45] A. Manna, A. Mishra, S.G. Thombare, P.K. Mukhopadhyay, J. Bhattacharya, Proc. National Symp. on Nuclear Instrumentation, IGCAR, Kalpakkam, India (2004) p. 93.

[46] L. Karsch, A. Böhm, K. -Th. Brinkmann, L. Demirörs, M. Pfuff, Nucl. Instr. and Meth. **A 460**, 362 (2001).

[47] C.H. Poppe, J.D. Anderson, J.C. Davis, S.M. Grimes, C. Wong, Phys. Rev. **C 14**, 438 (1976).

[48] W. Nelson, H. Hirayama, D. Roger, Stanford University Report SLAC-265 1985.

[49] R.A. Cecil, B.D. Anderson, R. Madey, Nucl. Instr. and Meth. **161**, 439 (1979).

[50] P. Kuijper, J.C. Veefkind and C.C.Jonker, Nucl. Phys. **A 181**, 545 (1972).

[51] D.A. Gothe, V. Nanal, R.G. Pillay, Proc. DAE-BRNS Symp. on Nucl. Phys. **46 B**, 506 (2003).

[52] J. Alarja, A. Dauchy, A. Giorni, C. Morand. E. Pollaco, P. Stassi, R. Billerey. B. Chambon, B. Cheynis. D. Drain and C. Pastor, Nucl Instr. and Meth. **A 242**, 352 (1986).

[53] R. Fülle, Gy. Máthé and D. Netzband, Nucl. Instr. and Meth **35**, 250 (1965).

[54] J. G. ál, G. Kalinka, B. M. Nyakó, G. E. Perez, Z. Máté, G. Hegyesi, T. Vass, A. Kerek, A. Johnson, Nuclear Instruments and Methods in Physics Research **A 366**, 120 (1995).

[55] See www.SRIM.org, J.F. Ziegler, J. Biersack, U. Littmark, The Stopping and Range of Ions in Matter (Pergamon Press, 1985).

[56] Y. Larochelle, L. Beaulieu, B. Djerroud, D. Doré, P. Gendron, E. Jalbert, R. Laforest, J. Pouliot, R. Roy, M. Samri, C. St-Pierre, Nucl Instr. and Meth. **A 348**, 167 (1994).

[57] K. G. Prasad, Nucl. Instr. and Meth. **B 40/41**, 916 (1989).

[58] B. Srinivasan, S. K. Singh, R. G. Pillay , M. B. Kurup and M. K Pandey, Pramana **57**, 651 (2001).

[59] M. B. Kurup, Pramana **59**, 811 (2002).

[60] M.Y. Vaze, V.M. Datar, P.J. Bhalerao, H.C. Jain, S.N. Mishra, S.D. Narvekar, U.T. Raheja and R.G. Pillay, Indian Journal of Pure and Applied Phys. **35**, 193 (1997).

[61] Suresh Kumar, V.M. Datar, D.R. Chakrabarty, P.C. Rout, R. Kujur, Proc. of the Int. Symp. on Nucl. Phys. Vol. **54**, 702 (2009), URL = http://sympnp.org/proceedings/index.php.

[62] LAMPS - Linux Advanced Multiparameter data acquisition System, URL = http://www.tifr.res.in/∼pell/lamps.html.

[63] K Ramchandran, Thesis on "Fission time scales from pre-scission multiplicities and evaporation residue cross-sections ", University of Mumbai, 2010.

[64] Rene Brun and Fons Rademakers, Nucl. Inst. & Meth. in Phys. Res. **A 389**, 81 (1997), URL = http://root.cern.ch/.

[65] P. C. Rout, D. R. Chakrabarty, V. M. Datar, S. Kumar, E. T. Mirgule, A. Mitra, V. Nanal, and R. Kujur, Nucl. Instr. & Meth. **A 598**, 526 (2009).

[66] V. Weisskopf, Phys. Rev., **52**,295 (1937).

[67] V. Weisskopf and D. H. Ewing, Phys. Rev. **57**, 472 (1940).

[68] W. Hauser and H. Feshbach, Phys. Rev. **87**, 366 (1952).

[69] A. J. Cole, Statistical Models For Nuclear Decay-From Evaporation to Vaporization (IOP Publishing Ltd., 2000)

[70] D. R. Chakrabarty, lecture notes, SERC school at IUAC, New Delhi (2008).

[71] F. Puhlhofer, Nucl. Phys. **A 280**, 268 (1980).

[72] P R S Gomes *et al.*, Phys. Rev. C **71**, 017601 (2005).

[73] A. Shrivastava *et al.*, EPJ Web of Conferences, **17**, 03001 (2011).

[74] P. C. Rout, D. R. Chakrabarty, V. M. Datar, Suresh Kumar, E. T. Mirgule, A. Mitra, A. Shrivastava,V. Nanal, S. P. Behera, G. Mishra, R. Kujur, Symp. on Nucl. Phys. **57**, 512 (2012).

[75] D.R. Chakrabarty, Nucl. Instr. and Meth.**A 560**, 546 (2006).

[76] P. C. Rout, D. R. Chakrabarty, V. M. Datar, Suresh Kumar, E. T. Mirgule, A. Mitra, V. Nanal, R. Kujur, Proc. DAE-BRNS Symp. on Nucl. Phys. **52**, 325 (2007).

[77] A. Mitra, Thesis on "Angular momentum gated charged particle spectra from low energy heavy ion inducled nuclear reaction ", University of Mumbai, 2010.

[78] K. H. Schmidt et al., Z. Phys. **A 308**, 215 (1982).

[79] S. F. Mughabghab and C. Dunford, Phys. Rev. Lett. **81**, 4083 (1998).

[80] M. Korolija, etal., Phys. Rev. Lett. **60**,193 (1988).

[81] N. Cindro etal., Phys. Rev. Lett. **66**,868 (1991).

[82] M. Dasgupta (priv. comm.).

[83] R.B. Wiringa (priv. comm.), A.K. Jain (priv. comm.).